City Research Online

City, University of London Institutional Repository

Turbine End-wall Aerothermal Management with Engineered Surface Structure

Xin Miao

Department of Mechanical Engineering & Aeronautics

City, University of London

This thesis is submitted for the degree of

Doctor of Philosophy

2018

Abstract

Motivated by the enlarged design space and additional flexibility offered by the latest advances in manufacturing techniques, especially Additive Manufacturing (AM), this thesis investigates a novel turbine end-wall aerothermal management method with the engineered surface structures, through closely coupled experimental and numerical studies.

A 90-degree turning duct and a linear turbine cascade test section were employed for the experimental research in a low-speed wind tunnel. Duct and turbine end-wall heat transfer and cooling effectiveness were measured by transient Infrared Thermography. PIV measurement was conducted to obtain the exit flow field.

Computational fluid dynamics (CFD) simulations were performed using ANSYS FLUENT to compliment the experimental findings. The flow solver uses the finite volume method to solve the three-dimensional Reynolds-Averaged Navier-Stokes (RANS) equations. The k-ω shear stress transport (SST) turbulence model was validated and chosen for all the numerical studies.

The secondary flow control principle of the engineered surface structure in the simplified duct is revealed through a detailed investigation of the flow produced by multiple small surface structures. The CFD and PIV measurement results consistently show that addition of the engineered surface structure on end-wall can effectively reduce the magnitude of streamwise vorticity associated with the secondary flow and alleviate its lift-off motion. For turbine cascade applications, it can be observed that the strength of the passage vortex is effectively reduced, and the passage vortex loss core moves closer to the end-wall with the addition of the engineered surface structure.

The purge air cooling enhancement by the engineered surface structure is then studied. The purge air cooling flow becomes more attached to the end-wall and covers a larger wall surface area with the added end-wall rib structures. Both experimental and numerical results reveal a consistent trend on improving film cooling effectiveness and net heat flux reduction (NHFR). This novel concept was successfully demonstrated in a more realistic turbine cascade case. Enhanced cooling effectiveness and net heat flux reduction were obtained from both experimental data and CFD analysis. The additional surface features were proved to be effective in reducing the passage vortex and providing more coolant coverage without introducing additional aerodynamic loss. The overall Net Heat Load Reduction for the 90-degree turning duct and the turbine cascade is increased by 11% and 2% respectively.

Acknowledgment

Foremost, I would like to express my sincere gratitude to my advisor, Professor Qiang Zhang, for his continuous support during my study and research at the City University of London. He is such an enthusiastic and innovative professor with wide knowledge about different research fields. He leads me to the world of the turbine and invokes my interest in this field. From him, I learned every step about how to conduct effective research and write a good scientific paper. He also taught me how to be a real researcher and to be responsible for my works.

I would also like to thank my second advisor, Professor Chris Atkin. He helped me a lot in my research with his enormous knowledge about aerodynamics. Besides my advisors, I would like to thank Dr. Zhengzhong Sun. He gave me a lot of help in the PIV experiment and spent much time and effort in improving the quality of my papers. I also appreciate Professor Abdulnaser Sayma and Dr. Hao Xia; they gave me a lot of useful suggestions in my thesis.

My sincere thanks also go to Dr. Chetan Jagadeesh, Richard Leach, and Keith Pamment for their technical support in the lab and lots of useful practical advice.

I am grateful to Nathalie Chatelain and all the staff in the Department of Mechanical Engineering and Aeronautics for their help throughout my doctoral study.

I thank all the members of Shanghai Jiao Tong University Aero-Thermal Lab, Hongmei Jiang, Haiteng Ma, Zhaoguang Wang and Qianhui Li; they gave me a lot of help in my transient thermal measurement experiment. The time work with them is the best memory in my life.

Last but not the least, I would like to thank my family and my friends. Without their love and support, I will not be able to overcome all the difficulties.

Contents

Nomenclature

Symbols

A	End-wall surface area
C_p	Pressure loss coefficient
C_x	Axial chord (m)
c	Specific heat (J/kg-K)
c_p	Specific heat at constant pressure (J/kg-K)
d	Rib distance
D	Duct width
f	Sampling frequency (Hz)
h	Heat transfer coefficient (W/(m^2-K)), rib height, enthalpy
H	Duct height
I	Image intensity
Ma	Mach number
$\dot{m}$	Mass flow rate (kg/s)
n	Rib number
p	Pressure (Pa)
P	Pitch, pressure
q''	Heat flux (W/m^2)
r	Duct radius, streamline radius of curvature
Re	Reynolds number
R/D	Radial-wise measurement location normalized by duct width
R^2	Coefficient of determination
S	Span (m)
s	Entropy
$\dot{S}$	Entropy generation rate per unit volume
T	Temperature (K)
t	Time (s)
U	Uncertainty
V	Velocity (m/s)

v	Fluid particle velocity
w	Rib width, work
Y/P	Pitch-wise measurement location norsmalized by pitch
y+	Non-dimensional wall distance: $y^+ \equiv u_t y / \nu$
Z/S	Span-wise measurement location normalized by span

Subscripts

0	Total, without film cooling
ad	Adiabatic
b	Blade metal
c	Coolant air
f	Film cooling
gen	Generation
i	Inner
in	Inlet
mid	Midspan
o	Outer
out	Outlet
p	Purge air
r	Recovery
rev	Reversible
s	Streamwise direction
w	Wall
x	X axis
y	Y axis
z	Z axis
∞	Mainstream

Greeks

β	Pitch angle
γ	Ratio of specific heats
δ	Boundary layer thickness
ζ	Loss coefficient
η	Cooling effectiveness
θ	Non-dimensional total temperature

λ	Thermal conductivity (W/(m-K))
λ_2	The second eigenvalue of the second invariant of the velocity gradient tensor
ρ	Density (kg/m^3)
τ	Time constant (s)
φ	Non-dimensional metal temperature
Ω	Vorticity (s^{-1})

Abbreviations

DAQ	Data acquisition
EXP	Experiment
HTC	Heat transfer coefficient (W/(m^2-K))
IR	Infrared
LDV	Laser Doppler Velocimetry
LPD	Laser powder deposition
NGV	Nozzle Guide Vane
NHFR	Net heat flux reduction
NHLR	Net Heat Load Reduction
PS	Pressure side
RANS	Reynolds-Averaged Navier-Stokes
RMSE	Root-mean-square error
SS	Suction side
SSE	Sum of square error

List of Figures

List of Tables

Chapter 1

Introduction

This thesis investigates the turbine end-wall aero-thermal management with the engineered surface structure. The background relevant to this research is first briefly introduced in Section 1.1, including the gas turbine advantages, application, working principle and cooling challenge. Section 1.2 gives the motivation of this thesis, as well as research objectives. The thesis outline is summarized in the final section.

1.1   Background

The gas turbine is doubtlessly one of the most important inventions of the twentieth century. Compared to other combustion engines, the advantages of the gas turbine in the industrial application are numerous, such as high power/weight ratio, high reliability, low maintenance cost and short start-up time to achieve peak output.

The gas turbines are most well-known to the public for its application to aircraft

propulsion. The gas turbine for aero-engines come in three different configurations (Jansohn (2013)): turbojet/ turbofan, turboprop, and turboshaft. The turbojet is the earliest jet engine; it generates thrust from the kinetic energy of the hot exhaust gas. For civil commercial aircraft, turbojet has been replaced by turbofan, which has a big, single, ducted fan in front of the engine. Most of the air bypasses the turbine, only a small portion of the air passes through the core engine. One example of the powerful aero-engine product shown in Fig.1.1 is the GE90 which now powers the longer-range Boeing 777-200LR, 777-300ER and 777 Freighter aircraft. GE90 has long held the world record with 127 900 pounds of thrust (GE Aviation (2001)) achieved on a test stand. The turboprop propulsion system consists of two main parts: the core engine and the propeller. The core is very similar to a basic turbojet instead of expanding the hot exhaust through the nozzle to create thrust, almost all the engine's power is used to drive the propeller. Because propellers become less efficient as the speed of the aircraft increases, turboprops are used only for low-speed aircraft. The turboshaft engine is composed of two main assemblies: the power section and the gas generator. The gas generator is very similar to the turbojet, while the power section consists of an additional turbine which conveys mechanical power convert it into output shaft power.
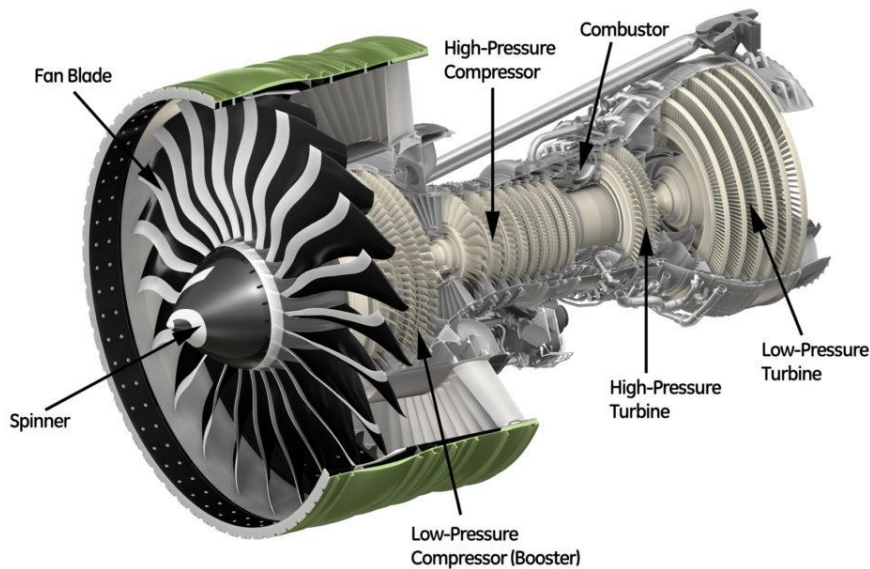
Figure 1.1: GE90-115B Engine. (GE Aviation (2001))

The gas turbine is also widely used for land-based power-generation applications. The designs of these industrial turbines are closely linked to respective aero-engine products, thus called 'aero-derivative' such as the LM series of engines from GE (GE Energy, 2011). Another application of gas turbine is mechanical drives. The majority of gas turbine-powered mechanical load drive machines are used in the oil and gas industry for such duties as pumping, injection and compression, as well as the transportation of oil or gas through a pipeline (Solar Turbines, 2011; MAN Turbo and Diesel, 2011; Siemens, 2011).
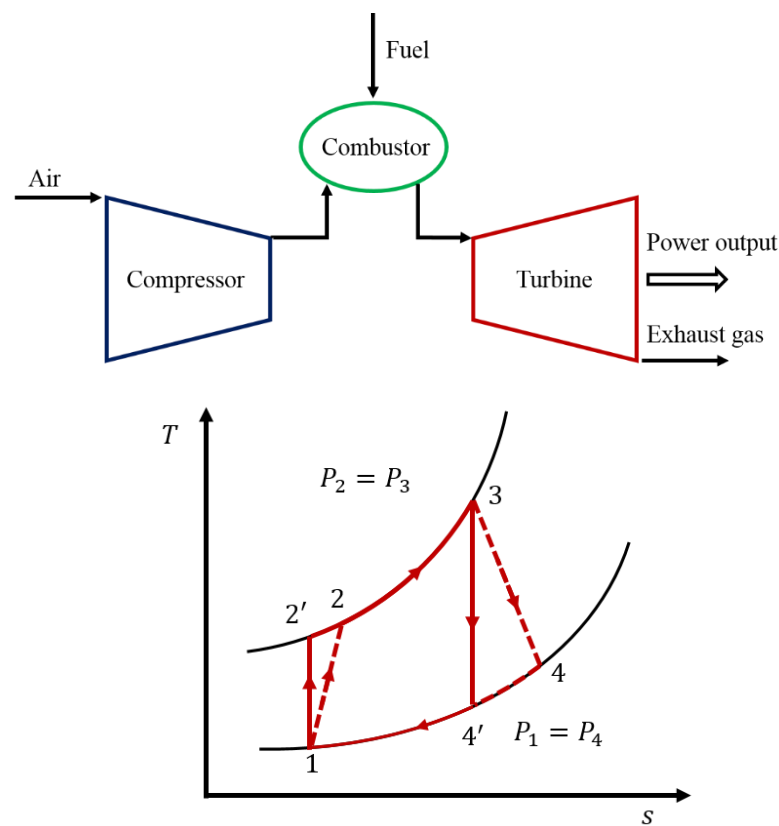
Figure 1.2: Simple gas turbine system and Brayton cycle.

The gas turbine is made up of three main components: the compressor, combustion chamber, and turbine. The basic principle of the gas turbine is well known, the operation diagram and ideal Brayton cycle for a simple gas turbine are shown in Fig.1.2 to explain the working mechanism. Air is drawn into the compressor and the pressure is increased isentropically between states 1 and $2'$. Fuel is injected into the combustor where it mixes with the compressed air and is burned. This process is assumed to be reversible and isobar. The high-pressure high-temperature gas from

the ignited mixture moves through the turbine blades forcing them to spin between states 3 and 4′. Therefore, chemical energy is converted into mechanical energy. A small part of the energy is used to drive the compressor, while the remaining provides thrust for propulsion of the aircraft. As irreversibilty in the real case, the compressor consumes more work, and the turbine produces less work than that of the ideal Brayton cycle which is depicted by dashed lines in the T-s diagram. In addition, due to the frictional and aerodynamic losses in a combustor, total pressure losses also occur during the combustion process.
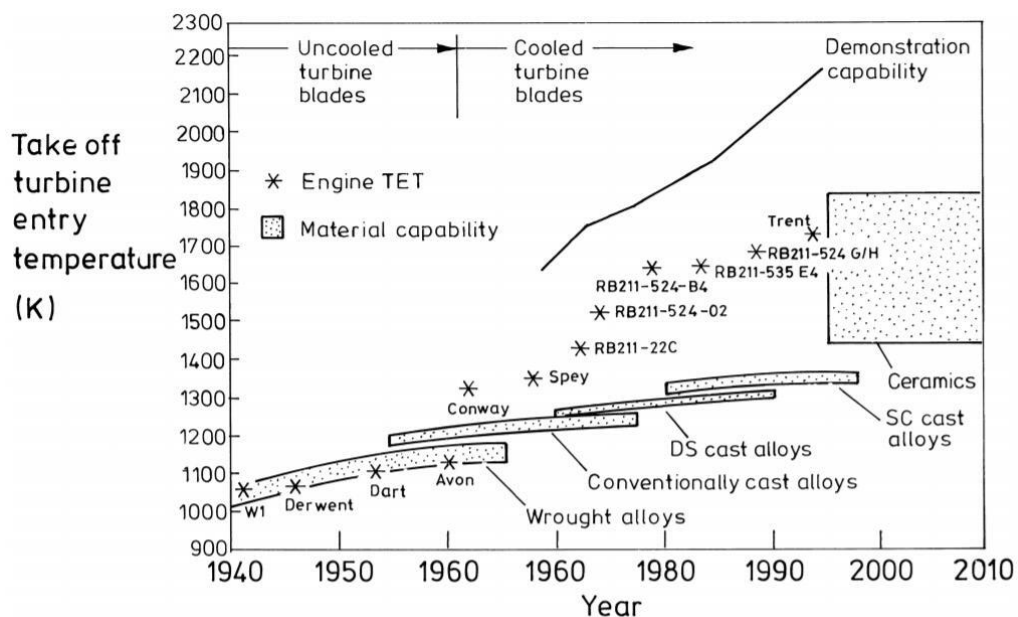
Figure 1.3: Evolution of turbine entry temperature. (Cumpsty and Heyes (2015))

The efficiency of the ideal Brayton cycle is largely influenced by three key factors: the overall pressure ratio of the compressor (OPR); the single component efficiencies and the turbine entry temperature (TET) (Cumpsty and Heyes (2015)). Although increased OPR can improve the efficiency of a gas turbine, the compressor temperature also increases which has an adverse effect on gas turbine cooling.

Incremental gains in individual component efficiencies can add up to significant savings over the whole engine. In turbomachinery, efficiency is probably the most important performance, a small change in the efficiency of either component causes a much larger proportional change in the power output. Denton (1993) discussed the

origins and effects of loss in turbomachinery and divided the losses into three components: the profile losses, tip-leakage losses and secondary losses. Profile losses are generated in the blade boundary layers away from the end-wall. The profile losses are typically measured at midspan where the flow is often assumed as two-dimensional. Additional losses from the trailing edge sudden expansion and downstream mixing are generally included in the profile losses. Tip-leakage losses are generated primarily from the leakage of the flow over the gap between the stationary casing wall and moving rotor blade. Secondary losses are generated within the end-wall surface boundary layers and through the downstream mixing of the end-wall vortical structures. The vortical structures, also named as secondary flow, is defined as deviations from primary inviscid flow through the passage, three-dimensional boundary layers, large streamwise vortices, and separated flows present at the end-wall are collectively referred to secondary flows. It is well-known that secondary flows have a significant impact on the aerodynamic efficiency and durability of turbine components. According to Sharma and Butler (1986)'s research, the secondary loss can account for 30%-50% of the total aerodynamic loss. Therefore, one research filed identified by designers as a source of efficiency improvement is to reduce the losses generated from the complex flow present at the end-walls.

Turbine Entry Temperature (TET) also largely influences the efficiency. The improvement in turbine entry temperature and material capabilities of Rolls Royce gas turbines is shown in Fig. 1.3. It can be seen that the TET increased rapidly since 1961 when cooled blades were first introduced to the Conway engine (Saravanamuttoo et al. (2001)). Nowadays, the TET can be achieved at 1800K, which is far beyond the blade melting point. In order to avoid this extreme thermos-mechanical loads reducing component lifetimes and decreasing reliability, a lot of gas turbine cooling techniques have been applied. Secondary flow also has a significant detrimental effect on end-wall cooling efficiency. A 25°C temperature increase for a component operating in a 1500°C environment can reduce half of the component life (Han et al. (2012)).

1.2   Research Motivation and Objectives

The main motivation of this thesis is the increased design space and flexibility to turbine aerothermal management offered by the latest advances in manufacturing techniques, especially Additive Manufacturing (AM).

Additive Manufacturing is a process based on the principle of creating or fabricating components or assemblies in a layer-by-layer addition of material. This is in direct contrast to the traditional subtractive manufacturing where the material is removed from a block of raw material until the desired final shape is formed. AM has three major advantages compared with the traditional manufacturing methods like machining and welding: substantially reduce product development time; leave behind little material waste and improve the flexibility for manufacturing complex products with unique geometries (Yan and Gu (1996)). Several AM technologies have emerged over the past decades, such as Stereolithography (SLA), Selective Laser Sintering (SLS), Fused Deposition Modelling (FDM), Laminated Object Manufacturing (LOM), etc. All these technologies work on the same basis of layered manufacturing, the differences among them relate to the materials used, the equipment employed, the fabrication environment, and fabrication process or technique (Bikas et al. (2015)). Siemens first finished full-load engine tests for gas turbine blades completely produced by using AM technology. Multiple 3D- printed turbine blades were successfully validated with a conventional blade design at full engine conditions. With AM technique, the lead time for prototype development reduces up to 90 percent (Navrotsky et al. (2015)). Although the machines and materials used for metal AM remain expensive, in the reasonably foreseeable future, AM could be the main procedure to undertake many product enhancements in parts or designs.

Besides using AM technique, the engineered surface features could also be produced by traditional manufacturing techniques such as profile grinding (Denkena et al. (2010)). The manufacturing process by ball-end mill cutter is shown in Fig. 1.4a. Upon the completion of machining, a groove surface structure is left after the process. Detailed groove structure can be observed in an impeller in Fig. 1.4b. The manufac-

turing cost would increase greatly for fabricating the impellers with a smoother surface. This is based on the conventional wisdom that a smooth surface is always more aerodynamically efficient. It certainly becomes more feasible and less costly to fabricate small-scale engineered surface features compared to removing this residual roughness.

(a)   (b)
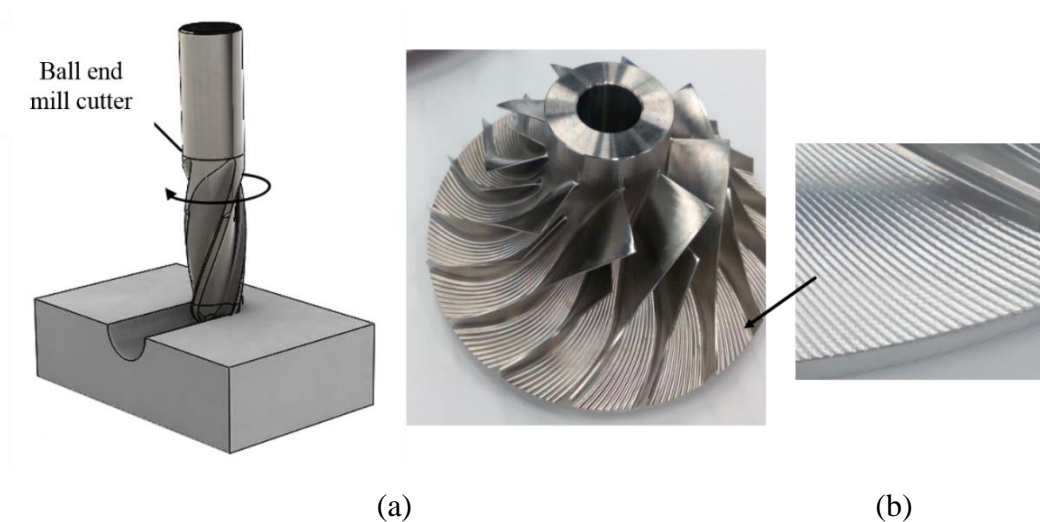
Figure 1.4: (a) manufacture process and (b) an impeller manufactured with different wavy grooves.

This study investigated one novel concept for turbine end-wall aerothermal management which can be implemented by the recent advances in manufacturing techniques. The engineered surface structure can be optimally designed and added to the turbine end-wall. There are two major potential benefits: (1) end-wall secondary flow control (2) purge air cooling enhancement. Exploring these potentials is the major aim of this research.

The research objectives are:

1. Exploit the fundamental flow physics and working principle of the engineered surface structure in a simplified curved channel and understand the influence of different surface features on the end-wall secondary flow control.

2. Investigate the potential of engineered surface structure in controlling the undesired end-wall secondary flow in a real turbine system.

3. Investigate purge air cooling enhancement through the engineered surface structure added to the turbine end-wall.

4. Validate numerical models by flow field information and end-wall heat transfer data obtained through PIV and transient thermal measurement technique.

1.3 Thesis Structure

Chapter 2 reviews literature relevant to the study of end-wall aerothermal management. The physics of the secondary flow, secondary loss reduction methods, an overview of purge air and end-wall cooling are introduced.

Chapter 3 provides details of the experiment apparatus and procedures. The low-speed wind tunnel, the 90-degree turning duct and the linear cascade test section are described first, followed by the PIV and heat transfer experiment setup. Two experimental techniques: PIV and transient thermal measurement, which are used in aero-optical and cooling experiment respectively are reported. Data acquisition system and flow condition are also described. The measurement uncertainties are discussed at the end of this chapter.

Chapter 4 describes the numerical setup and procedures for the computational portion of this thesis. Computational domain, grid independence, solver, as well as code validation are discussed.

The numerical and experimental results are presented in Chapter 5 and 6. Chapter 5 investigates the effect of the engineered surface structure in controlling the end-wall secondary flow. A 90-degree turning duct is employed as a simplified model for the turbine passage without introducing the horseshoe vortex. Then the concept is applied to a linear turbine cascade to study its effect on secondary flow control. The working principle of the engineered surface structure is revealed through detailed analysis.

The feasibility of enhancing purge air cooling effectiveness through a series of small-scale ribs added onto the end-wall is explored in Chapter 6. The fundamental working mechanism and cooling performance in a 90-degree turning duct are first

presented. Then the engineered surface structures concept is validated in a more realistic turbine cascade case. Purge air flow structure and end-wall heat transfer in both low and high-speed condition are further discussed.

Lastly, the results and contributions of the study are summarized in Chapter 7. The main conclusions of this thesis and suggestions for future work are given.

10

Chapter 2

Literature Review

Literature relevant to the study of end-wall aerothermal management is reviewed in this chapter. Section 2.1 describes the definition and generation of secondary flow. Different secondary flow models and secondary loss are discussed in the followed two sections. Section 2.4 reviews three control methods for secondary loss reduction. The working mechanism of each method is introduced in detail. Section 2.5 reviews the heat transfer performance of end-wall and highlights the significant influence on heat load. Some widely used end-wall cooling techniques are then reported. The purge air system, the effect of rim seal geometry, as well as the interaction between purge air and mainstream are also described.

2.1 Fundamental Secondary Flow Theory

Secondary flow occurs whenever viscous fluid turns in a curved passage. The basic flow configuration in a duct is shown in Fig 2.1. When the flow turns through a curved passage, the flow far away from the end-wall can be considered as a two-dimensional flow. This mainstream sets up a pressure gradient normal to the streamlines which balance the normal acceleration of the fluid particles moving round the bend with velocity and streamline radius of curvature. Consider a small element of fluid of mass dm, of unit depth and subtending an angle $d\theta$ at the axis, as shown in Fig 2.1a. The element is in radial equilibrium so that the pressure forces balance the centrifugal forces (Dixon and Hall (2005)).

$$(p + dp)(r + dr)d\theta - prd\theta - \left(p + \frac{1}{2}dp\right)drd\theta = dmv^2/r \qquad (2.1)$$

Where v is fluid particle velocity and r is streamline radius of curvature. Identifying $dm = \rho r d\theta dr$ as the mass per unit depth, and ignoring the second order terms, the radial momentum equation is obtained.

$$\frac{\partial p}{\partial r} = \frac{\rho v^2}{r} \qquad (2.2)$$

Near the end-wall, the fluid in the boundary layer also experiences the same pressure gradient $(\partial p/\partial r)$ but has a lower velocity. According to Equation 2.2, since the velocity in the boundary layer is lower than mainstream velocity, the boundary layer streamlines must have a smaller radius of curvature than mainstream. Therefore, the boundary layer fluid is swept towards the inner wall of the bend. The two-dimensional flow is termed the primary flow and the three-dimensional effect near the end-wall is called secondary flow.

Secondary flow can also be described in terms of vorticity components (Greitzer et al. (2007)). At the inlet, the mainstream velocity can be considered uniform in a direction crossing the channel, the velocity only varies in the spanwise direction. The vorticity magnitude is given by the velocity gradient, and the direction of vorticity follows from the right-hand screw rule, as indicated by the arrow AB in Fig 2.1b. The vorticity direction is normal to the inlet velocity and in a plane parallel to the end-wall.

As the flow proceeds round the bend, the fluid near the inner wall has higher velocity than that in the inner wall. Fluid particles on the outside wall has farther to travel (Greitzer et al. (2007)). Because vortex line behaves the same way as the material line, the vortex line is stretched at the outlet, ends up as $A'B'$. Thus, the vorticity has a streamwise component which leads to a secondary circulation as indicated in the channel cross-section.

The simplest equation for the streamwise component of vorticity was derived by Squire (1951). If the deflection angle is not large, the magnitude of the secondary vorticity equals to twice the inlet normal vorticity times the flow turning angle.

$$\Omega_{2s} = -2\Omega_1(\alpha_2 - \alpha_1) \tag{2.3}$$

where Ω_{2s} is the outlet streamwise vorticity, Ω_1 is the inlet normal vorticity, α_1 and α_2 are the inlet and exit yaw angle respectively.

The generation of secondary flow has also been discussed in some detail by Horlock (1958), Preston (1954), Carter (1948) and many other researchers.
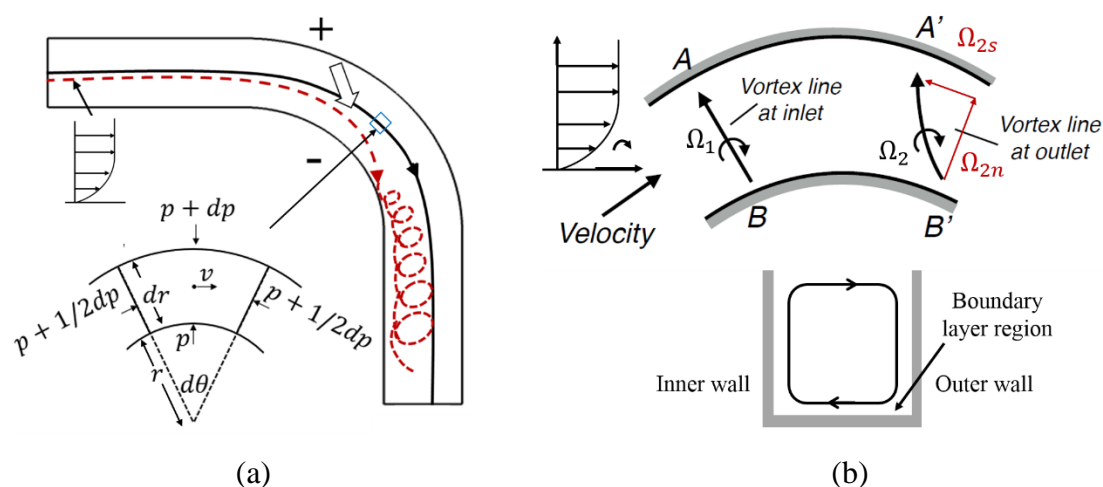
Figure 2.1: Generation of secondary flow in a curved duct (Modified by Greitzer et al. (2007)).

Such secondary flow behavior exists in wide industrial applications, including open channel flows (Thomson (1877); Blanckaert and De Vriend (2004)), ducts of ventilating systems (Humphrey et al. (1981)), piping of pumps and blowers (Sprenger (1969); Berger et al. (1983)), aircraft intakes (Sullerey and Pradeep (2004);

Paul et al. (2011)), turbomachinery passages (Horlock (1973); Horlock, and Lakshminarayana (1973); Langston (1980); Langston (2001)), etc. Among all these applications, the secondary flow in turbomachinery is the most complicated. Next section will focus on this three-dimensional secondary flow in turbomachinery.

2.2   Secondary Flow Models in Turbine System

Secondary flow has been studied over decades because its importance to increase the efficiency of turbomachines. A number of secondary flow models have been proposed to show the structure and the development of secondary flow. There are two general reviews which introduce very detailed model theories and background on secondary flow research. One was done by Sieverding (1985), he gives a brief review of pre-1985 work. The other one written by Langston (2001) focuses on work done from 1985 to 2000. These secondary flow models are very helpful to improve the understanding of the origin and development of various vortices and the loss induced by secondary flow. Among all these models, there are some prominent features of the secondary flow namely: passage vortex; corner vortex; horseshoe vortex and counter vortex.

Horseshoe vortex is formed when a boundary layer fluid meets any blunt object. In turbomachinery, the horseshoe vortex is formed around the leading edge of the blade. Eckerle and Langston (1986) studied the horseshoe vortex formation by using a large cylinder in the low-speed wind tunnel, as shown in Fig.2.2. The flow outside the boundary layer has higher stagnation pressure than the flow near the end-wall, the pressure gradient leads to a downward flow at the end-wall and cylinder junction. The incoming flow in the boundary layer interacts with the reverse flow and curls up into the horseshoe vortex. In a turbine system, the two legs of the horseshoe vortex are not symmetric. The pressure side leg crosses the blade passage to the suction side and interacts with the passage vortex. The rotation direction of the passage vortex and pressure side leg of the horseshoe vortex is the same. Therefore, the two structures are merged and become the dominant secondary flow feature, while another leg (suction side leg) moves into the adjacent passage and becomes the counter vortex. It rotates in the opposite sense to the passage.
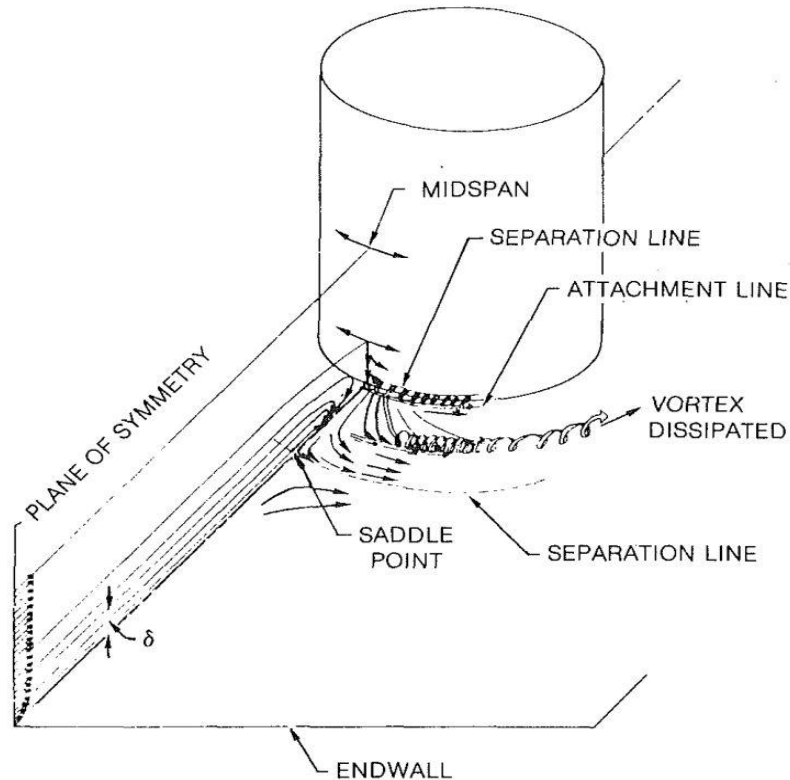
Figure 2.2: Horseshoe vortex formation (Eckerle and Langston (1986)).

Passage vortex is the dominant flow feature of the secondary flow, it caused by the pitchwise pressure gradient inside the blade passage. The velocity in the boundary layer is low. According to Equation 2.2, in order to balance the pitchwise pressure gradient the streamline curvature radius in the boundary layer should be reduced. Therefore, the boundary layer flow turned more than the main flow in the passage, so a cross-flow from the pressure side to the suction side occurs. In order to preserve the continuity, a vertical flow is formed, and the passage vortex develops from this recirculating flow. The strength of the passage vortex mostly depends on the flow turning angle, blade loading, and pitchwise pressure gradient.

Corner vortex, as the name suggests, is induced at the corner of blade edge at the end-wall and much smaller than passage vortex. It is generated by the interference of the cross flow and the near suction side flow in the baled passage. Corner

vortex is very difficult to verify experimentally and can only be observed in experiments with high turning. The size of the corner vortex depends on the blade loading, the higher loading is, the stronger corner vortex becomes.
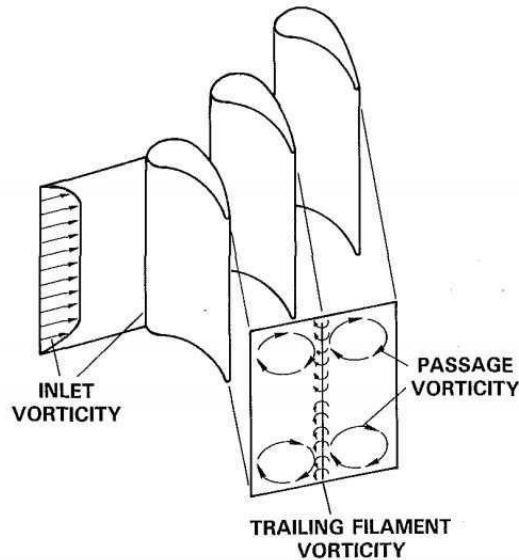
Figure 2.3: Secondary flow model of Hawthorne (1955).

The classic secondary flow model was proposed for the first time by Hawthorne (1955). The vortex system is presented in Fig. 2.3. The passage vortex presents the distribution of secondary circulation, which occurs due to the stretch of the vortex line as discussed in Section 2.1. The trailing filament vorticity arises because the fluid passes through the cascade with different velocities between suction and pressure side. However, the formation of horseshoe vortex at the leading edge was not discussed.

One of the earliest studies was done by Langston et al. (1977). A low-speed cascade wind tunnel was used in their work, detailed measurements were made by a 5-hole probe and hot wire from upstream to downstream. Fig.2.4 shows the classic secondary flow model from the results. The inlet boundary layer separates at the blade leading edge and generates the horseshoe vortex, then one leg of the horseshoe vortex (pressure side leg) moves into the passage and becomes the passage vortex by the cross pressure gradient, while the other leg, termed the suction side leg, enters into the adjacent passage and becomes the counter vortex which has an opposite

sense of rotation to the passage vortex.
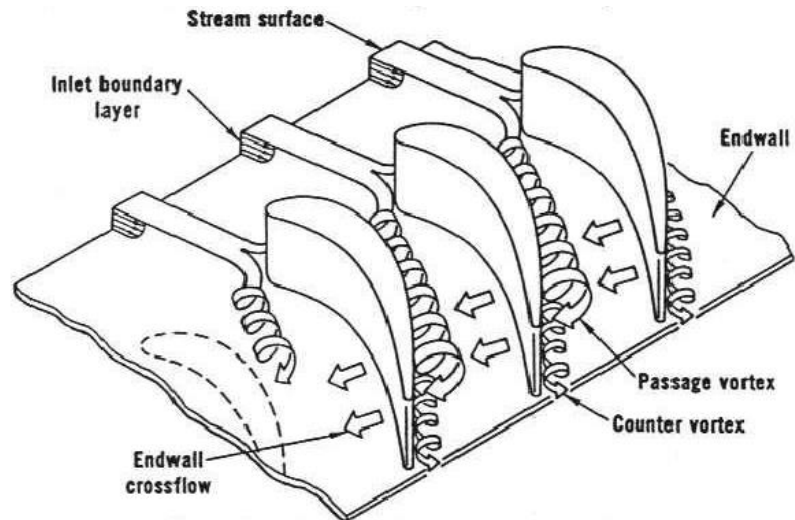
Figure 2.4: Secondary flow model of Lanston et al. (1980)
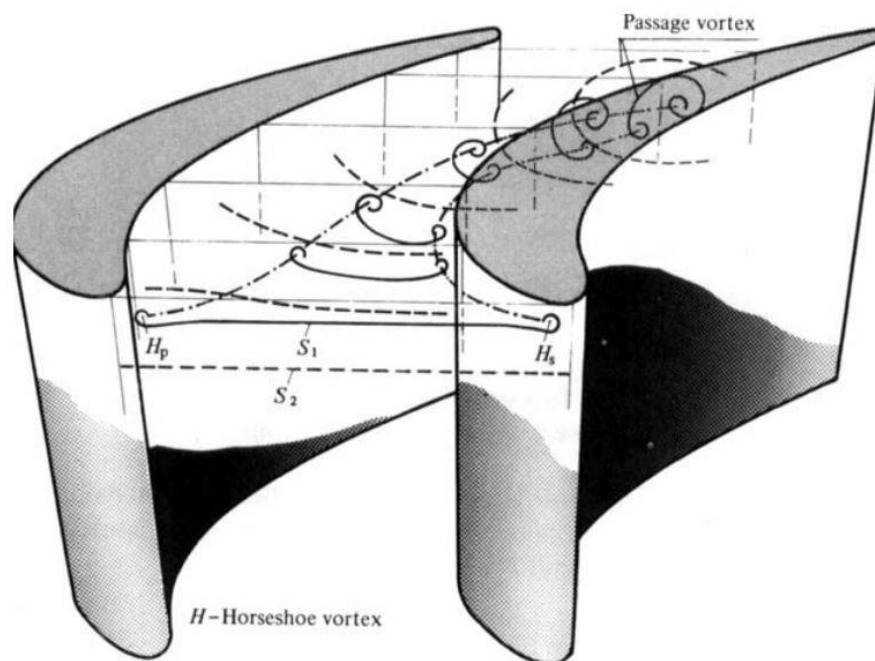
Figure 2.5: Secondary flow model of Sieverding and Van Den Bosche. (1983)

The model of Sieverding and Van Den Bosche (1983) shows the development and interaction of the passage vortex and counter vortex by using the colored smoke wire technique. In Fig. 2.5, stream surface S1 is situated in the end-wall boundary

layer, stream surface S2 is situated outside the end-wall boundary layer. Both stream surfaces are parallel to the end-wall. The model shows that the horseshoe vortex and passage vortex do not exist independently, both of them are part of the same vortex structure.

Sharma and Butler (1986) described a secondary flow pattern from improved understanding of others and their own experimental data. The development of leading edge horseshoe vortex, passage vortex and corner vortex are shown in Fig.2.6. Different from the other versions of secondary flow model, the suction side leg of horseshoe vortex wraps around the passage vortex instead of adhering to the suction side. They used this approach to develop a semi-empirical model for estimating the end-wall losses. One of their key findings is that the inlet boundary layer losses are convected through the passage without causing additional losses.
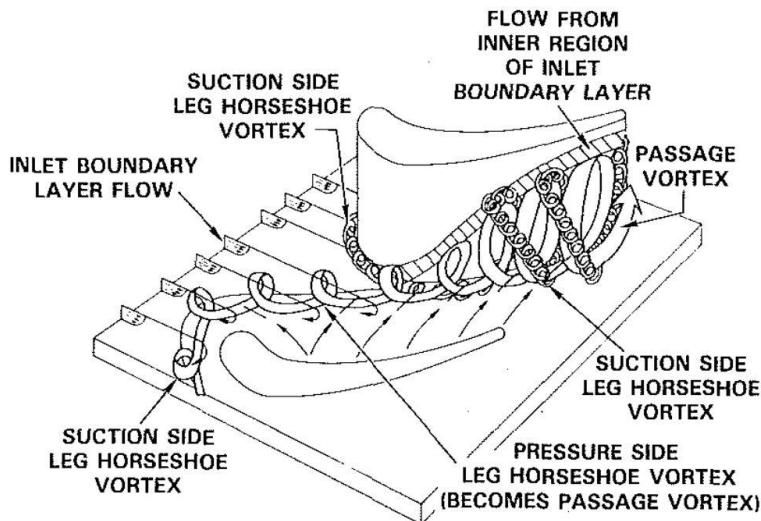
Figure 2.6: Secondary flow model of Sharma and Butler. (1986)

Detailed flow visualization study was performed by Wang et al. (1995). Multiple smoke wires were used to investigate the secondary flow near the end-wall region. The wires were positioned parallel to the end-wall ahead of the cascade. The smoke trace generated by the wires was illuminated by a laser light sheet, the development and evolution of the horseshoe vortex and passage vortex were clearly resolved. In their model shown in Fig. 2.7, more detailed flow structures were observed near the leading edge of the cascade. Because the experimental was run in a

low Reynolds number, for the same inlet boundary layer, the strength of the secondary flow is stronger under this laminar flow condition. Thus, the vortex structure is more stable.

There are three main reasons why there are so many different secondary flow models. Firstly, the secondary flow is much depending on turning angle, different blade profiles lead to different results. Secondly, various studies used different instruments and techniques. Thirdly, different experiments were conducted in different Reynolds numbers, thus the strength of secondary flow is not the same, and some small vortex structures are unstable. Despite the progress achieved in recent years, further work on secondary flow model is still needed.

V_{sh} : Suction side leg of horseshoe vortex system
V_{ph} : Pressure side leg of horseshoe vortex system
V_{p} : Passage vortex
V_{wip} : Wall vortex induced by the passage vortex
V_{sLc} : Suction side leading edge corner vortex
V_{pLc} : Pressure side leading edge corner vortex
V_{sc} : Suction side corner vortex
V_{pc} : Pressure side corner vortex
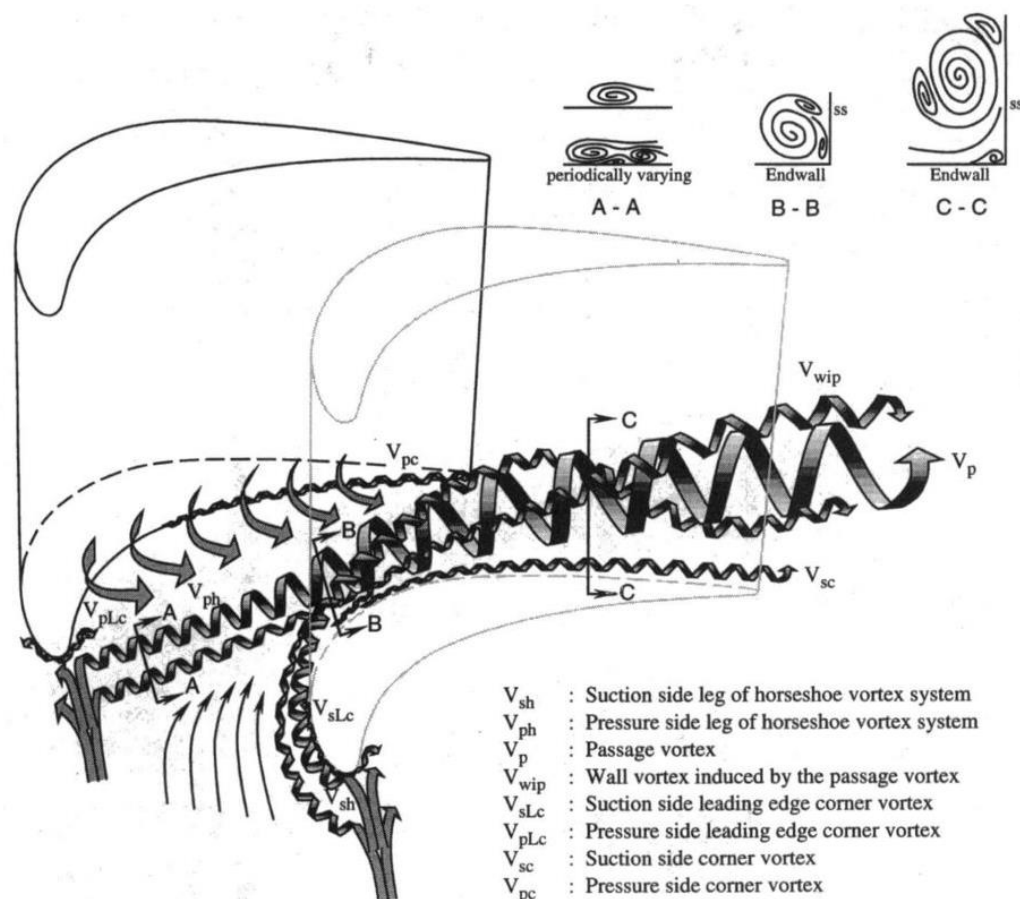
Figure 2.7: Secondary flow model of Wang et al. (1995)

2.3   Secondary Loss

Secondary flows have a number of undesirable effects, as described by Gregory-

Smith (1997):

1) It produces extra mixing losses.

2) It can change the work output by altering the flow angle in the tangential direction.

3) It can provide a non-uniform flow at downstream of the blade row which reduces the efficiency.

4) It can introduce non-uniform heat transfer across the blade and end-wall surface.

Among all these undesirable effects, secondary loss received much attention due to its large effect on the efficiency of turbomachinery, thus this section will mainly focus on the undesirable secondary loss. The secondary loss has been investigated for many years despite the fact that the physical origin of much of the loss is still unknown. People use the term secondary because originally it was thought that the loss is caused by secondary flow. Fundamentally, loss occurs when velocity gradients between two elements of fluid are high which leads to viscous dissipation of energy. In the early years of gas turbine development, several correlations of experimental data were produced to attempt to predict the loss. Gregory-Smith and Graves (1983) produced a method to estimate secondary losses. Three parts were used to model the physical nature of the flow: a triangular loss core produced from the inlet boundary layer, a new boundary layer loss calculated from a two-dimensional calculation, and the third component of loss roughly equal to secondary kinetic energy at the exit. Sharma and Butler (1986) presented another method to predict the secondary losses. The "penetration height" of the secondary flow region is used and the authors quote an accuracy of ±10% for this method. Denton (1987, 1993) described the process of loss production in turbine machines and pointed out that most descriptions of loss in the paper are vague, the loss should be defined in terms of entropy increase. Denton listed the losses found in turbine machines including the secondary loss. In his paper, secondary loss combines many factors, about 2/3 of it comes from the entropy generation in the wall boundary layers, another part comes from mixing loss of inlet boundary layer, the third component is the loss associated with the secondary kinetic energy.

2.3.1 Entropy Generation from Secondary Flow

The relationship between entropy generation and lost work is described by Greitzer et al. (2007). The first and second law of thermodynamics are given for a differential process by Equation 2.4 and Equation 2.5.

$$dw = dq - dh \tag{2.4}$$

$$ds = \frac{dq}{T} + ds_{gen} \tag{2.5}$$

Where w is the work done per unit mass, q is the heat transfer and h is the enthalpy. Combining Equation 2.4 and 2.5 to eliminate the heat transfer term yields an expression for the work extracted for a reversible ($ds_{gen} = 0$) and non-reversible process, given by

$$dw_{rev} = -dh + Tds \tag{2.6}$$

$$dw = -dh + Tds - Tds_{gen} \tag{2.7}$$

The difference between these two processes is the lost work, which is given by Equation 2.8. Therefore, entropy generation due to irreversible process is a measure of total lost work.

$$dw_{loss} = dw_{rev} - dw = Tds_{gen} \tag{2.8}$$

Many researchers use the entropy generation rate to investigate the origin of secondary loss. Denton and Pullan (2012) studied the source of secondary loss from the CFD simulation results and analyzed the entropy generation rate development through the cascade in detail. Zlatinov et al. (2012) developed a consistent framework for interpreting entropy generation as a measure of loss for turbomachinery applications with secondary air streams. Grewe et al. (2014) investigated the effect of end-wall geometry variations on turbine efficiency. Entropy generation rate was used to determine the loss mechanism associated with each geometry features. The entropy generation rate per unit volume will be derived in the following subsection.

The expression for the rate of change of entropy per unit mass can be obtained by splitting the energy equation (Greitzer et al. (2007))

$$T\frac{Ds}{Dt} = \frac{1}{\rho}\tau_{ij}\frac{\partial u_i}{\partial x_j} - \frac{1}{\rho}\frac{\partial q_i}{\partial x_i} \tag{2.9}$$

$$\rho\frac{Ds}{Dt} = \frac{1}{T}\tau_{ij}\frac{\partial u_i}{\partial x_j} - \frac{1}{T}\frac{\partial q_i}{\partial x_i} = \frac{1}{T}\tau_{ij}\frac{\partial u_i}{\partial x_j} - \frac{q_i}{T^2}\left(\frac{\partial T}{\partial x_i}\right) - \frac{\partial}{\partial x_i}\left(\frac{q_i}{T}\right) \tag{2.10}$$

Further insight into the content of Equation 2.10 can be obtained by using the relation between conduction heat flux and temperature distribution, namely Fourier's law of heat conduction

$$q_i = -k\frac{\partial T}{\partial x_i}, \qquad i = 1,2,3 \tag{2.11}$$

Where i denotes three directions of coordinates. Thus, Equation 2.10 can be written as

$$\rho\frac{Ds}{Dt} = \frac{1}{T}\tau_{ij}\frac{\partial u_i}{\partial x_j} + \frac{k}{T^2}\left(\frac{\partial T}{\partial x_i}\right)^2 + \frac{\partial}{\partial x_i}\left(\frac{k}{T}\frac{\partial T}{\partial x_i}\right) \tag{2.12}$$

Integrating throughout the interior volume V_{sys}, of a closed surface A_{sys}, we obtain

$$\iiint_{V_{sys}} \rho\frac{Ds}{Dt}dV = \iiint_{V_{sys}} \frac{1}{T}\tau_{ij}\frac{\partial u_i}{\partial x_j}dV + \iiint_{V_{sys}} \frac{k}{T^2}\left(\frac{\partial T}{\partial x_i}\right)^2 dV + \iint_{A_{sys}} \frac{k}{T}\frac{\partial T}{\partial x_i}n_i dA \tag{2.13}$$

The left hand side term is the total entropy change of the fluid particle. The first two integrals on the right hand side are always positive, they represent irreversible entropy production. The third term represents entropy change due to heat transfer in and out of the volume can be positive or negative. Thus the entropy of a fluid particle can only decrease if there is heat conducted out of the particle. Moving the third term of RHS to the left, it becomes

$$\iiint_{V_{sys}} \dot{S}_{gen}\,dV = \iiint_{V_{sys}} \rho\frac{Ds}{Dt}dV - \iint_{A_{sys}} \frac{k}{T}\frac{\partial T}{\partial x_i}n_i dA$$

$$= \iiint_{V_{sys}} \frac{1}{T}\tau_{ij}\frac{\partial u_i}{\partial x_j}dV + + \iiint_{V_{sys}} \frac{k}{T^2}\left(\frac{\partial T}{\partial x_i}\right)^2 dV \tag{2.14}$$

where $\dot{S}_{gen}$ is the entropy generation rate per unit volume, it is the sum of two components-viscous and thermal dissipation

$$\dot{S}_{visc} = \frac{1}{T}\tau_{ij}\frac{\partial u_i}{\partial x_j} \tag{2.15}$$

$$\dot{S}_{therm} = \frac{k_{eff}}{T^2}\left(\frac{\partial T}{\partial x_i}\right)^2 \tag{2.16}$$

For Newtonian fluids, shear stress tensor can be written as,

$$\tau_{ij} = \mu\left(\frac{\partial u_i}{\partial x_j} + \frac{\partial u_j}{\partial x_i}\right) \tag{2.17}$$

Combining Equation 2.15 and Equation 2.17 produces

$$\dot{S}_{visc} = \frac{1}{T}\mu\left(\frac{\partial u_i}{\partial x_j} + \frac{\partial u_j}{\partial x_i}\right)\frac{\partial u_i}{\partial x_j} \tag{2.18}$$

$$\dot{S}_{visc} = \frac{1}{T}\mu_{eff}\left\{ \begin{array}{c} 2\left[\left(\frac{\partial u_1}{\partial x_1}\right)^2 + \left(\frac{\partial u_2}{\partial x_2}\right)^2 + \left(\frac{\partial u_3}{\partial x_3}\right)^2\right] + \left(\frac{\partial u_1}{\partial x_2} + \frac{\partial u_2}{\partial x_1}\right)^2 \\ + (\frac{\partial u_1}{\partial x_3} + \frac{\partial u_3}{\partial x_1})^2 + (\frac{\partial u_2}{\partial x_3} + \frac{\partial u_3}{\partial x_2})^2 \end{array} \right\} \tag{2.19}$$

2.3.2 Pressure Loss Coefficient

The pressure loss coefficient is a common definition for aerodynamic loss esti-
mation. In the experiments, the total pressure is always used as a direct measure of
the energy content of the flow field. This subsection illustrates the reason why it
could be done. The Gibbs equation for a control volume is (Cengel and Boles (2002)):

$$dh = Tds + vdP \tag{2.20}$$

For an ideal gas, $dh = c_p dT$, where h is the enthalpy and c_p is the specific
heat at constant pressure. Therefore Equation 2.20 becomes

$$ds = c_p\frac{dT}{T} - \frac{1}{\rho T}dP \tag{2.21}$$

Since the linear cascade is open to the atmosphere, and once at steady operating
conditions the wind tunnel does not appreciably raise the temperature of the flow, it
could be assumed for these experiments that the cascade is adiabatic, hence $dT = 0$.
Using the equation of state for an ideal gas ($Pv = RT$), Equation 2.21 becomes

$$ds = -R\frac{dP}{P} \tag{2.22}$$

The pressure term in Equation 2.22 is defined as total pressure. By using total pres-
sure between any two states, the total pressure change in a control volume is obtained.

$$P_{0,2} - P_{0,1} = e^{-\frac{\Delta s}{R}} \tag{2.23}$$

In Equation 2.23, Δs refers to the entropy increase which associated with all loss

mechanisms acting on the cascade fluid. The aerodynamic loss can be termed as a reduction in total pressure. For this reason, total pressure measurement is used to determine the efficiency of the turbine.

2.4   Secondary Loss Reduction Methods

Secondary loss can account for 30%-50% of the total aerodynamic loss, according to Sharma and Butler (1987). In order to increase the efficiency of turbomachinery, it is important to take methods to reduce secondary loss. There have been many efforts to improve performance including the end-wall contouring, leading edge modification and end-wall fence.

2.4.1   End-wall Contouring

The non-axisymmetric end-wall contouring is an effective secondary flow reduction method studied by many research groups. The principle of this method is varying the pressure gradient by changing the end-wall profile. Rose (1994) pioneered the concept of using a non-axisymmetric end-wall profile to alter the static pressure distribution. A three-dimension end-wall profile was designed in both axial and circumferential direction. The CFD results show that the end-wall contouring leads to a 70% reduction of the static pressure non-uniformities. Yan et al. (1999) used Rose's basic principles to design the end-wall profile. The end-wall uses convex curvature and concave curvature surface to change the local static pressure. Both experimental and CFD results indicate a reduction of 20% in pressure loss by using the three-dimension end-wall contouring method.

Harvey et al. (1999) designed the non-axisymmetric end-wall by using the linear design system proposed by Shahpar et al. (1999) as shown in Fig. 2.8. The CFD results show that the exit flow overturning and underturning are largely reduced, the two legs of the horseshoe vortex are appropriately controlled by the convex and concave profile. Hartland et al. (1999) validated the CFD prediction of Harvey et al. (1999) by measuring the flow filed and distribution of end-wall static pressure. The

experimental data generally agree with the CFD results. Compared with the baseline case, the net secondary loss is reduced by 30%. Ingram et al. (2002) performed an experiment in Durham cascade to study the effect of the second generation end-wall profile based on the design of Harvey et al. (1999). The secondary loss can be reduced by about 24% relative to the smooth case. Brennan et al. (2001) redesigned the high-pressure turbine of the Rolls-Royce Trent series engine. Secondary loss can be reduced by about 0.24% and 0.16% for Nozzle Guide Vane (NGV) and Rotor respectively. The total stage efficiency is increased by 0.4% with the addition of non-axisymmetric end-wall. Snedden et al. (2009, 2010) employed the generic end wall to the rotor blade. The rotor efficiency can be improved by 0.4% due to the influence of the non-axisymmetric end-wall on the secondary flow structure.
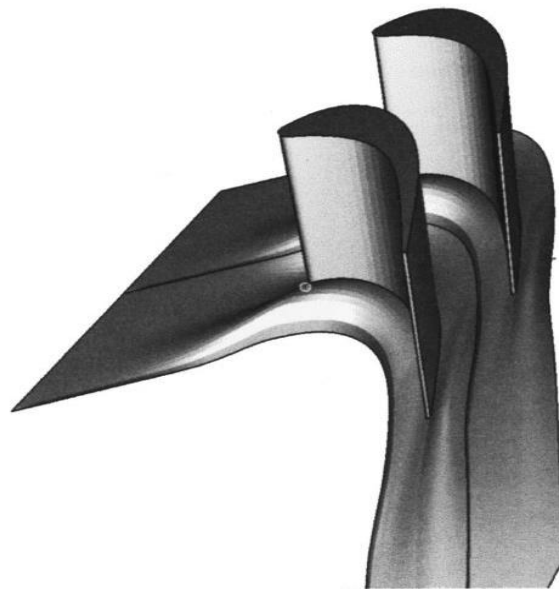
Figure 2.8: Perspective view of final profiled end wall design. (Harvey et al. (1999))

Different non-axisymmetric end-wall design methods were proposed in the later research. Saha and Acharya (2008) profiled the end-wall by combining two curves which vary in the streamwise and pitchwise direction respectively. The numerical results show that the total pressure loss is lower than that in the smooth end-wall case. Praisner et al. (2013) used a gradient-based optimization algorithm to design the end-wall for the low-pressure turbine. The numerical prediction shows that the non-axisymmetric end-wall contouring is effective in reducing passage vortex and pressure loss. Schobeiri and Lu (2014) designed the end-wall profile by continuous

diffusion method which can be applied to both high-pressure and low- pressure turbine. The second rotor efficiency can be increased by 0.5% with the addition of non-axisymmetric end-wall.

Another method for minimizing secondary flow losses is using axisymmetric end-wall contouring. The earliest study was done by Deich et al. (1960). They tested the S-shape end-wall and found efficiency is improved for the low aspect ratio stages. Morris and Hoare (1975) studied the axisymmetric contouring in the vane cascade, the results show that losses can be successfully reduced especially the low aspect ratio passage. Kopper et al. (1981) carried out experiments at a higher outlet Mach number, the mass-averaged total pressure loss is reduced by 17% from the experimental measurement. Dossena et al. (1999) presented both experimental and numerical results in a NGV with S-shape contoured end-wall. Compared with the baseline case, the secondary losses are reduced by 26%. Other relevant studies are presented by Boletis (1985), Moustapha and Williamson (1986), Warner and Tran (1987), Burd and Simon (2000) and Piggush and Simon (2013).

2.4.2 Leading Edge Modifications

Modification to the leading edge is another approach to reduce secondary loss by varying the initial development of the horseshoe vortex. Sauer et al. (2001) designed a bulb geometry at the leading edge of the turbine blade in a low-speed wind tunnel. The results show that the suction side leg of the horseshoe vortex is strengthened by the bulb geometry. As the passage and counter vortex have the opposite rotating direction, the strength of the passage vortex can be weakened. Compared to the baseline case, the secondary loss is reduced by 47%. However, the overall loss may be increased due to this mechanism. No experiment results of overall loss and measurement in the blade passage are available in the open literature.

Another type of airfoil modification that has been successful in reducing the strength of the horseshoe vortex and the associated losses is leading edge fillet. Zess and Thole (2002) performed the experimental study on leading edge fillet in vane cascade. The Laser Doppler Velocimeter system (LDV) was used to obtain the flow field in the vane passage. Their results reveal that the fillet design is effective in

accelerating the incoming boundary layer and reducing the turbulent kinetic energy (TKE) and secondary kinetic energy. As a result, the strength of horseshoe vortex is reduced. The CFD prediction is in a good agreement with the experimental measurements and verified the benefits of the leading edge fillet in eliminating the horseshoe vortex.

To learn more about these promising geometries, Becz et al. (2003, 2004) compared both Sauer bulb and fillet configurations in a large-scale cascade as shown in Fig 2.9. Their 2003 results indicate that the large bulb geometry does not reduce total loss, while the small bulb and fillet geometries show equal area-averaged total loss reduction of 8%. The 2004 study measured the mass-averaged total pressure loss coefficient by using the multi-hole probe. The experimental results show that the bulb geometry has no benefit in loss reduction, while the fillet geometry can reduce overall mass-averaged loss by about 7.3%.

Figure 2.9: The small bulb, large bulb, and fillet geometries shown at the airfoil leading edge and end-wall junction. (Becz et al. (2003))

2.4.3 End-wall Fence

The end-wall fence is a spanwise protrusion on the end-wall that typically extends from the leading edge to trailing edge of the blade passage. The principle of

the end-wall fence is to alter the cross passage flow away from the suction side by employing a single fence to the end-wall surface.

The end-wall fence has been studied extensively for secondary flow control in a duct. Camci and Rizzo (2002) used a 90-degree duct to study the turbine passage without considering the horseshoe vortex. The single fence device with several heights and widths were investigated to achieve better aerothermal effects. They found the full-length fence can weaken the secondary flow the most and a reduction in loss coefficient was reported. The results also indicate that the end-wall fence significantly influences the level of convective heat transfer coefficient, both thick and thin fences increase the end-wall heat transfer throughout the turning duct. Cho et al. (2011) carried on Camci and Rizzo (2002)'s work to optimize the single fence geometry by using the same 90-degree duct. An approximate method was employed to reduce the computational resource. The optimized design reduced the averaged total pressure loss and the area-weighted average maximum Nusselt number by 8.6% and 2.5% respectively.

The single end-wall fence concept has also been applied into turbomachinery. It was originally conceived by Prumper (1972, 1975) who investigated over 400 end-wall fence configurations and found that employing the single fence along the middle line of the passage produce lower losses. Kawai (1994) installed the fence with several heights on the end-wall as well as blade suction surface. The most effective control was achieved when the fence height equaled to 1/3 of the undisturbed boundary layer thickness and placed in the middle of the blade passage.
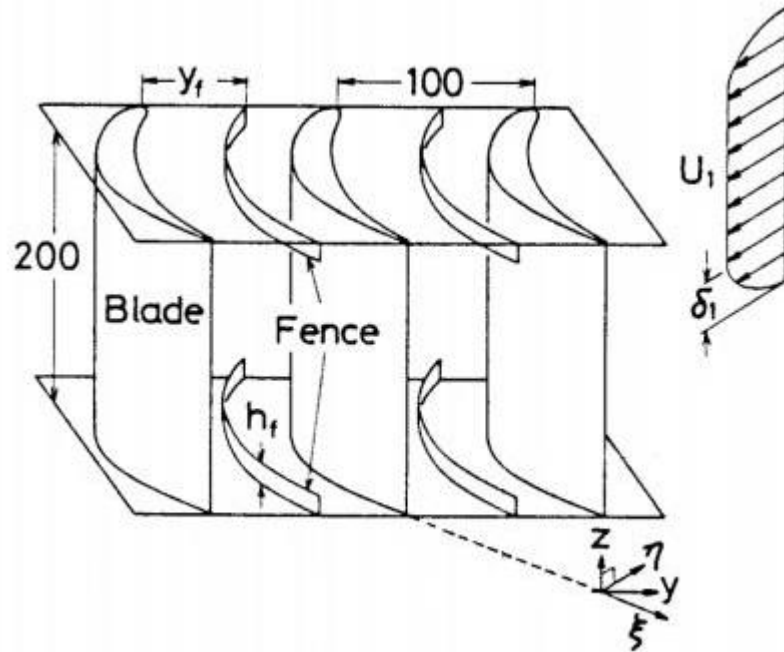
Figure 2.10: Cascade with end-wall fence. (Kawai (1994))

Chung et al. (1991) and Chung and Simon (1993) used the flow visualization method and LDV measurement to study the effect of a triangular-shaped fence on secondary flow control. The results show that the strength of the vortical motion is largely reduced by the end-wall fence, especially for the pressure side leg of the horse vortex.

Latterly, Govardhan et al. (2006) and Zhong et al. (2008) investigated end-wall fence with different length, height, and pitch-wise installation location. The fence under investigation was also found effective in preventing the development of the horseshoe vortex filament on the pressure surface.

However, the single fence can enhance the heat transfer and likely be burnt down due to the lack of extensive protection by the coolant. Such configuration is unrealistic for the real engine condition.

2.5 End-Wall Heat Transfer and Cooling Techniques

As discussed in Chapter 1, the gas turbine engine efficiency can be improved by increasing the rotor inlet temperature. Therefore, turbine entry temperature has been continuously increased over the past decades and achieve to 2500°F–2600°F which is much higher than the permissible metal temperatures for the gas turbine engines nowadays. In order to obtain the safe operational condition for the blade and vane, additional cooling methods should be introduced.

For the blade leading edge region, the high heat load is experienced due to the hot mainstream stagnating. Thus, both internally and externally cooling methods have to be employed in this is region. The jet impingement is always applied inside the turbine blade, while film cooling holes are employed to provide a cooling film to protect the outside surface. For blade trailing edge, the relatively thin region provides the limited surface area to dissipate the heat. Generally, the pin-fins are employed in the trailing edge to increase the heat transfer area and provide structural support. In the tip region, the accelerating flow through the narrow clearance gap between the tip and casing leads to high heat transfer. Externally, film cooling is generally used to protect the blade tip region.

For brevity, the cooling for the blade and tip region, blade leading and trailing edge are not discussed in this section. Han (2004) summarized the cooling techniques for the turbine blade edge region. The literature review presented in the followed sub-sections will only focus on the end-wall cooling.

Compared with the tip region, blade leading and trailing edge, the end-wall region receives less attention. However, the end-wall has a large area which interacts with the hot gases directly. As the rotor inlet temperature increases, the heat load can result in premature failure of the blades or end-wall. The highly three-dimensional secondary flow in the cascade also underpins the thermal performance. Therefore, the blade and vane end-wall in advanced engines also require specific cooling strategy. Different end-wall cooling techniques are reviewed by Wright et al. (2014) and Bogard and Thole (2012) in detail.

The followed subsections will first discuss the end-wall heat transfer and then focus on different end-wall cooling techniques.

2.5.1   End-wall Heat Transfer

In order to investigate the cooling schemes to protect the turbine end-wall adequately, it is necessary to improve the understanding of the secondary flow in the turbine passage. This complex, three-dimensional secondary flow aerodynamic has been introduced in the previous section of this chapter. This subsection will focus on the heat transfer effect by the secondary flow.

Heat transfer on the end-wall region is related to the secondary flow structure directly. The flow structures and their influences on film-cooling and heat transfer were reviewed by Langston et al. (1977), Langston (1980, 2001), Chyu (2001), and Simon and Piggush (2012). For the blade leading edge, high heat transfer coefficient existences due to the formation of the horseshoe vortex. In the downstream of the passage, elevated heat transfer coefficient is caused by the merging of the pressure side leg of the horseshoe vortex and the passage vortex. For the trailing edge region, an enhanced heat transfer occurred due to the mixing of vortex between adjacent passages.

A variety of papers have presented the contour of the heat transfer coefficient by using different methods. Blair (1974) pioneered the investigation of end-wall heat transfer. He used many thermocouples and heaters to measure the heat transfer coefficient in a turbine vane passage. The results show that the large vortex located in the corner between the end-wall and the suction surfaces can produce large variations of heat transfer across the vane gap in the trailing edge region. Graziani et al. (1980) also found these variations in the end-wall heat transfer coefficient by using a similar method as that in the Blair (1974)'s experiment but with higher spatial resolution. The heat transfer coefficient on the suction surface is influenced by the passage vortex, while the heat transfer coefficient on the pressure surface is not affected by the secondary flow. York et al. (1984) used thermocouples attached on each side of the nickel wall to measure the heat flux. The results sustain the work of Blair (1974) and Graziani et al. (1980), similar variations of heat transfer were found.

Hylton et al. (1983) performed heat transfer measurement in an uncooled linear cascade end-wall and found that the Stanton number near the blade leading edge is about three times higher than that at mid-pitch of the passage entrance. Goldstein and Spores (1988) examined the local transport coefficients for two different end-wall boundary layer thicknesses and two free-stream Reynolds numbers by using the mass transfer analogy. Figure 2.11 shows the effect of secondary flow on heat transfer. The largest heat transfer enhancement occurs near the leading edge due to the horseshoe vortex. The other two peaks of heat transfer are the results of passage and corner vortex.
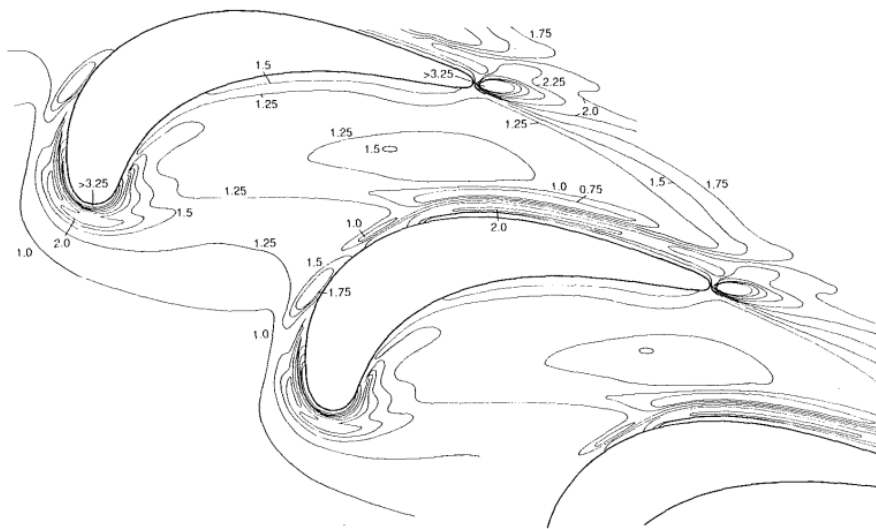
Figure 2.11: Mass (heat) transfer contour on turbine end-wall (Goldstein and Spores (1988)).

Mainstream turbulence effect is considered in the later research. High turbulence intensity and large turbulence scales always occur when the flow exits the combustor. This high turbulence leads to an earlier transition of the boundary layer which increases the end-wall heat transfer. Thole et al. (2002) measured the flow field and heat transfer in a turbine vane with two different turbulence levels. They reported that the horseshoe vortex is moved close to the leading edge slightly for high turbulence level. In general, the high freestream turbulence increases the end-wall heat transfer. Lee et al. (2002)'s research also indicates the same trend.

2.5.2 End-wall Film Cooling

The basic principle of end-wall film cooling is using internal coolant air ejected out through discrete holes to provide a coolant film to protect the outside surface of the end-wall from hot combustion gases. As the local areas of high heat transfer identified, the film cooling holes can be implemented on the end-wall to reduce the heat load in these areas.

Takeishi et al. (1989) carried out an experiment to investigate the film cooling and heat transfer on the vane end-wall. Discrete film cooling holes were employed at three different locations along the passage. They found the film cooling effectiveness decreases while the heat transfer increases near the blade leading edge due to the effect of horseshoe vortex. The path of the coolant is largely affected by the migration of the passage vortex. Harasgama and Burton (1991, 1992) measured heat transfer on the platform of NGV. Film cooling holes were located along an iso-Mach line near the blade leading edge. The results show that the secondary flow can convect the coolant towards the blade suction side. Therefore, the coolant cannot protect the region near the blade pressure side and trailing edge. Jabbari et al. (1996) placed discrete film cooling holes at the downstream of the turbine blade passage. The result is similar with the work of Takeishi et al. (1989) and Harasgama and Burton (1991, 1992), which indicates that the uniform coolant coverage cannot be provided by discrete film cooling holes due to the cross pressure gradient.

Friedrichs et al. (1995, 1997, and 1998) found that evenly spaced rows of film cooling holes cannot provide uniform coolant protection due to the strong secondary flow. The location of the film cooling holes should be designed based on the end-wall flow structure. They used a new measurement technique to obtain the film cooling effectiveness distribution on the turbine end-wall. The technique was based on the reaction between the ammonia and the diazo. With their improved design, more coolant coverage can be observed in the majority of the passage. However, the region near the leading edge and blade suction side is still difficult to protect due to the existence of the horseshoe and corner vortex.

Barigozzi et al. (2006) improved the shape of the film cooling hole to investigate the geometry effect on the aero-thermal performance of a nozzle vane cascade. Two

film cooling hole geometries, cylindrical and fan-shaped, were employed to compare the film cooling effectiveness on a passage end-wall. They found that the passage vortex is weakened and cross flow in the passage is reduced as the blow ratio increases, therefore, a more uniform coolant coverage is observed across the passage. Although fan-shaped holes have better cooling performance than cylindrical holes, the cooling effectiveness is increased only in the upstream region for both cases.

End-wall film cooling has also been investigated by Goldman and McLallin (1977), Sieverding and Wilputte (1981), Bario et al. (1989), Han (2012). All these works deliver a consensus that the secondary flow has a strong detrimental impact on film cooling on the end-wall.

2.5.3   Leading Edge Modification and End-Wall Contouring

Aerodynamically, leading edge modification can reduce the strength of the horseshoe vortex, while end-wall contouring can change the pressure gradient cross the baled passage. The heat transfer and cooling performance of these two methods have also been studied.

Han and Goldstein (2006) placed a fillet geometry at the blade leading edge to study the mass transfer coefficients on end-wall. The results show that the fillet significantly reduces the horseshoe vortex and delays the passage vortex migrating to the suction side. However, the strength of the passage vortex has no difference with the no fillet case. The near wall corner vortices are enhanced by the fillet and generate a high mass transfer region. Mahmood et al. (2005) measured four different leading edge fillet profiles in a low-speed linear turbine cascade. They found the fillets lead to the passage vortex moves closer to the suction side of the baled in the passage. The optimized fillet which has a concave profile can reduce the Nusselt number significantly compared to the baseline. However, no reduction of total loss coefficient is observed. Lethander et al. (2003, 2004) optimized a leading edge fillet geometry to obtain the maximum thermal benefit. The results indicate that although large fillet can reduce the strength of the horseshoe vortex and increase the thermal benefit, the total pressure loss is slightly increased.

Since the addition of leading edge fillet increases the heat exchange area in the

stagnation region, some studies focused on cooling the fillet. The patent of Liang (2006, 2009) provided a new approach to cool the leading edge fillet and reduce the secondary flow. Film cooling and leading edge fillet were combined by adding a variety of film cooling holes on the fillet surface. Because the additional effort is needed to cool the fillet, the use of leading edge modification has not become widespread.

Many research groups investigated the effect of end-wall contouring on the reduction of heat transfer and aerodynamic loss. Barigozzi et al. (2010) studied the effect of purge air flow in a nozzle vane. The results indicate that the direct impact of contouring on coolant coverage depends on the site of coolant ejection related to the contouring. Lin et al. (2000) performed a numerical investigation to study the end-wall heat transfer in an NGV passage with axisymmetric end-wall contouring. They found both the secondary flow and the heat transfer coefficient is reduced. Thrift et al. (2011) studied the axisymmetric end-wall contouring effect on the cooling performance. Film cooling holes were distributed near the blade leading edge and pressure side of the passage. Compared with the flat surface, the end-wall contouring can increase the coolant coverage from the upstream cooling holes, while the cooling effectiveness in the downstream region is decreased with the addition of end-wall contouring.

2.5.4 Purge Air Cooling

Figure 2.12 shows the secondary air system in an aviation engine. The region between the stator and rotor is called stator-rotor cavity and the flow restriction located at the outer edges of the cavity is the rim seal which is shown in the zoom-in part of Fig. 2.12 (Rolls Royce (2015)). As the turbine disc rotates, the air acceleration causes the pressure inside the stator-rotor cavity decreasing, the high pressure in the main gas path forces hot gas into the cavity. The ingestion of high-temperature gases has become an issue, it can lead to the discs overheating, thermal fatigue and uncontrolled dilatation rates of the rotor discs and bearings (Paniagua et al. (2004)). In order to avoid the penalty caused by hot gases ingestion, continuously expelling bypassed compressor purge air is injected through the rim seal between the rotating

and stationary parts. The goal is to oppose the inward flow of hot gas and to cool down the disc.
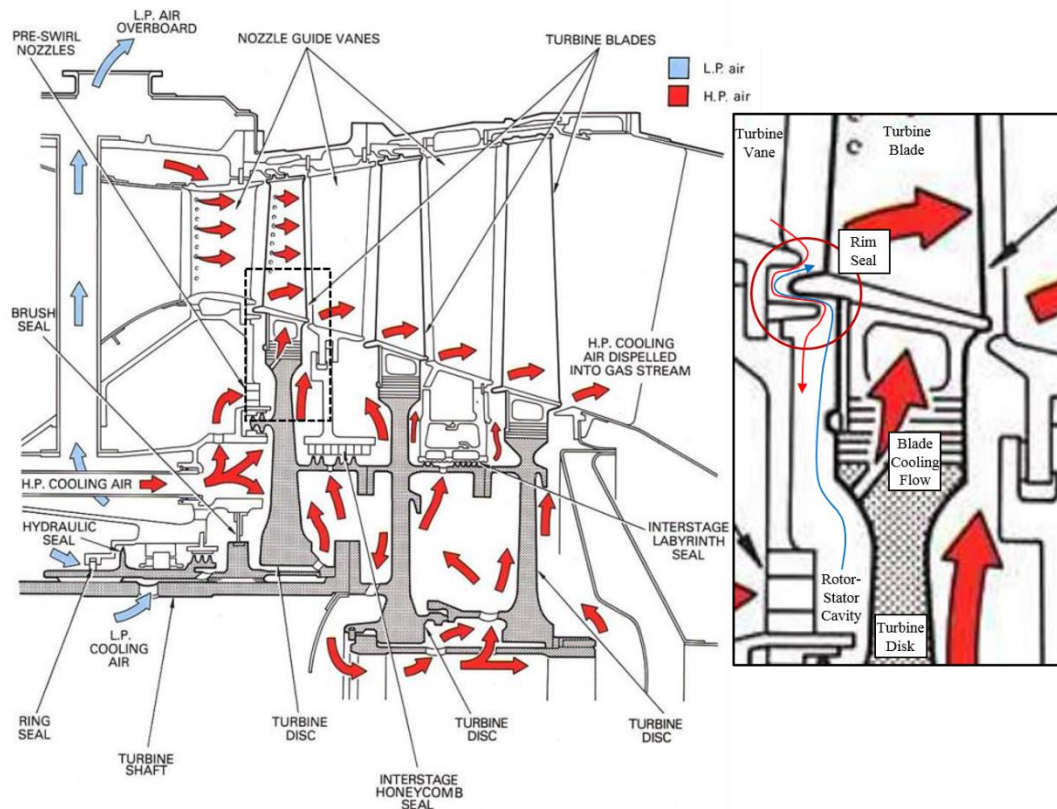
Figure 2.12: Schematic of a secondary air system for an aviation engine (Rolls Royce (2015)).

Some early purge air studies focused on the simplified cavity configurations and the heat transfer problems inside the cavities. Bunker et al. (1992a) measured the heat transfer coefficients distribution in rotating and stationary discs by using the Thermochromic Liquid Crystal (TLC) method. Hub purge air injection was investigated over a wide range of the flow control parameters. The results show that stator heat transfer is sensitive to the mixed fluid temperature, while rotor heat transfer depends on the spacing between the stator and rotor. Bunker et al. (1992b) further employed three basic cavities to investigate the rotor heat transfer coefficients in more realistic cases. Comparisons of various radial distributions of rotor heat transfer coefficient they found that overall rotor heat transfer is optimized in the present geometry by either a median location of radial injection or by hub injection. Wilson

et al. (1997) performed a Direct Navier-Stokes (DNS) calculation to predict the highly unsteady flow within a rotating cavity, simulating the realistic working condition. Owen and Wilson (2001) reviewed the recent computational and experimental research on rotor-stator systems with pure air flow. Ingress of hot mainstream gases, pre-swirl cooling-air supply systems and cooling air flows in rotating cavities were summarized to improve the detailed understanding of the complex flow phenomena.

Achieving the sealing and cooling of the turbine discs using minimal purge air plays an important role in turbine design. There have been a large number of papers describing the effect of different rim seal geometries on the interaction of purge and mainstream. De la Rosa Blanco et al. (2009) studied the effect of a backward and forward-facing step rim seal geometry and the purge air flow ratio. They found the end-wall secondary flow is strengthened and the mixing loss is increased with forward-facing step geometry. Marini and Girgis (2007) numerically analyzed two rim seal shapes: recessed and raised leading edge in a transonic high-pressure turbine. The results show that end-wall passage vortex structure and location can be affected by the rim seal shape and cavity flow. The stage efficiency is increased by using a raised leading edge shape at the real engine condition. Schuler et al. (2010) also numerically investigated the effect of different rim seal geometries on the aerodynamic loss mechanism. A compound geometry which is similar to the raised leading edge shape of Marini and Girgis (2007) and a simple axial gap geometry was used in a turbine rotor. Compared with axial gap geometry, the total pressure loss coefficient is reduced due to the thinner boundary layer produced by compound geometry. Recently, Popović and Hodson (2013b) presented numerical and experimental results from a linear cascade with purge air injection. The first paper reported the effect of an upstream overlapping seal geometry with forward and backward facing annulus steps. It was found that the rim seal clearance should be reduced in both radial and axial direction to improve the sealing effectiveness. In the second paper, Popović and Hodson (2013c) investigated several engine realistic rim seals. The simple axial geometry and overlapping seals were all considered in this study. The size and the location of the recirculation zones within the rim seal are found to be the most important feature that affects the overall loss and sealing effectiveness. The findings

from above investigations show that the rim seal geometry is an important consideration for not only sealing effectiveness but also mainstream losses.

Besides the geometry of the rim seal, the mainstream-purge air flow interaction also received many attentions. McLean et al. (2001a) presented one of the first studies of the secondary aerodynamic effects of wheel space coolant mixing with the mainstream flow. The experiment was performed in a cold-flow turbine rig at the AFTRF. The exit flow surveys with and without cooling injection in the stationary frame were measured using both five-hole and modified Kiel probes. Three different types of purge air injection configuration (root, radial and impingement injection) were studied. The results show that the exit flow condition can be largely affected by a small quantity of purge air. The root shows the strongest changes in total-to-total efficiency, the passage-averaged efficiency increase is over 1.5 percent due to affect the magnitude of over-turning and under-turning. McLean et al. (2001b) also investigated the relative aerodynamic effects associated with purge air injection in the rotating frame. The exit flow angles and velocity field were measured in detail. The results indicate that the effects of small purge air injection into the mainstream of a high-pressure turbine stage can be very significant and should not be neglected on the aerodynamic analysis. The cooling air is affecting the structure of the three-dimensional secondary flow and inlet rotor boundary layer, which in turn has a large effect on the three-dimensional exit flow and stage performance. Girgis et al. (2002) tested a transonic turbine with various secondary air injection conditions. Cavity flows with a large tangential component allow an improvement of 10.3% efficiency compared to the case of flow injected radially. Paniagua et al. (2004) analyzed the interaction of purge flow with the mainstream flow in a high-pressure turbine. Three purge flow ratios (0.5%, 0.6% and 1.5%) were tested under the engine representative conditions. They found that the purge air flow reinforces the intensity of the rotor hub vortex and enhances its migration towards mid-span. Reid et al. (2006) reported that increasing purge flow ratio can reduce the turbine efficiency, while swirling the purge flow can diminish this adverse effect. Similar results have also been found in the studies by De la Rosa Blanco et al. (2009), Popović and Hodson (2013a) and Lynch et al. (2013). Schuepbach et al. (2010) performed steady and unsteady meas-

urements in a turbine stage to examine the effects of purge air-mainstream interaction. The results show that with a 0.9% increasing of purge flow injection, the total efficiency decreases 0.6%. Additionally, similar to Paniagua et al. (2004)'s work, the strength of the secondary flows and entropy generation through mixing are increased.

As reported previously, purge air is introduced to prevent the hot gases from ingesting into the cavity and provide sufficient coolant to cool down the disc. Blair (1974) first investigated the end-wall protection form upstream purge air. The results show that purge air flow is quickly crossed towards suction side of the blade due to the passage vortex migration. The similar trend is also found in the work of Colban et al. (2002); Hermanson and Thole (2002); Vakil and Thole (2003); Ranson et al. (2005); Thole and Knost (2005); Cardwell et al. (2007). Few studies were related to the potential of using purge air to cool down the end-wall until the investigation of Roy et al. (2000). Roy measured the heat transfer on the vane end-wall for the cases with and without purge air injection by using the Transient Liquid Crystal (TLC) technique. The experimental results indicate that with the injection of purge air, the heat transfer coefficient near the blade leading edge and vane pressure side is reduced. The passage vortex is also weakened thus a more uniform coolant distribution can be observed. Similarly, Dénos and Paniagua (2002) studied the purge air effect in a high-pressure transonic turbine stage. They found the purge air effectively reduces the heat flux around the rotor leading edge.

Later, the research group of University of Minnesota (Burd et al. (2000a, 2000b), Oke et al. (2001), Oke and Simon (2002)) focused on the study of various purge air injection schemes in a NGV. They combined the axisymmetric contoured end-wall with purge air and studied the heat transfer. The purge air flow is injected through a 45-degree inclined slot. Similar to Roy et al. (2000)'s study, the results indicate that most of the purge air is moved to the suction side of the blade at a low purge flow ratio, while better cooling coverage and secondary flow effect reduction occur as the percentage of the purge flow increases to 3.2%. Zhang and Jaiswal (2001) and Zhang and Moon (2003) carried out an experiment to measure the film cooling effectiveness with two different injection geometries: discrete holes and slots. They found for both hole and slot injections, the secondary flow dominates the near end-wall flow field at a lower mass flow, while the cooling film dominates the near wall flow field

and the secondary flow is suppressed at a higher mass flow ratio (above 2.0%).

Nicklas (2001) and Kost and Nicklas (2001) first investigated the end-wall cooling performance by combining purge air cooling with film cooling holes. The vane end-wall film cooling effectiveness and heat transfer coefficient were measured. The results show that higher intensity of the horseshoe vortex due to the coolant ejection from the slot causes a strong increase of the heat transfer coefficients at the end-wall. Coolant ejected from the holes causes a local increase of the turbulence level directly downstream and boosts the heat transfer coefficients in that area. Knost and Thole (2004) designed two patterns of end-wall film cooling hole and combined them with purge air cooling. They found the critical area of the leading edge and the junction between the pressure side and the end-wall can be adequately cooled by increasing the purge air flow. Purge air has been proved to be efficient in protecting the end-wall in the upstream region of the blade passage. However, in the downstream area, the purge air offers minimal coverage as the passage vortex lifts the purge air off the end-wall. Therefore, Wright et al. (2007, 2008a, 2008b) only added several film cooling holes at the passage downstream region. The film cooling effectiveness of different purge slot geometries was measured by the Pressure Sensitive Paint (PSP) technique. The results indicate that the large purge air ratio could not only offer cooling protection to the rear of the blade passage but also result in a large aerodynamic penalty. In addition, combining both upstream purge air and downstream film holes can efficiently increase film cooling effectiveness. Lynch and Thole (2008) studied the effect of purge air ratio and slot width on vane end-wall heat transfer coefficients and film cooling effectiveness. The results indicate that for a fixed purge air ratio, the decreasing of slot width can increase the purge air coverage area. While for a fixed slot width, the heat transfer coefficients and film cooling effectiveness are slightly increased as the purge air ratio increasing. Dannhauer (2008) measured the cooling effectiveness for several purge air configurations in NGV. The experimental data indicate that it is possible to cover the complete end-wall with high leakage fraction and using an appropriate injection geometry. Later, Popović and Hodson (2010) investigated the purge air cooling in a rotor blade and observed that the purge air mainly concentrates around the blade suction surface, resulting in a higher heat transfer coefficient. However, the overall heat load is not reduced.

Most of the researchers studied the purge air cooling in linear cascades or turbine vanes, while few studies focused on investigating the effect of purge air cooling in rotating environment. Suryanarayanan et al. (2009, 2010) first investigated purge air cooling in the first stage rotor under the rotating conditions. Discrete film cooling holes were also located downstream of the passage. They found that the film cooling effectiveness is largely affected by the purge air ratio and the rotational speed. For the downstream discrete film cooling, the film cooling effectiveness and purge air coverage are maximum for the reference speed of 2550 rpm.

2.6   Summary

In this chapter, the fundamental secondary flow theory is first described in terms of pressure gradient and vorticity component. Different secondary flow models are discussed to improve the understanding of this complex flow. Among these models, three common major flow structures; passage vortex, horseshoe vortex and corner vortex are well known, although the production of loss from these features is not currently well understood. The undesirable effects of secondary flow and secondary losses are then discussed. Entropy generation rate is used to predict secondary losses. A number of methods of loss reduction using the enhanced knowledge of the flow field are proposed. Actually, achieving reliable loss reduction methods is quite difficult as a large proportion of authors showed a lack of success in reducing the loss. Three secondary flow reduction techniques which have been shown to be the effective methods of loss reduction are introduced: end-wall contouring, leading edge modifications, and end-wall fence.

The effect of secondary flow on end-wall heat transfer and different end-wall cooling techniques are discussed. Purge air system is introduced in order to prevent the hot mainstream from ingesting into the cavity between the stator and rotor. The related studies are presented in this section, including simplified cavity configurations and the heat transfer problems inside the cavities, the design of rim seal geometry, and the interaction between the mainstream and purge air flow.

Chapter 3

Experimental Facility and Measurement Techniques

The experimental facility and measurement techniques are introduced in this chapter. Section 3.1 presents the facility employed in this study, including a low-speed wind tunnel, a 90-degree turning duct, a linear cascade test section and a purge air system. Two measurement techniques are then introduced in detail. The principle and data processing of the PIV measurement technique are presented in Section 3.2. The transient thermal measurement method is then explained in Section 3.3. The data acquisition system and flow condition are introduced in the followed section. Finally, the uncertainty in the experimental results is discussed.

3.1   Experimental Facility

3.1.1   Low-Speed Wind Tunnel

A low-speed wind tunnel is employed in the present study, as shown in Fig. 3.1. The wind tunnel consists of five parts, which are air blower, flow conditioner, setting chamber, contraction part and test section. A 25kw air blower is connected to a large-sized flow conditioner. The ambient air enters the centrifugal fan through a bell mouth inlet. The flow exits the fan and passes through a wide-angle diffuser before entering the settling chamber. The diffuser has screens to prevent boundary-layer separation and reduce the flow velocity. In order to obtain the uniform inlet flow and moderate the axial turbulence, the flow straightener and meshes are installed inside the settling chamber. The contraction section is connected to increase the speed of the airflow from the settling duct. The test section is then connected with the contraction. It should be noticed that due to the limitation of the experimental facility, only low-speed experiments are performed in the present thesis.
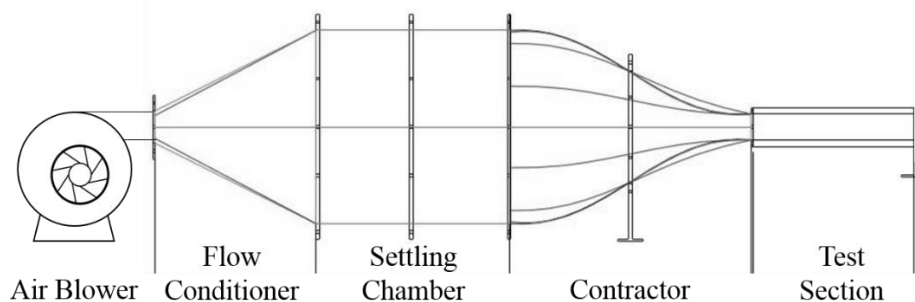
Figure 3.1: Low-speed wind tunnel

3.1.2 90-Degree Turning Duct Test Section

A 90-degree turning duct is firstly used in this study to simulate the turbine passage without considering the complex interactions between the horseshoe vortex and passage vortex. A schematic of the test section is shown in Fig.3.2. The non-dimensional radius ratio of the duct is kept the same as that in the work of Camci and Rizzo (2002). All geometry parameters are normalized with duct width D. The inner and outer radius ratios (r_i/D and r_o/D) are 1.8 and 2.8, respectively. In order to avoid the interaction of the induced passage vortex from the top wall, the duct height H is set to be 2D. The turning duct is equipped with straight inlet and outlet sections, whose lengths are 2.5D. The coordinate system is also shown at the center point of the curved duct. The bottom end-wall on the duct is designed with interchangeable blocks. Three types of end-wall blocks are employed: one smooth wall, one with seven small-scale ribs and one with seven wavy-groove. The end-wall blocks with the engineered surface structure are manufactured through 3D printing. The processing precision of 3D printing is 0.1mm (6% precision level). The bead blasting method is used in the finishing process to remove layer lines. The ribs cover the angular range from 0° to 45°, namely the first half of the turning duct. Figure 3.3 shows a sample of the ribs fabricated by the 3D printing technique. The measured rib array geometry is also summarized in Table 3.1.

Table 3.1: Geometry of rib fence and groove surface structure

h/D	0.05
w/D	0.02
d/D	$\dfrac{1 - 0.02 \cdot n}{n + 1}$
δ/h	4

Figure 3.2: 90-degree turning duct test section
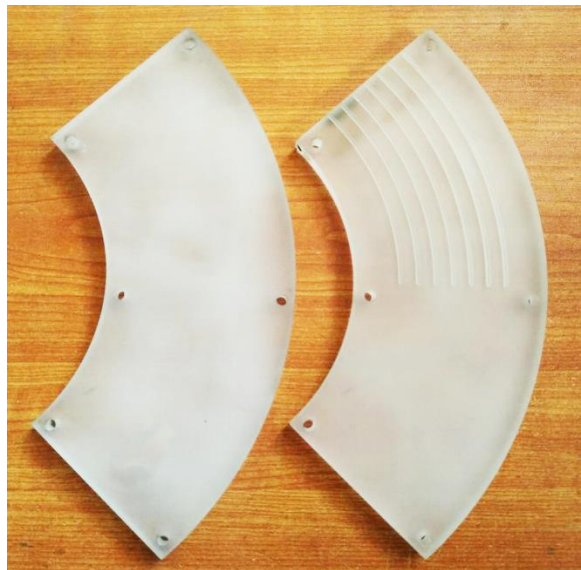
Figure 3.3: Interchangeable end-wall with smooth and ribbed surface for 90-degree turning duct.

3.1.3 Linear Turbine Cascade Test Section

A linear turbine cascade test section is connected with the low-speed wind tunnel. The test section contains four blades and three flow passages, as shown in Fig. 3.4. The turbine blade profile is similar to the one studied by Wright et al. (2008b). The size of the blade is scaled up by a factor of 1.65 to fit the dimension of the contraction exit, and the details of the blade geometry are summarized in Table 3.2.
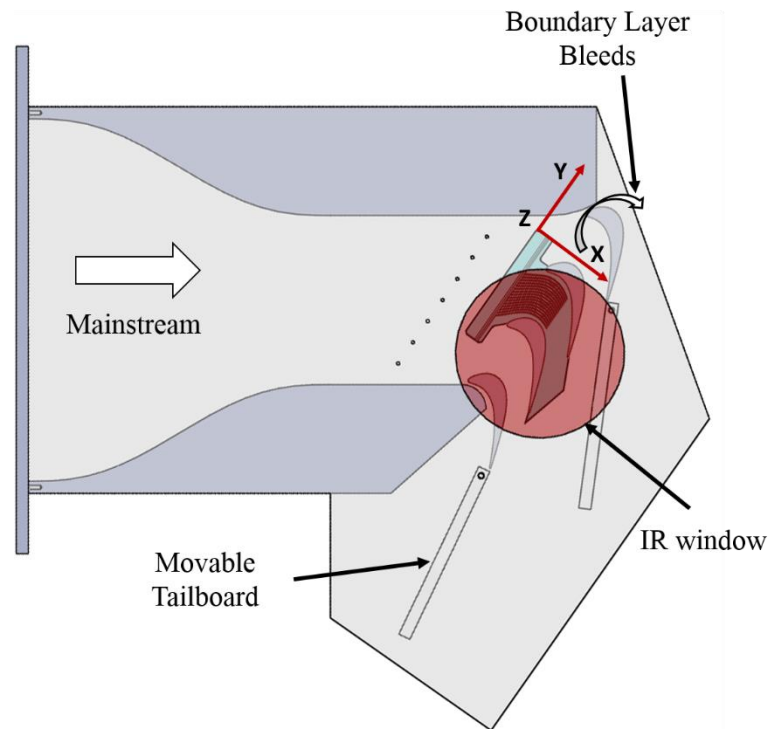
Figure 3.4: Linear cascade test section

Near the suction-side sidewall, two boundary layer bleeds, and two movable tailboards are designed and adjusted to deliver a reasonable flow periodicity. The inlet test section is a rectangular cross-section with dimensions of 130 mm (W) by 80 mm (H). The inlet velocity is maintained at 20 m/s, and the turbulence intensity at the test section inlet is about 1%.

Two types of end-wall, smooth and ribbed are used in the experiment. On the ribbed end-wall surface, the ribs start from the rim seal exit to 55% chord downstream of the blade leading edge. The interchangeable end-wall is also made by 3D printing, and the material has a very low thermal conductivity. The detachable end-

wall samples with the smooth and ribbed surface for turbine cascade are shown in Fig.3.5, and the rib array geometry is summarized in Table 3.3.

Table 3.2: Geometry of the high-pressure turbine blade linear cascade.

Axial chord	56mm
True chord	75mm
Span	80mm
Pitch	56mm
Inlet flow angle	35°
Mean exit flow angle	72.49°
Test section passage width	80mm
Test section passage height	130mm

Figure 3.5: Interchangeable end-wall with smooth and ribbed surface for turbine cascade.

Table 3.3: Geometry of ribs array on the end-wall.
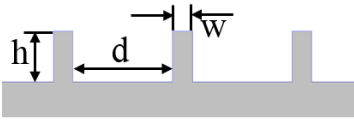
h/P	0.026
w/P	0.017
d/P	0.089
δ/h	4

3.1.4 End-Wall Rim Seal Design

For thermal measurement, both the 90-degree turning duct and linear cascade test-section are equipped with a secondary air system to simulate the purge air injection through the rim seal. Figure 3.6a shows the rim seal geometry used in 90-degree turning duct. An inclined slot on top of the cavity injects the purge air into the turning duct, thus forming the purge air flow. The inclination angle between the slot and the end-wall is 30 degree. The slot spans along the entire duct width and has a width of 0.06 D. The ratio between the purge air velocity and the freestream is 0.86. The choice of the slot dimensions and flow conditions is based on the experiment by Wright et al. (2008a).

(a)   (b)
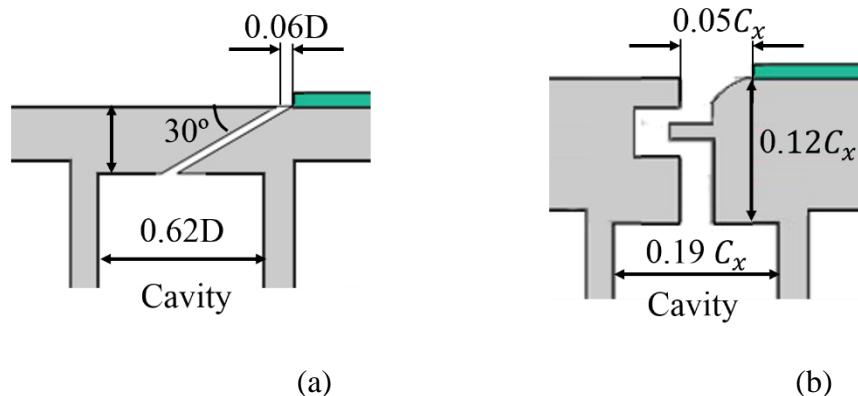
Figure 3.6: Purge air rim seal configuration for (a) 90-degree turning duct and (b) linear cascade test-section

Detailed geometry of the rim seal for linear turbine cascade test-section is also shown in Fig.3.6b. The purge flow enters the wind tunnel through a labyrinth-like rim seal. This rim seal design can effectively prevent the hot mainstream flow from ingesting into the engine cavity and accurately represents the stator-rotor rim seal structure in the real engine. The rim seal is located 22.7% C_x upstream of the blade leading edge and covered a width of 1.5 blade passages. The purge air blowing ratio, which is the ratio between purge air velocity and mainstream velocity, is set as 0.86. The slot dimensions and flow conditions are the same as the experiment of Wright et al. (2008b).

3.1.5   Purge Air Supply System

The purge air supply system is introduced in heat transfer experiment to simulate the purge air injection through the rim seal. It is designed to provide steady and low-temperature purge air and independently control the mass flow rate of the purge air entering the passage. The schematic of the purge air supply system for the heat transfer experiment in 90-degree turning duct is shown in Fig 3.7.
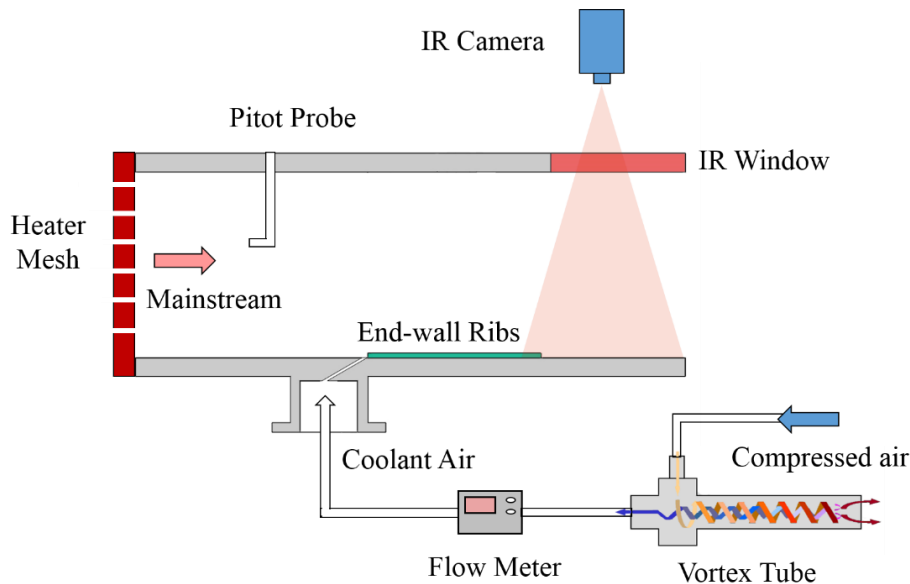
Figure 3.7: Schematic of coolant supply facility and 90-degree turning duct test section

A vortex tube (AiRTX International Company, Model 20035) is used to generate the cold air. Compressed air is injected into the vortex tube through the nozzle and accelerated to a spiral-like rotating vortex flow in the vortex tube chamber. There are two exits for a vortex tube, the exit close to the inlet nozzle is the cold end, while the exit on the other side is the hot end. When closing the control valve of the hot end, a backward flow will generate and move to the cold end. The heat exchange between the forward and backward flow makes the central air cool down. The volume and temperature of the cold air can be controlled by changing the valve opening. The cold end of the tube is then connected to a stabilizing cavity with a steady temperature of 278 K throughout the transient tests. The thickness of the stabilizing cavity is 8mm. In order to inhibit heating up of the cooling flow by surrounding air, the stabilizing cavity and pipes are wrapped by the thermal insulating material. The cooling flow is injected into the turning duct through an inclined slot. Detailed geometry of the rim seal is introduced in Subsection 3.1.4. The volumetric flow rate of the purge air is measured by using a digital flow meter (SMC Company, Model PF2A750-02-27).

The schematic of the purge air supply system for heat transfer experiment in the linear cascade is shown in Fig. 3.8. The purge air supply system is similar to the one used in the turning duct. The compressed air is injected into the vortex tube (AiRTX International Company, Model 20035) to generate cooling air. The cooling flow of 293K then enters the cascade passage through a labyrinth-like rim seal, as shown in Fig. 3.8. The flow rate is measured by the same digital flow meter (SMC Company, Model PF2A750-02-27). The thermal insulating material is also used to maintain the temperature of the cooling flow.

The vortex tube can reduce the temperature of the incoming compressed air by up to 60 K at its maximum cooling capacity. But the actual temperature decrease is dependent upon room temperature. It should be noticed that the heat transfer experiment for duct and cascade is performed in winter and summer respectively. Therefore, the cooling air temperature in cascade experiment is relatively higher.

In order to check the uniformity of purge air injected through the rim seal, the end-wall surface temperature is first measured without turning on the wind tunnel. Only compressed air is provided to obtain the cold purge air. The overall uniformity

of the purge air is satisfactory according to end-wall surface temperature distribution.
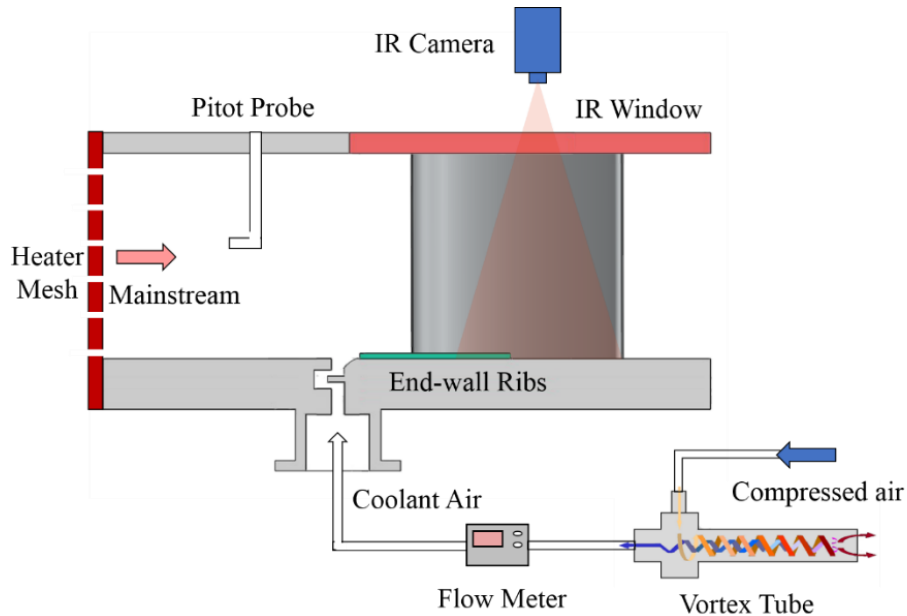
Figure 3.8: Schematic of coolant supply facility and linear cascade test section

3.2 PIV Experiment

Particle Image Velocimetry (PIV) technique was used to measure the velocity field information at the exit of the 90-degree turning duct to confirm the effect of end-wall ribs. Different PIV techniques and applications have been reviewed by many researchers (Adrian (1986, 1991, 2005); Lauterborn and Vogel (1984); Dudderar et al. (1988); Buchhave (1992); Prasad (2000); Grant (1997)). This section will briefly introduce the PIV principle, and present the procedure of data processing, and experimental setup for this research.

3.2.1 2D PIV Principle

Particle Image Velocimetry (PIV) is an optical flow visualization method used to obtain instantaneous flow field velocity and related properties in fluids. Figure 3.9 briefly shows a typical schematic of the PIV setup in a wind tunnel. The fluid is

seeded with small particles which are assumed to follow the flow faithfully (Raffel et al. (2018)).

The laser beam has the property of being monochromatic, which means that waves are sent with one single frequency. Then, the laser beam has to be expanded and diverted by an optical system in order to achieve the desired illuminated geometry. In the case of 2D PIV, the targeted geometry is a vertical plane parallel to the duct exit. The laser sheet illuminates a plane within the flow field twice. The time delay between two laser pulses depending on the mainstream velocity.

Once the laser system is properly set, the cameras can record PIV images. Since the frequency of the recording is very high (in the order of 1 kHz), a mode called multi-frame/single-exposure has been used. When the laser emits light pulses, the camera starts recording one image for each pulse. Two of these images form a frame, which will have a certain time span between both images.

Two images shortly after each other are used to calculate the distance of individual particles moved within this period. Finally, the velocity can be calculated from the measured distance and the known time difference. This technique has a lot of advantages in comparison to other techniques because it allows an accurate visualization of all the targeted particles in the fluid.
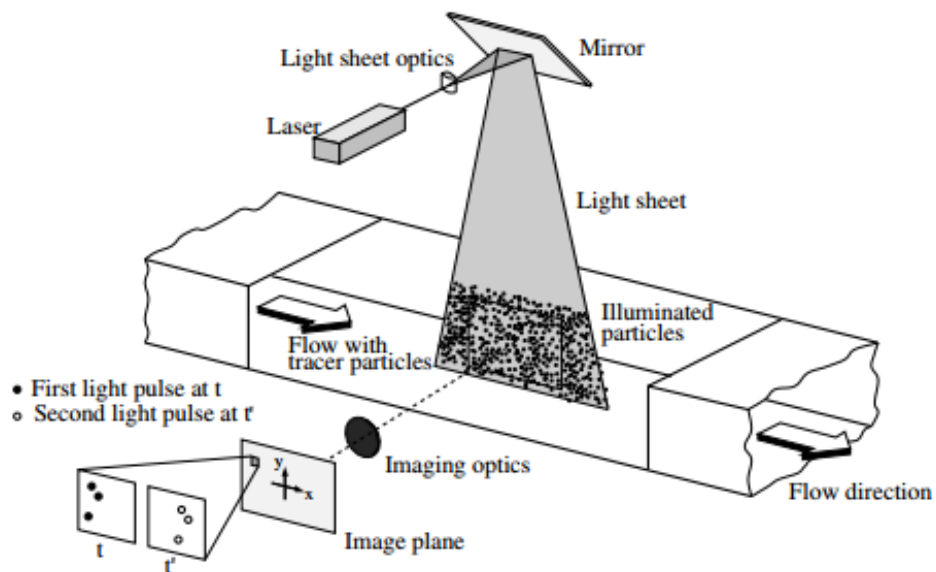
Figure 3.9: A schematic of 2D PIV setup in a wind tunnel (Raffel et al. (2018)).

Pictures belonging to the same frame are cross-correlated to obtain velocity fields. The first step of this process is dividing each image into many squared sub-areas. Each sub-area which contain several pixels will be individually considered to build one velocity vector. These areas are called interrogation areas. The post-processing software will compare the intensity of the pixels in each interrogation area by following a specific algorithm, the corresponding vector which represents the most repeated displacement of particles can be calculated. Then this algorithm is repeated over the whole bitmap to elaborate the velocity field.

The image at time t is exposed by a light pulse and recorded on one frame of the camera, the image intensity is

$$I_1(X) = I(X,t) = \int \mathcal{I}(z)\tau_0[X - F(x)]g[x - x_p(t)]dx \qquad (3.1)$$

Where $\mathcal{I}(z)$ is the beam intensity, τ_0 represents the exposure of a particle image per unit of beam intensity, and $g[x - x_p(t)]$ is the Lagrangian position of each particle.

Then the image from $t + \Delta t$ is exposed and recorded in a second frame, the image intensity field for the time of the second exposure is

$$I_2(X) = I(X,t + \Delta t) = \int \mathcal{I}(z)\tau_0[X - F(x)]g[x - x_p(t + \Delta t)]dx \qquad (3.2)$$

This is called single-pulsed, double-frame recording. These two images contain random patterns of particles that can be used to identify the particles uniquely.

Correlation methods can yield instantaneous velocity vector fields if one estimates the cross-correlation between I_1 and I_2 on the basis of spatial averages instead of ensemble averages or time averages. The cross-correlation estimator for a spot labeled W_1 is given by,

$$R(s) = \int_{W_1} I_1(X)I_2(X + s)dX \qquad (3.3)$$

This function has a sharp maximum in the s-plane, located at the displacement between the recorded images, as shown in Fig. 3.10. The maximum occurs when the second image is shifted with respect to the first by an amount $s = \Delta X_p$. Then the integrand contains large peaks at which the particle images overlap, and the integral of these peaks is corresponding large. The $R(s)$ determines the image displacement and, ultimately, the particle displacement.
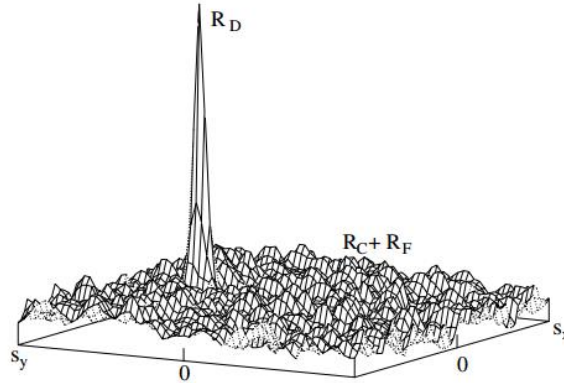
Figure 3.10: Correlations of single-pulsed, double-frame images (Raffel et al. (2018)).

During its elaboration, a lot of particles will lose out of the boundaries of inter-rogation areas (so-called drop-out), and to highly avoid this effect, an overlapping distance is recommended between contiguous interrogation areas. Besides, an inter-esting option called adaptive correlation has been used to generate more accurate instant velocity fields without the disadvantages of using smaller interrogation areas that lead to a higher drop-out. This mode analyses initially the bitmap using bigger interrogation areas to determine an approximate field. Later, an iteration with smaller interrogation areas allows the identification of smaller structures such as secondary flows and vorticities.

3.2.2 Data Processing

The PIV data process in the present study consists of three parts.

1) Pre-processing, which is an image treatment for enhancing the quality of the results.

2) PIV analysis. A PIV spatial autocorrelation algorithm developed at the von Karman Institute (Window Distortion Iterative Multigrid (WIDIM)) (Scarano (2000)) was applied to the pair of images in order to track the tracer particles and create the velocity maps;

3) Post-processing. The velocity fields which contain valuable information about the flow at the 90-degree plane was analyzed to understand the flow structures in the turning duct better.
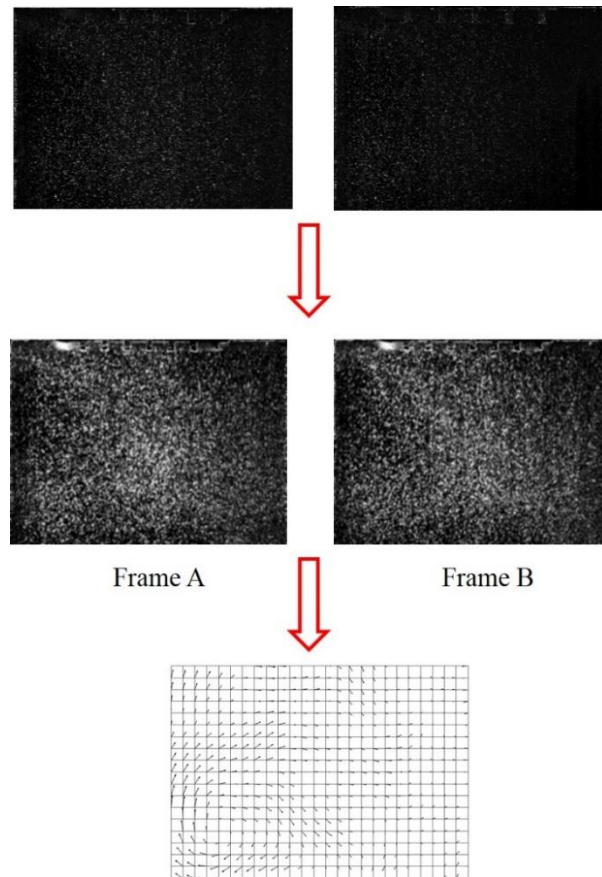
Figure 3.11: Raw pictures recorded by a high frame rate camera (top) and enhanced pictures (middle) and the final resulting contour plot with velocity vector (bottom).

Figure 3.11 presents the chart flow showing the data processing in a simplified way. Before calculating the velocity vector, the raw images need to be pre-processed to reduce the light reflections and homogenize the illumination. The enhanced pictures are shown in the middle of Fig.3.11, more clear and homogeneous illumination can be seen. A pair of frames always contains a large number of particles, it is impossible to trace and calculate each particle. Thus, the pictures are divided into many

sub-areas, as shown in the bottom of Fig. 3.11. As discussed previously, each inter-rogation area will be individually considered to build one velocity vector by cross-correlation method. Typically, an interrogation area dimension ranges from 16x16 to 128x128 pixels due to different algorithms. In this thesis, a 32x32 pixels interro-gation area dimension is used.

The cross-correlation between two corresponding interrogation areas is calcu-lated by using Fast Fourier Transforms (FFT) to obtain the particles mean displace-ment. A peak value is usually observed during the cross-correlation computation, which represents the best estimation for particles displacement. Figure 3.12 shows the mean cross-correlation map. The correlation functions exhibit a clear displace-ment peak. This allows obtaining a confident estimate of the velocity.
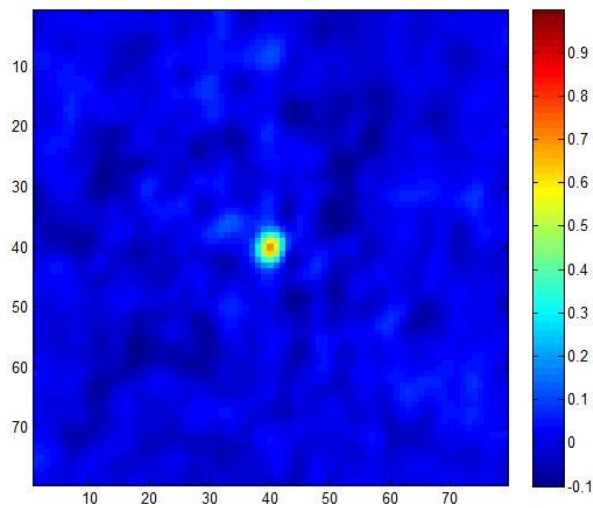
Figure 3.12: Mean cross-correlation map.

3.2.3 PIV Experimental System Setup

A closed re-circulating low-speed T2 wind tunnel at City is employed in this experiment. In all of the test cases, the free stream velocity is set to $V_\infty = 20$ m/s. A transparent test section is designed for this PIV experiment. The geometry and di-mension of the test section are the same as the geometry used in CFD simulation.

Measurements of the velocity field at the exit of the turning duct are acquired using the Particle Image Velocimetry (PIV) technique, as illustrated in Fig. 3.13. A

typically TSI Nd:YAG laser with 532 nm wavelength illuminates the measurement plane and the flow is seeded using an oil droplet generator. Particle images are recorded using a high frame rate camera, the fitted lens has 50 mm fixed focal and an aperture of f5.6. The high-speed camera is perpendicularly positioned to the light sheet to capture the tracer particles.
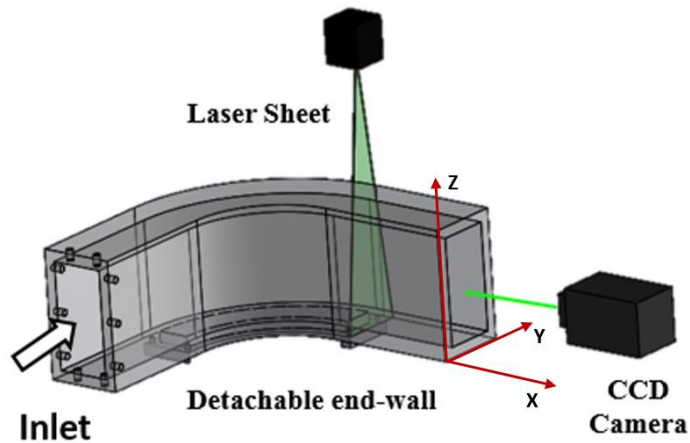
Figure 3.13: PIV experimental setup.

For each test, a total of 2000 image pairs are acquired with an image pair separation time of 15 µs at a rate of 1000 Hz, which is slow enough so that each measurement could be considered independent. Vectors are determined with TSI's Insight 4G software, using window sizes of 32×32 pixels. The instantaneous vector maps are subsequently post-processed in MATLAB to determine the mean vector maps.

3.3 Heat Transfer Experiment

3.3.1 Heat Transfer Coefficient and Adiabatic Wall Temperature

The transient thermal measurement technique was employed in the present experimental study. For a short running time, the solid can be considered as semi-infinite, one-dimensional conduction if the heat penetration depth is small compared with the actual thickness of the solid. A low-conductivity material was used in all

the experiments to validate this assumption.

Convection heat transfer coefficient (HTC, h) was determined experimentally using the definition from Newton's law of cooling (Bergman et al. (2016)):

$$q'' = h(T_{ad} - T_w) \ .$$
                                                                          (3.4)

where q'' is the surface heat flux (W/(m^2)), T_{ad} is the adiabatic wall temperature, and T_w is the wall temperature.

The assumption of this equation is that HTC is predominantly determined by the aerodynamics, hence the interaction between the solid and fluid part is negligible. It is acknowledged that when the temperature difference becomes very large, heat flux may not give linear independence of wall temperature, as reported by Maffulli and He (2014). However, within the temperature range of this thesis, the HTC can be considered independent of wall temperature.

The adiabatic wall temperature in Equation 3.4 is generally assumed to be the driving temperature on the solid surface to generate convective heat transfer. When the adiabatic wall temperature equals to the wall temperature, there will be no heat flux on the solid surface and the wall can be regarded as adiabatic. The use of adiabatic wall temperature allows HTC to be constant during the heat transfer process (independent of wall temperature). Detailed discussion on the use of adiabatic temperature can be found in Goldstein (1971), Moffat (2003) and Harrison and Bogard (2008).

The selection of adiabatic wall temperature is complicated when introducing pure air. It becomes a three temperature problem: mainstream temperature (T_∞), wall temperature (T_w) and cold purge air temperature (T_c). The adiabatic wall temperature should be a mixture between the mainstream temperature and the cold purge air temperature (Kwak et al. (2003)). This problem can be solved by using a transient heating method. If the inlet mainstream temperature and cold purge air temperature are constant during the transient process, the adiabatic wall temperature can be considered as a constant value.
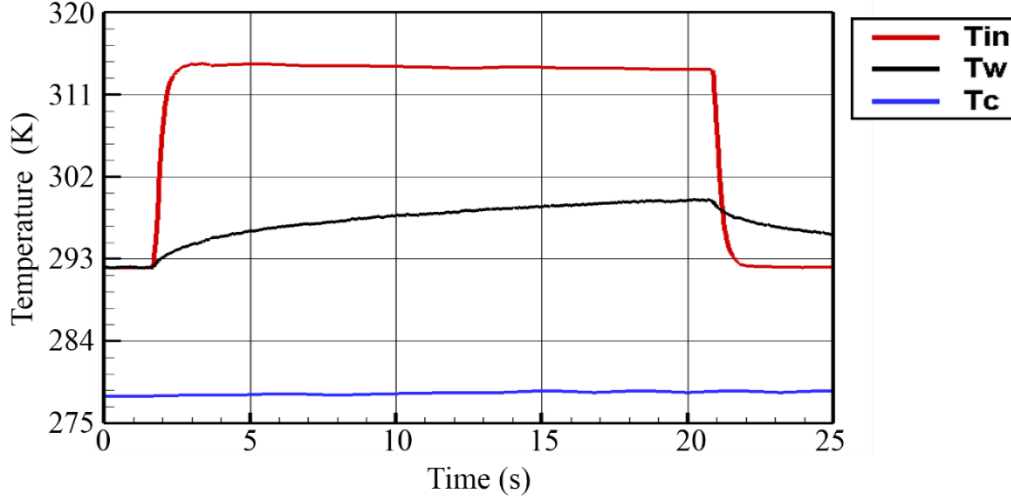
Figure 3.14: Time histories of the cold purge air, end-wall and inlet temperatures.

Figure 3.14 presents time histories of the cold purge air, duct end-wall and inlet temperatures during the heat transfer process. All the temperature data were acquired by a LabVIEW program. Low-speed wind tunnel and purge air system are running at the same time to reach the stable state which essentially guarantees the linear relationship between the surface heat flux and temperature difference. Then the mesh is powered and a step increase of 24 K is achieved in this test run. Transient thermal measurement technique relies on this step heating in the mainstream temperature (red color). The complete heat flux history is then reconstructed from temperature traces (black color) for each end-wall pixel by using the impulse method which will be discussed in detail in the next Subsection 3.3.2. The temperate of cold purge air temperature (blue color) is maintained at a relatively constant value during the transient experiment.

The heat transfer coefficient and adiabatic wall temperature can be easily derived through a linear regression process. Equation 3.4 is non-dimensionalized by dividing $T_{0,in}\kappa/r_i$ to account for the inlet temperature oscillations in the tests.

$$\frac{q''r_i}{T_{0,in}\kappa} = -\frac{hr_i}{\kappa} \cdot \frac{T_w}{T_{0,in}} + \frac{hr_i}{\kappa}\frac{T_{ad}}{T_{0,in}} \qquad (3.5)$$

Where κ is the air thermal conductivity under the room temperature (0.026

W/m-K) and r_i is the duct inner radius (0.09 m). For the linear cascade heat transfer experiment, r_i is replaced by blade axial chord C_x (0.056 m).

A sample of linear regression for one selected location on the imaged end-wall surface is shown in Fig 3.15. The slope of the regression line is the Nusselt number and is proportional to the heat transfer coefficient, and the adiabatic wall temperature can also be derived from the *x*-axis intercept of the regression line. Figure 3.15 shows that all data points scatter around the regression line with a good fit.
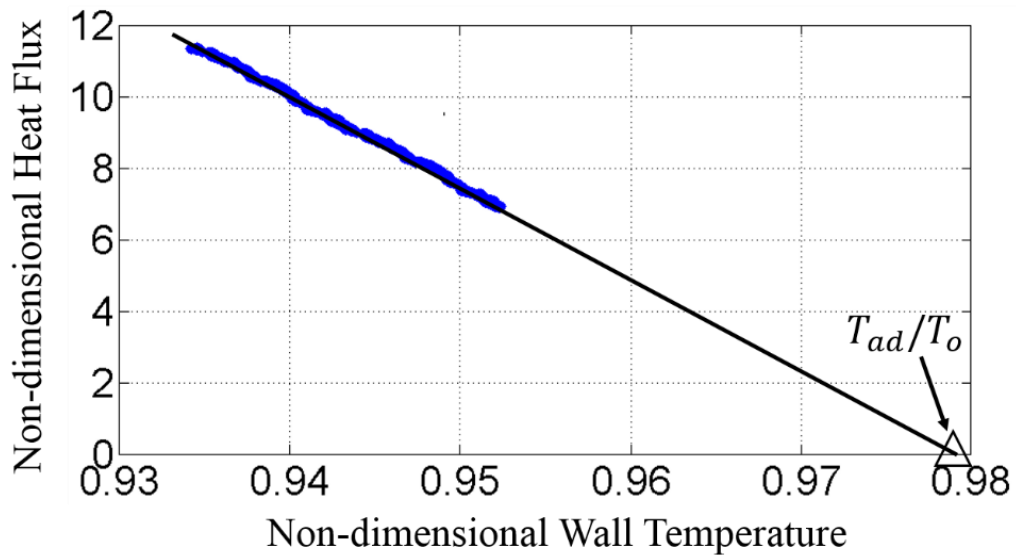
Figure 3.15: Non-dimensional wall heat flux versus wall temperature variations for one selected end-wall location.

3.3.2 Impulse Response Method

In this thesis, the impulse response method is used to reconstruct the surface heat flux from temperature history for each end-wall pixel location by IR thermography. The impulse response method is developed by Oldfield et al. (1978). A finite difference scheme was proposed to calculate heat flux from the discrete temperature data. Oldfield (2008) then proved the impulse response method is more accurate and faster than previous heat flux reconstruction approaches. This method has been adopted in a wide range of heat transfer research in turbomachinery (Zhang et al. (2010, 2011) and O'Dowd et al. (2009, 2013)).

The impulse method can be used for any Linear Time Invariant (LTI) system.

LTI means that the relationship between the input and the output of the system is linear and the output for a particular input does not change whenever that input is applied. The response of an LTI system such as heat transfer rate $q(t)$ can be calculated from the impulse response $h(t)$ of that system by the convolution integral.

$$q(t) = h(t) * T(t) = \int_{-\infty}^{\infty} h(\tau)T(t - \tau)d\tau \qquad (3.6)$$

To avoid the singularities and difficult evaluation of the integral, discrete-time domain is used. The continuous signals $T(t)$ and $q(t)$ are sampled at sampling period T_s or sampling frequency $f_s = 1/T_s$. The convolution integral can be written as

$$q[n] = h[n] * T[n] = \sum_{k=-\infty}^{\infty} h[k]T[n - k] = $$
$$\sum_{k=-\infty}^{\infty} h[n - k]T[k] \qquad (3.7)$$

In the processing, all signals and impulse responses are 0 for n<0 and all the signals have a finite size N. Thus, the convolution integral becomes

$$q[n] = h[n] * T[n] = \sum_{i=0}^{N} h[k]T[n - k] \quad , k=0,1,\ldots,N-1 \qquad (3.8)$$

The discrete impulse response function sequence $h[n]$ can be obtain from a pair of nonsingular analytical solutions $q_1(t)$ and $T_1(t)$ by the convolution of

$$q_1[n] = h[n] * T_1[n] \qquad (3.9)$$

For the semi-infinite solid, the heat conduction equation in Laplace transformed form is

$$\overline{T_1}(s) = \frac{1}{\sqrt{\rho_1 c_1 \kappa_1}} \frac{1}{\sqrt{s}} \overline{q_1}(s) \ . \qquad (3.10)$$

For a step in $q_1(t)$, $\overline{q_1}(s) = 1/s$, so

$$\overline{T_1}(s) = \frac{1}{\sqrt{\rho_1 c_1 \kappa_1}} s^{-3/2} \ . \qquad (3.11)$$

The inverse Laplace transform of Equation 3.10 is:

$$T_1(t) = \frac{2}{\sqrt{\rho_1 c_1 \kappa_1}} \sqrt{\frac{t}{\pi}} \ . \qquad (3.12)$$

Thus, the discrete impulse response $h[n]$ is obtained by substituting $q_1(t)$ and $T_1(t)$ into Equation 3.10. Therefore, for any sampled temperature data, the corresponding heat transfer rate can be determined by Equation 3.9. The numerical error for the impulse response method is smaller than 6×10^{-14}.

3.3.3 Calibration of Infrared Camera

When measuring an object, the IR camera receives radiation not only from the object itself but also from the surroundings reflected via the object surface. However, there is normally no easy way to find accurate values of emittance and atmospheric transmittance for the actual case. Although the IR camera has its own built-in calibration program, an in-situ calibration procedure similar to Schulz (2000) is conducted in the present study. A fast-response thermocouple is imbedded in the middle of the end-wall to record temperature variation. The end-wall is heated to 60K by using the heater gun. The thermocouple measures the decline of the end-wall temperature, while the IR camera records the relative grayscale value change during the natural cooling process. Figure 3.16 presents the grayscale of the IR camera and the calibration curve of temperature. The calibration relation is used in the experiment. Note that the same end-wall surface material is used in both 90-degree turning duct and linear cascade test section. Thus the infrared camera calibration shares the same in-situ calibration curve.
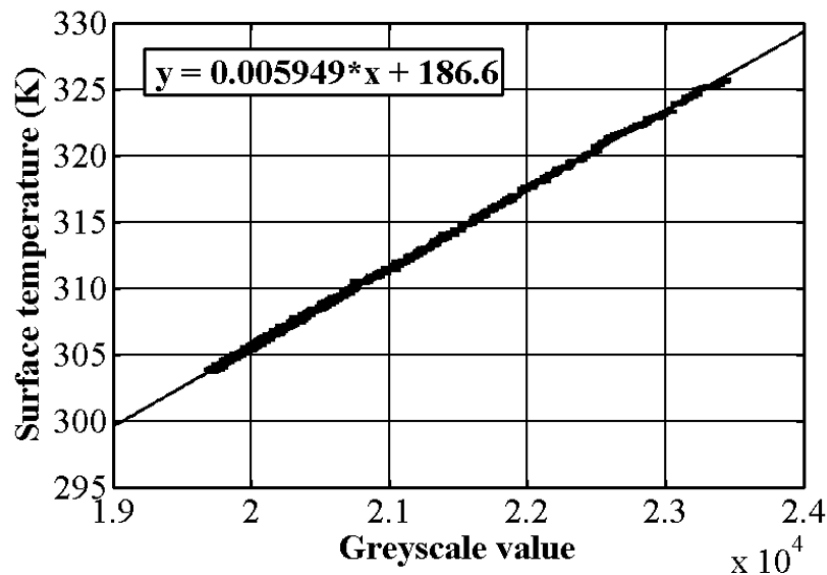
Figure 3.16: IR camera calibration curve.

3.3.4 Transient Thermal Measurement over Ribbed Surface

The semi-infinite 1-D conduction is a poor assumption near all the corners of

the ribs as lateral conduction (mostly 2D) effects dominate (O'Dowd et al. (2011) and Jiang et al. (2015)). In the present study, a case study on 2D transient conduction analysis was conducted to assess the errors for the near-rib region if the 1D conduction is still assumed to process the surface temperature trace. A detailed description of similar practice can be found in Jiang et al. (2015). Figure 3.17 shows the temperature contour within the solid three seconds after the ribbed wall is suddenly exposed to convection with a typical constant heat transfer coefficient value and fluid driving temperature (70 w/m^{2}K and 345 K, respectively, in the present experiments). The Impulse Response method is employed next to calculate the heat flux history based on the semi-infinite 1D assumption and the complete temperature trace during the transient heating history. The percentage differences between the calculated values and the specified heat transfer coefficient (true value) are shown in Fig. 3.17. The 1D conduction assumption is proved to be reasonable for locations in the central region of the rib groove, which covers about 60% of the ribbed surface area. As expected, the solution shows an overestimated heat transfer coefficient with an error over 10 percent near the corner. The semi-infinite assumption is absolutely not valid for rib top surface (over 110% error). Therefore, data showed on the rib top surface and groove corner regions can only be cautiously examined for the qualitative trend.
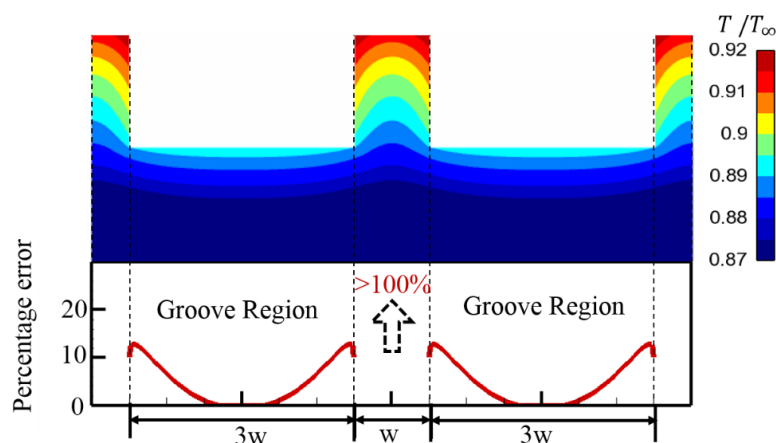
Figure 3.17: Measurement errors due to 1D semi-infinite conduction assumption, assessed through a 2D transient conduction analysis.

3.3.5   Transient Thermal Measurement Setup

The heat transfer experiment facility is shown in Fig. 3.18 and Fig 3.19. The transient Infrared thermal measurement was conducted on the end-wall surface. For the heat transfer experiment in 90-degree turning duct, a zinc selenide window is fitted into the duct top wall, and an infrared (IR) camera is installed perpendicularly with respect to the IR window. The distance from IR camera to the window is adjusted to ensure the field of view covers an angular region between 45° to 90°, namely the latter half of the turning duct, as shown in Fig. 3.2. For the linear cascade experiment, the zinc selenide window is flush mounted into the cascade top wall, so that the entire middle passage is within the field of view of the infrared camera. The location of the IR window is shown in Fig.3.4.
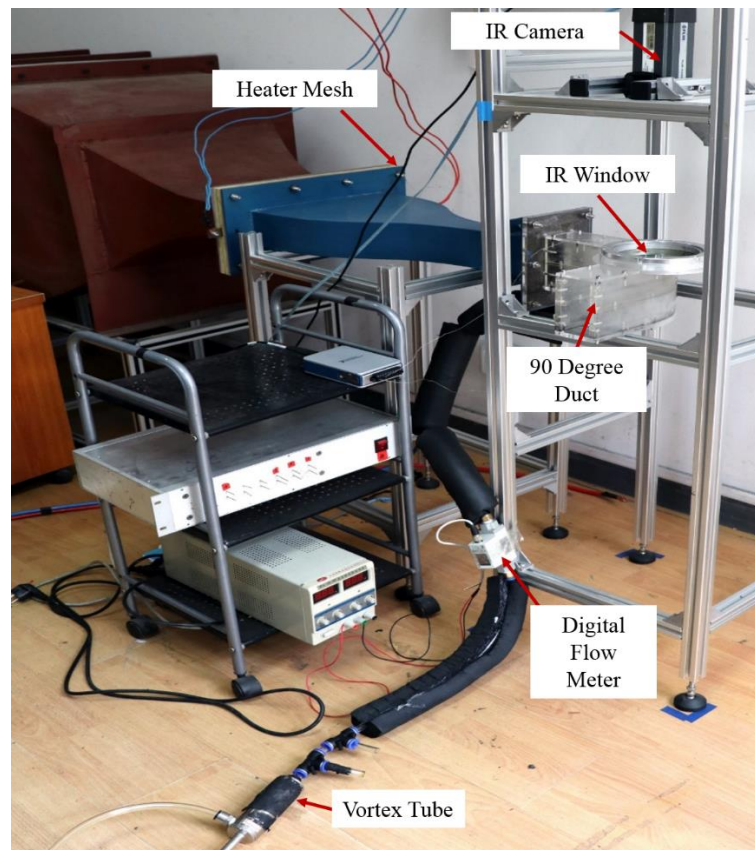
Figure 3.18: Transient thermal measurement facility for 90-degree turning duct.

FLIR A325 IR camera is employed in the thermal measurement. It can supply

16-bit grayscale images with the resolution of 320×240 pixels. The temperature range of the IR camera is from -20℃ to 120℃. Thus, the temperature to grayscale resolution is 0.002℃ per grayscale value. The IR camera is equipped with a lens of 18 mm focal length. The frequency of the IR camera is 60 Hz.

A heater mesh is installed upstream of the test section to provide a step increase in mainstream flow temperature. The heating mesh is made of stainless steel with a sieve mesh number of 200. During the experiment, the mesh is powered by a 100 kW DC power and raises the mainstream temperature. The mainstream temperature of duct and cascade test-section is about 314K and 345K respectively.

Two fast-response thermocouples are placed in the inlet section and purge cavity respectively to monitor the temperatures. The thermocouple has a wire diameter of 76 µm and response time of less than 80 ms. The temperature is recorded by a National Instrument data acquisition system.
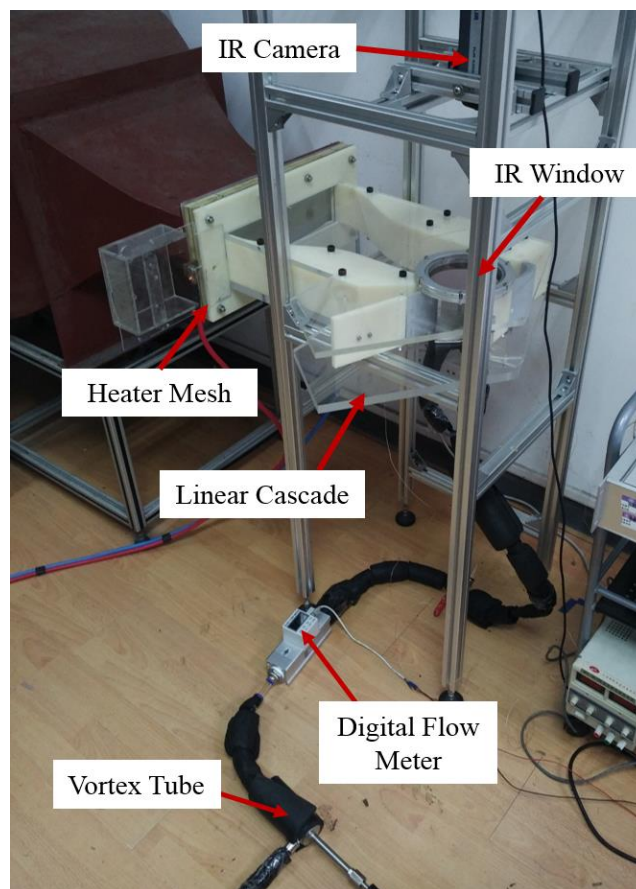
Figure 3.19: Transient thermal measurement facility for linear cascade.

3.4   Data Acquisition (DAQ) Systems

Two independent data acquisition chains were used in the heat transfer experiments. Both data acquisition systems are controlled by a PC, thus the pressure data, the operational conditions, and the end-wall surface temperature can be monitored at the same time. The schematic of the data acquisition system is shown in Fig. 3.20.

Two-port differential pressure transducers of the Sensortechnics HCLA Series are used in the experiments. The range varies from 0 to 2.5 mbar, which is sufficient for the inlet total pressure and the inlet boundary layer measurement. The transducers are calibrated individually and recalibrated every time when measurements are taken. The calibration curve is linear, and its slope is constant. These transducers ensure a precise measurement with only a little noise. The transducers are installed on a circuit board and then connected through National Instruments myDAQ to the computer, where the voltage is converted into pressure.
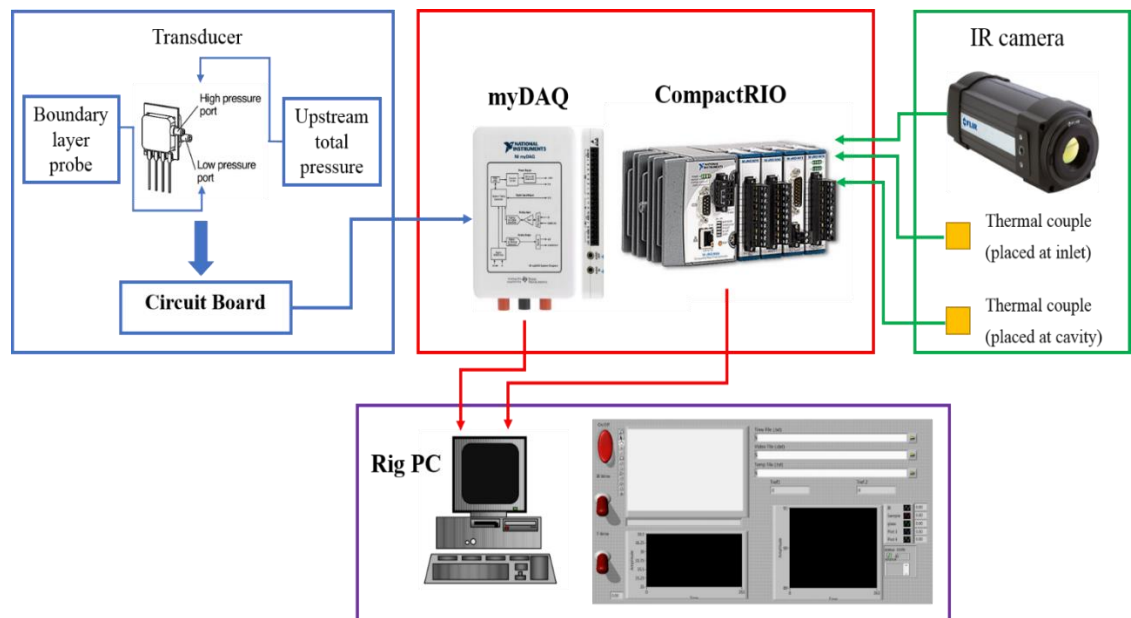
Figure 3.20: Schematic of the data acquisition system.

The infrared (IR) camera captures the end-wall surface temperature history through an IR window and transmits the recordings to the computer by an Ethernet connection cable (RJ-45 Gigabit). Two thermocouples are placed at the test section

inlet and stabilizing cavity respectively. The thermocouple signals are transmitted to the CompactRIO (NI 9219), which has in-circuit cold junction compensation for accurate measurement of the thermoelectric effect.

LabVIEW program is used on the computer to process the received data by communicating with the NI CompactRIO and myDAQ. It can easily monitor and record the pressure and temperature data. The program panel is also shown in Fig. 3.20.

3.5 Flow Condition

As shown in Fig 3.4, there are seven pressure taps located one axial chord upstream of the leading edge. The inlet static pressure and total pressure are measured by using a pitot probe placed at the middle hole.

At the inlet of the test section, a boundary layer trip is employed to enhance the secondary flow. The inlet boundary layer thickness is measured by a boundary layer probe through each hole. The single-hole probe has a flat tip to minimize potential errors in total pressure measurement. The sensing head diameter of the probe is 0.3mm. Detailed geometry of the boundary layer probe is shown in Figure 3.21.
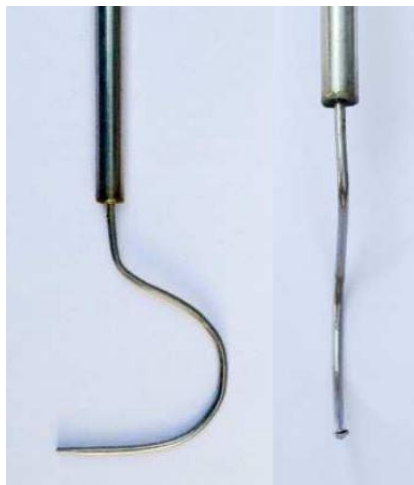
Figure 3.21: The boundary layer probe.

The inlet velocity distribution including boundary layer region is shown in Fig. 3.22. Note that due to the probe wall interaction no data is measured within 1mm height to the end-wall. It can be seen that the overall uniformity of the velocity distribution is satisfactory. The same velocity profile is also used as the inlet boundary

condition for the numerical prediction.
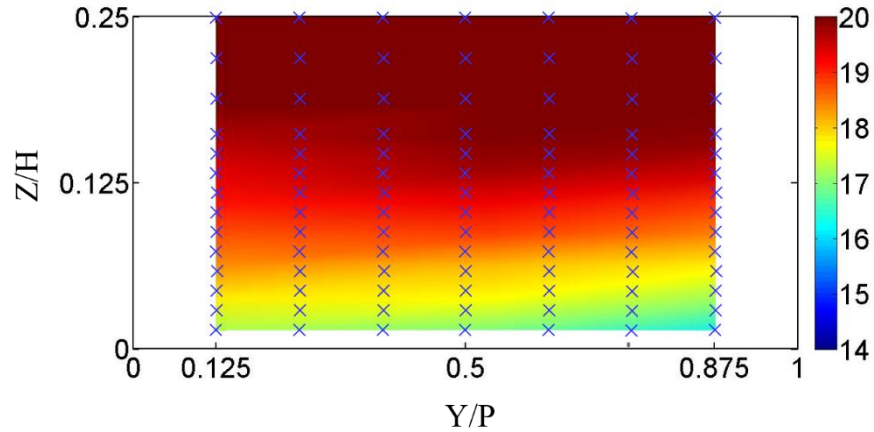
Figure 3.22: Inlet end-wall boundary layer velocity distribution measured one axial chord upstream of the test blade.

Details of flow conditions are listed in Table 3.4. The inlet mainstream velocity is 20 m/s, the mainstream accelerates through the cascade and exits at 50 m/s.

Table 3.4: Flow conditions of the transonic wind tunnel

Inlet velocity	20m/s
Inlet total pressure	102746 Pa
Inlet static pressure	102539 Pa
Inlet Reynolds number (based on C_x)	7.44×10^4
Exit velocity	50 m/s
Exit static pressure	101325 Pa
Exit Reynolds number (based on C_x)	1.86×10^5
Mass flow rate (full passage)	0.83 kg/s
Inlet boundary layer thickness, δ	6 mm
Inlet momentum thickness, θ	0.6 mm

3.6 Uncertainty Analysis

3.6.1 Linear Regression Uncertainty

Heat transfer coefficient and adiabatic wall temperature for a single experiment are obtained from linear regression, as explained in Section 3.3. Hence, the performance of linear regression dictates the uncertainty of heat transfer coefficient and adiabatic wall temperature in one experiment.

In order to assess the quality of linear regression during the transient data processing, R^2 is calculated. Linear regression can determine a best-fit line from a data scatterplot, thus the sum of squared residuals is reduced; equivalently, it reduces the error variance. For a set of n points (x_i, y_i) on a scatterplot and the best-fit line $\hat{y}_i = a + bx_i$. The coefficient of determination R^2 is defined by Devore (2015) as,

$$R^2 = 1 - \frac{SSE}{SST} \tag{3.13}$$

where SSE is the sum of square error, which can be interpreted as a measure of how much variation in y is left unexplained by the model, and is given by

$$SSE = \sum_{i=1}^{n} (y_i - \hat{y}_i)^2 \tag{3.14}$$

SST is the total corrected sum of squares, it is the sum of squared deviations about the sample mean of the observed y values, which is defined as

$$SST = \sum_{i=1}^{n} (y_i - \bar{y})^2 \tag{3.15}$$

R^2 is a measure of the proportion of variability explained by the fitted model. The distribution of R^2 in the measurement area for the smooth duct end-wall case is shown in Fig. 3.23a. R^2 is above 0.9 in most of the measurement domain, suggesting a satisfactory performance in linear regression. The distribution of R^2 in Fig. 3.23b reveals that the values are higher than 0.9 over the measurement domain and close to one at far downstream location, while the slightly lower R^2 value is present near the purge air inlet region. Figure 3.23 indicates that the fitted model predicts the data variation trend very well.

(a)   (b)
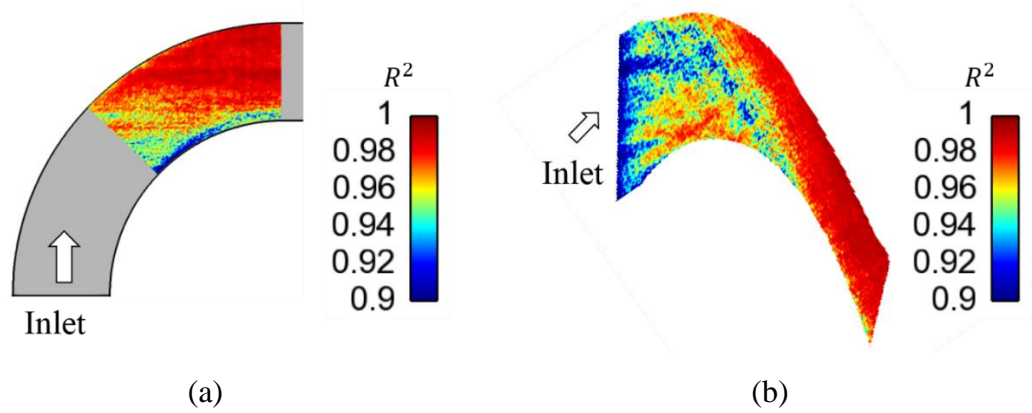
Figure 3.23: Contour of R^2 in linear regression for (a) 90-degree turning duct and (b) linear cascade heat transfer experiment.

3.6.2 Overall Uncertainty

To further examine the consistency of the obtained results, four repeated transient tests were taken for each type of end-wall surface. The 95% confidence level was used to estimate the uncertainty in the transient thermal measurement. The absolute uncertainty is then defined as

$$P_r = \frac{tS_x}{\sqrt{N}} \tag{3.16}$$

where N is the number of individual measurements. The value of t is given by the t distribution with N−1 degrees of freedom, for $N < 31$, t = 2. S_x is the standard deviation for the data ensemble, which is given by

$$S_x = \left[\frac{\sum_{i=1}^{N}(X_i - \bar{X})^2}{N - 1} \right]^{\frac{1}{2}} \tag{3.17}$$

where $\bar{X}$ is the arithmetic mean value of the ensemble. The relative uncertainty (U%) can be calculated based on absolute uncertainty and the ensemble mean value.

Figure 3.24 shows the contour of relative uncertainty in adiabatic wall temperature for 90-degree turning duct and linear cascade heat transfer experiment. The relative uncertainty in T_{ad} is below 0.3% for most of the rear 45° of the duct end-wall surface. For the cascade case, it can be observed that the relative uncertainty in

T_{ad} is below 0.5% for the majority of the blade passage.

(a)   (b)
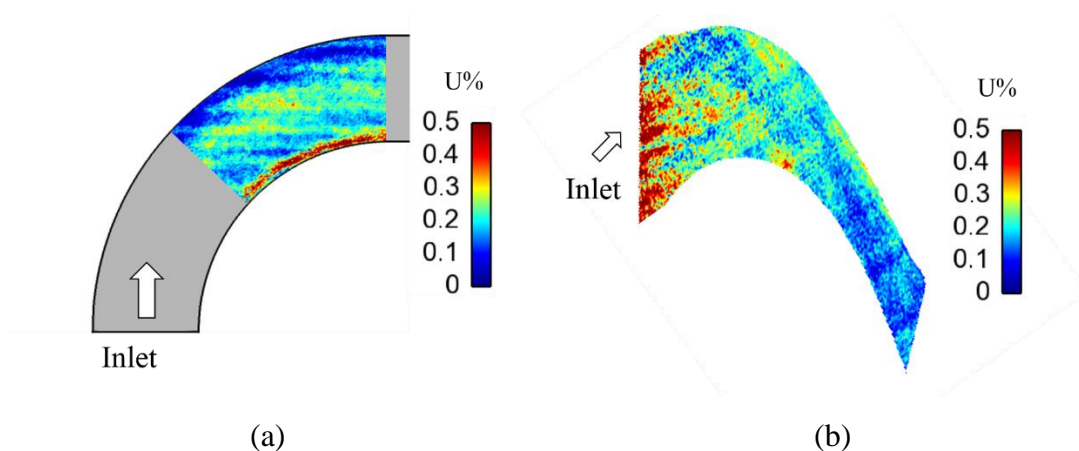
Figure 3.24: Relative uncertainty (U%) in T_{ad} distribution for (a) 90-degree turn-
ing duct and (b) linear cascade heat transfer experiment.

Figure 3.25 shows the contour of relative uncertainty in heat transfer coefficient
for 90-degree turning duct and linear cascade heat transfer experiment. The uncer-
tainty is also calculated based on Equation 3.19. It can be seen that the relative un-
certainty in HTC is below 10% for both cases.

(a)   (b)
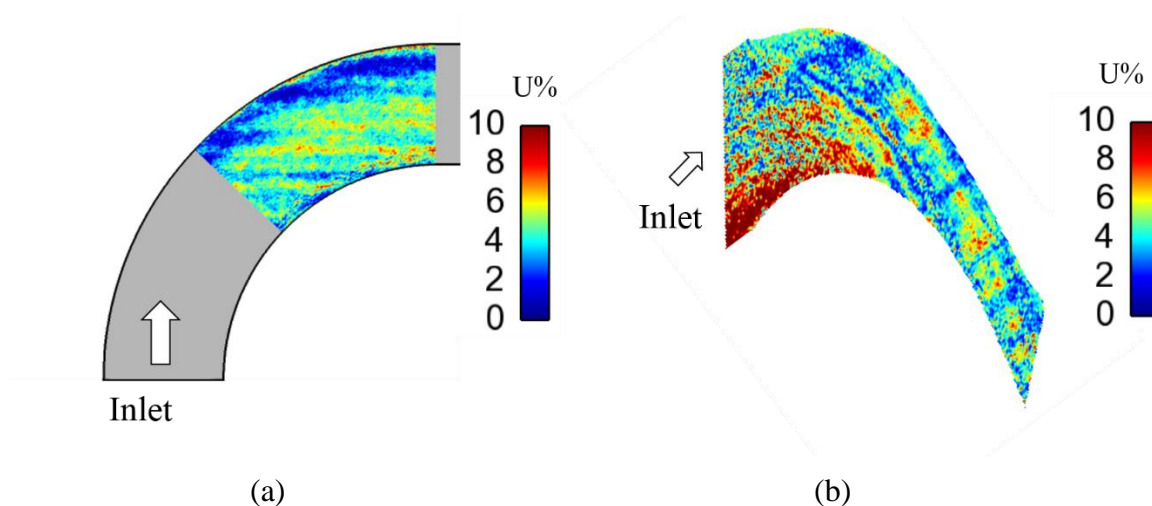
Figure 3.25: Relative uncertainty (U%) in HTC distribution for (a) 90-degree turn-
ing duct and (b) linear cascade heat transfer experiment.

Systematic uncertainty is also considered to evaluate the overall uncertainty. In
the present experimental study, the element systematic error sources mainly come

from the wall temperature measurement and end-wall material property measurement. The temperature to the grayscale resolution of the IR camera is 0.002 °C per grayscale value, thus the uncertainty of IR camera can be negligible. The systematic uncertainty only comes from the uncertainty of the K-type thermocouple (1K) in the calibration process. The material property (thermal product) uncertainty is 5%. A jitter analysis described by Moffat (1988) is used to determine the overall uncertainty.

The contribution of the uncertainty in material properties and thermal couple to the uncertainty in T_{ad} and HTC is calculated by

$$B_R = \sqrt{\sum_{i=1}^{N} \left(\frac{\partial R}{\partial X_i} B_i \right)^2} \qquad (3.18)$$

where R is the experiment result (T_{ad}, HTC) calculated based on several measurements. B_R is the systematic error. B_i is the bias limit for each variable. The overall uncertainty is then defined as

$$U_R = \sqrt{B_R^2 + P_R^2} \qquad (3.19)$$

A summary of uncertainty values for various measurement properties is presented in Table 3.5. The uncertainty values are within acceptable level compared to most heat transfer results in the open literature (Kwak et al. (2003); O'Dowd et al. (2013)).

Table 3.5: Measurement uncertainties

Measurement	Relative uncertainty 95% confidence
Material property	5% (564 ± 28 $W\sqrt{s}$/m²K)
Measured wall temperature	1K
HTC	9.7%
T_{ad}	0.3%

3.7   Summary

The PIV and transient heat transfer experimental facility and procedure are introduced in this chapter. Three experimental measurements are performed in the low-speed wind tunnel. The low-speed testing is focused on understanding the flow physics, lessons learned from the experiment can therefore be applied to the engine component design philosophy. A transparent 90-degree turning duct is first designed for both PIV and heat transfer experiment. Then the geometry of linear cascade test section which is used for transient thermal measurements is described in detail. The detachable end-wall surface structure is manufactured by using the 3D printing technique and is easy to change. The PIV measurement system and heat transfer experimental setup are presented in the followed section. Also included is an overview of end-wall rim seal geometry, purge air supply system, and hardware instrumentation. Two experimental measurement techniques employed in this thesis are introduced in this chapter. PIV is the non-intrusive method that does not influence the flow field. The principle of the PIV technique is described. The whole process that has been applied from the obtainment of raw images by the cameras to the creation of files containing valuable information about the flow is then explained. The second measurement techniques used in the heat transfer experiment is thermal measurement technique. The main assumption of this method is that the solid can be considered as semi-infinite, one-dimensional conduction and a step heating occurs at the origin. The infrared camera needs to be first calibrated before using it to record the end-wall surface temperature which minimizes the uncertainties associated with surface emissivity, transmissivity and radiation from surroundings. The principle of impulse response method is discussed in the followed section. End-wall surface heat flux can be reconstructed from temperature traces, the heat transfer coefficient and adiabatic wall temperature can be obtained from linear regression. Two main independent data acquisition chains for data recording and monitoring are described. The wind tunnel flow condition and inlet boundary layer information are listed in the followed section. Uncertainty analysis of the experiment is discussed at the end of this chapter. The linear regression uncertainty and repeatability analysis show that the experimental

results are reliable.

Chapter 4

Computational Approach and Details

The computational fluid dynamics (CFD) setups for all the numerical studies are described in this chapter. Section 4.1 introduces the computational domains, meshing strategies and boundary conditions. ANSYS FLUENT 14.5 is used to perform the numerical simulation. The introduction of solver, Reynolds-Averaged approach and turbulence model are presented in Section 4.2. Section 4.3 shows the results of grid impendence study. Finally, the simulation strategy is validated through the comparison with the experimental data.

4.1 Computational Domain and Mesh

The computational domain of 90-degree turning duct is shown in Fig. 4.1. The duct geometry is set the same as the experiment test section described in Subsection 3.1. The fluid flows from the left to the right side as shown in Fig. 4.1. The inlet boundary is set as the velocity inlet, while the outlet pressure equates to ambient pressure. The upper, lower and side boundaries of the domain are defined as the wall.

The construction of the computational domain and the meshing is done by a commercial software Pointwise. Fully structured hexahedra mesh is generated for different end-wall surface structures as can also be seen in Fig. 4.1. In order to ensure the accuracy of modeling small turbulent structures close to the rib and wavy groove region, the first cell node is set to achieve y+ close to 1.
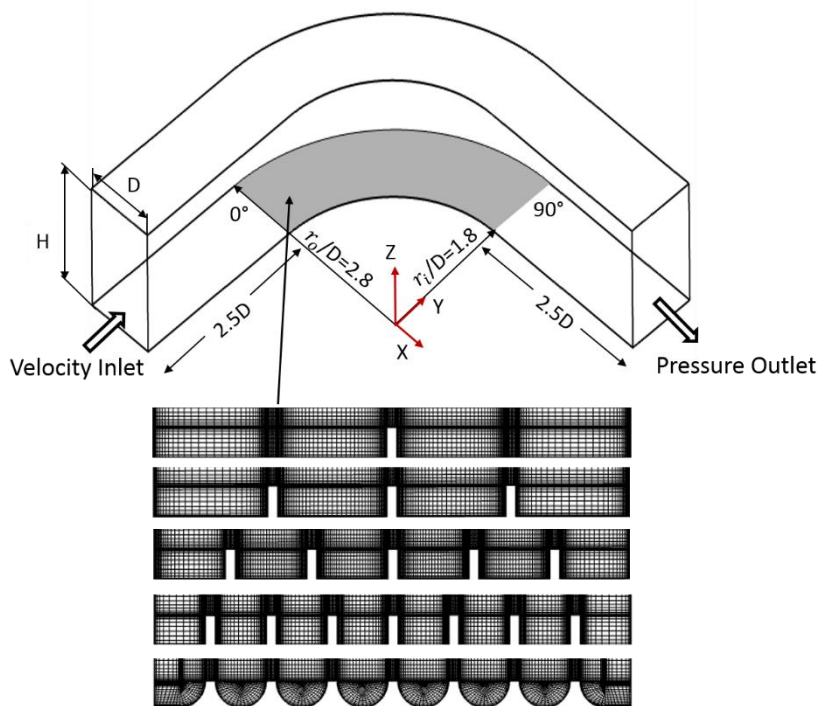
Figure 4.1: The 90-degree turning duct computational domain and the meshes around the end-wall structures.

Figure 4.2 shows the linear turbine cascade computational domain which consists of one blade with periodic boundary conditions. The flow field in the whole

linear cascade can be modeled with less computational cost. Inlet of the computational domain is one axial chord upstream of the blade's leading edge and set as velocity inlet. The outlet of the domain is 1.5 axial chords downstream of the blade trailing edge. Fully structured hexahedra mesh employed in this study is also shown in Fig. 4.2. The y+ value is smaller than one near the wall. It should be noticed that the same grid distribution was implemented for the smooth case to minimize the grid effect.
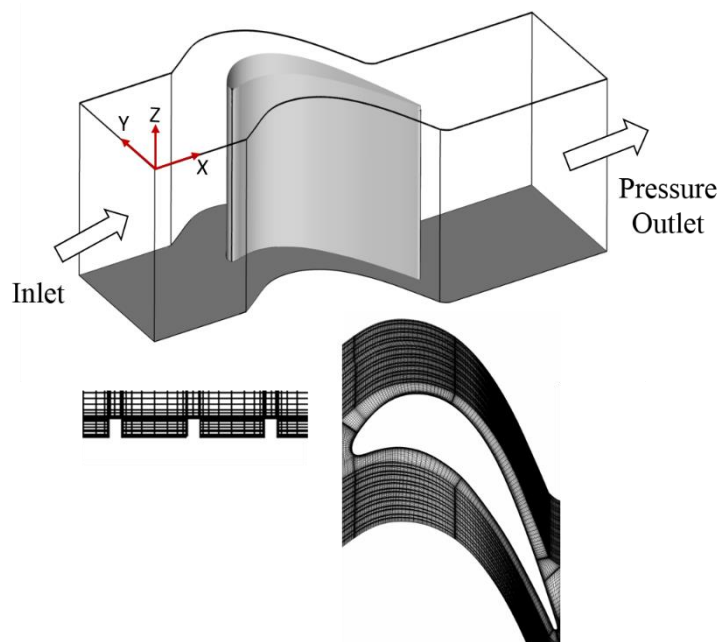
Figure 4.2: The linear cascade computational domain and the meshes around the end-wall structures.

Figure 4.3 shows the computational domain of 90-degree turning duct with purge air injection. The geometry and the duct inlet flow condition are set the same as the experiment. Pressure inlet is used as the inlet boundary condition for both the mainstream and the cooling air cavity inlet. Ambient pressure is set as the duct outlet boundary condition. Isothermal boundary conditions are set on the end-walls. The heat transfer coefficient and adiabatic wall temperature are calculated from two cases with different temperature values (290 K and 300 K).

Figure 4.3 presents an enlarged view of the hexahedra mesh around the purge air slot and wall ribs. The first grid point immediately above the wall has y+ value close to 1.
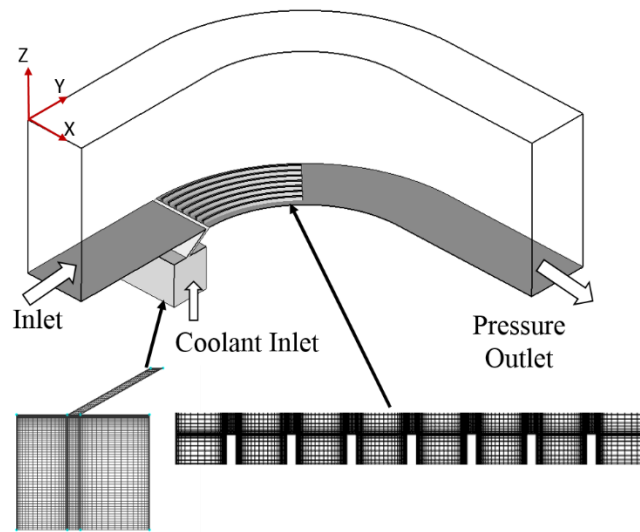
Figure 4.3: The 90-degree turning duct computational domain and the meshes in the purge cavity and slot and around the end-wall structures.

The computational domain of linear cascade with purge air injection is shown in Fig. 4.4, which includes one blade with periodic boundary conditions, rim seal and purge air cavity. The blade profile, flow angle and inlet boundary condition are the same as the experimental setup which introduced in Section 3.1 and 3.5. The temperatures at cascade inlet and purge air inlet are set as 345K and 293K, respectively, according to the thermocouple measurements. The duct outlet boundary condition is specified as ambient pressure.

Due to the complex geometry and periodicity requirement of the blade passage, structured grids are first created by sub-dividing the domain into several blocks. The block edges and faces are associated with the nearby curves and surfaces of the domain. Three grid sizes are studied to check the grid independence which will be given in Section 4.3. The grid of 5 million cells was chosen for further analysis, considering the heat flux value is not changed with larger grid density.
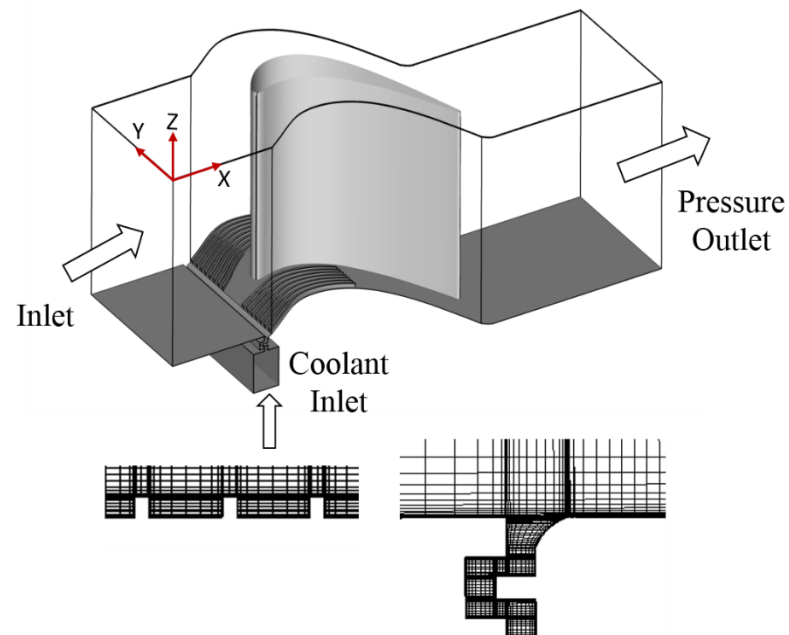
Figure 4.4: The linear cascade computational domain and the meshes in the purge cavity and slot and around the end-wall structures.
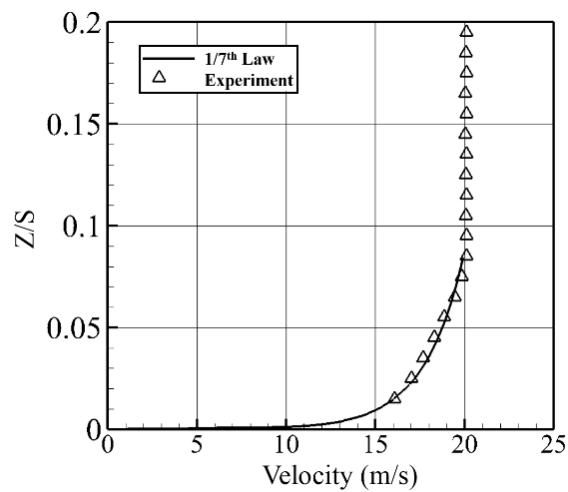
Figure 4.5: Inlet end-wall boundary layer velocity profile measured one C_x upstream of the test blade.

An example velocity profile in the boundary layer is shown in Fig. 4.5. In addition to experimental data, a boundary layer profile approximated by 1/7 power law is also illustrated in the same figure (Zhang et al. (2010)). Good agreement between

experimental data and 1/7 power law profile can be observed.

$$\frac{v}{V} = (\frac{z}{\delta})^{\frac{1}{7}}$$
(4.1)

Where δ is the measured inlet boundary layer thickness, V is the measured mainstream velocity, v is the velocity measured along Z direction. Then a User Defined Function (UDF) code is programmed to match the inlet velocity profile measured in the experiment. UDF is a routine written in C language which can be dynamically linked with the solver.

4.2   Solver

All numerical results presented in this thesis are obtained using the commercial software ANSYS FLUENT 14.5. The FLUENT solver is based on the finite volume method to solve the governing equations. The general conservation (transport) equation for mass, momentum, energy in the integral form is

$$\frac{\partial}{\partial t}\int_{\Omega} \Phi \, d\Omega + \int_{S} \Phi \boldsymbol{V} \cdot \boldsymbol{n} dS = \int_{S} \Gamma \nabla \Phi \cdot \boldsymbol{n} dS + \int_{\Omega} Q \, d\Omega$$
(4.2)

In this thesis, the simulation is carried out in the double-precision mode to improve the level of convergence. The fluid in the simulation is incompressible gas with constant physical properties due to the low speed condition. The solver type employed in this study is pressure-based.

Reynolds-Averaged Navier-Stokes (RANS) equation is employed to resolve the turbulent flow in this study. The basic idea behind the equations is Reynolds decomposition, whereby an instantaneous quantity is decomposed into the time-averaged and fluctuating quantities. RANS equation governs transport equation with averaged flow quantities and models the turbulence. Therefore, the RANS-based approach largely reduces the computational source and effort.

The k-ω shear stress transport (SST) turbulence model is chosen for all the numerical studies. Menter (2002) developed the k-ω SST model to make the k-ω model more accurate. In the near-wall region, the formulation of SST works from the inner part to the viscous sub-layer, while in the free stream region, the k-ω model is very sensitive to the turbulence properties, to avoid this problem, the formulation in this

region switches to a k-ε behavior. Therefore, the k-ω SST model can predict the flow condition near the engineered surface structure accurately and obtain precise numerical solutions (Nouri et al. (2013); Lei and Lixin (2015); Wang et al. (2016)).

Visualization of the CFD results is accomplished by using commercial software EnSight and Tecplot.

4.3 Grid Independence Study

Grid independence for 90-degree turning duct domain is checked through three grids with different density, namely 2 million, 5 million and 8 million nodes. Figure 4.6 compares the spanwise-averaged total loss coefficient C_p at the exit of turning passage (90-degree plane) in single rib case. It is apparent that the grids of 5 million and 8 million nodes produce the similar result, with a maximum difference less than 5%. As a result, the grid of 5 million nodes is chosen for simulation.
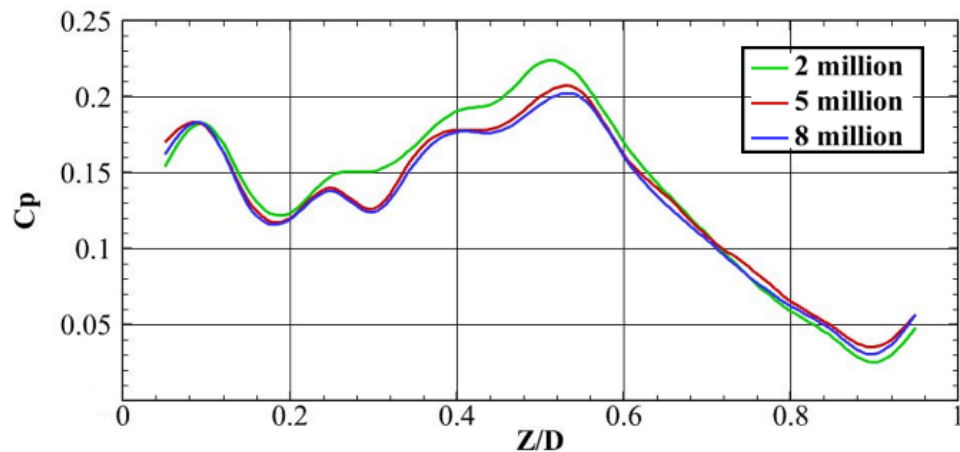
Figure 4.6: Spanwise distribution of the pitchwise averaged total pressure loss coefficient C_p.

Detailed mesh sensitivity study is also carried out for linear turbine cascade cases. The size of the mesh is set to 3 million, 5 million and 7 million respectively. Using the two points method, both Heat transfer coefficient (HTC) and adiabatic wall temperature (T_{ad}) can be easily obtained by solving a system of linear equation

(Equation 3.4). The averaged results of y^+ value, HTC and T_{ad} on end-wall surfaces are listed in Table 4.1.

The HTC difference distribution between the results from different meshes is shown in Fig. 4.7. It can be seen that the local HTC difference between 5 and 7 million cells is less than two percent for the majority of the end-wall surface. The area-average HTC difference between 5 and 7 million cells is 2.25%. Therefore, the difference between 5 and 7 million meshes can be negligible. In this thesis, the 5 million mesh was selected for the simulations.

Table 4.1: Mesh dependence studies.

Grid Size		3 million	5 million	7 million
Average y^+ on end-wall		1.066	0.665	0.511
Average HTC (W/(m²·K))	EXP	284.708		
	CFD	293.936	309.039	316.164
Average T_{ad} (K)	EXP	334.866		
	CFD	337.136	335.506	335.098
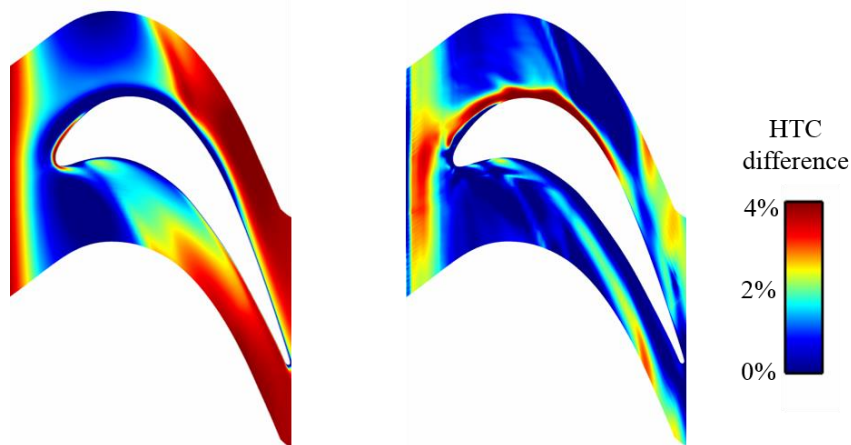
(a) 3 and 5 million   (b) 5 and 7 million

Figure 4.7: HTC difference distribution between the results from two meshes.

4.4   Code Validation

The simulation strategy employed in this research was validated by experimental data from various sources: (1) a previous experimental study by Camci and Rizzo (2002), for 90-degree turning duct with a single fence on the end-wall, (2) a previous experimental study by Wright et al. (2008b) in a linear cascade, and (3) thermal measurement for a simplified duct and a linear cascade.

In the experimental work by Camci and Rizzo (2002), the non-dimensional radius ratio of the duct is the same as the geometry shown in Fig 4.1. However, their duct has a square cross-section with H=D. Thus a separate validation case is set up to match the experimental setup.

The time-averaged velocity vector fields in the 90-degree plane are compared in Fig. 4.8. Similar results are predicted by the present simulation. Red and blue arrows illustrate clockwise and counter-rotating direction respectively. In the case without the fence installed, both simulation and experiment reveal the pair of symmetric secondary passage vortices centered at about Z/D=0.3 and 0.7, while in the case with a single fence, the lower passage vortex becomes lower to around Z/D=0.2 due to the counter-rotating vortex from the fence.

The coefficient of total pressure loss within the same plane is also compared in Fig. 4.9. The overall agreement can be observed. In the plane without single fence, the region with larger total pressure loss is associated with the passage vortex pair, and it features a symmetric mushroom-type due to the interaction of fluids between the top and bottom walls. Because of the presence of single fence and the resulted smaller vortex, the total pressure loss is alleviated in the lower half of the mushroom.
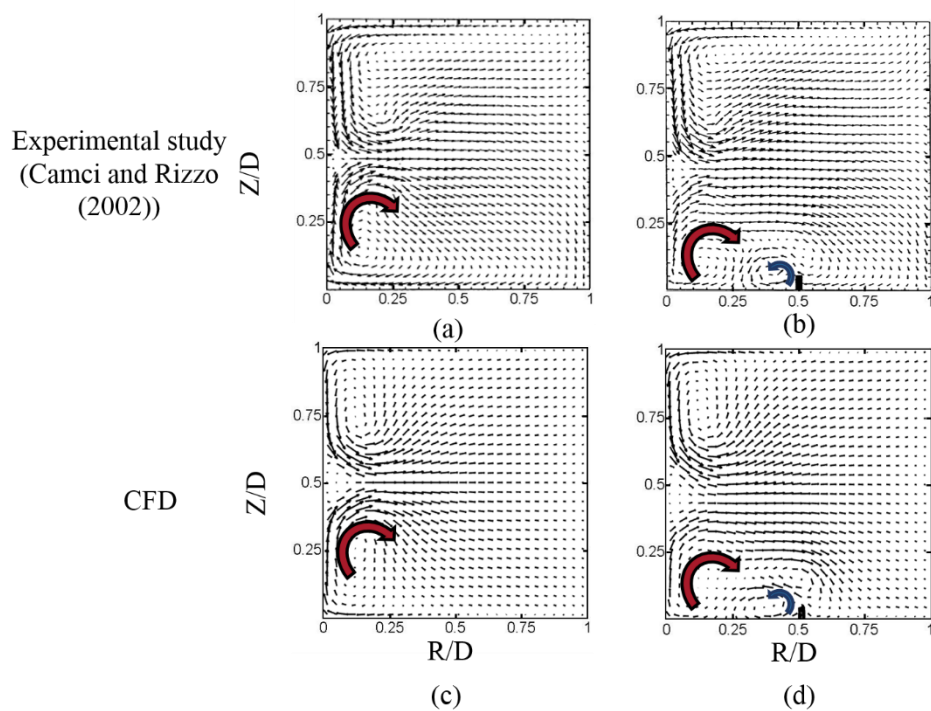
Figure 4.8: Time-averaged secondary vector field in the 90-degree plane, left column: no fence, right column: single fence.
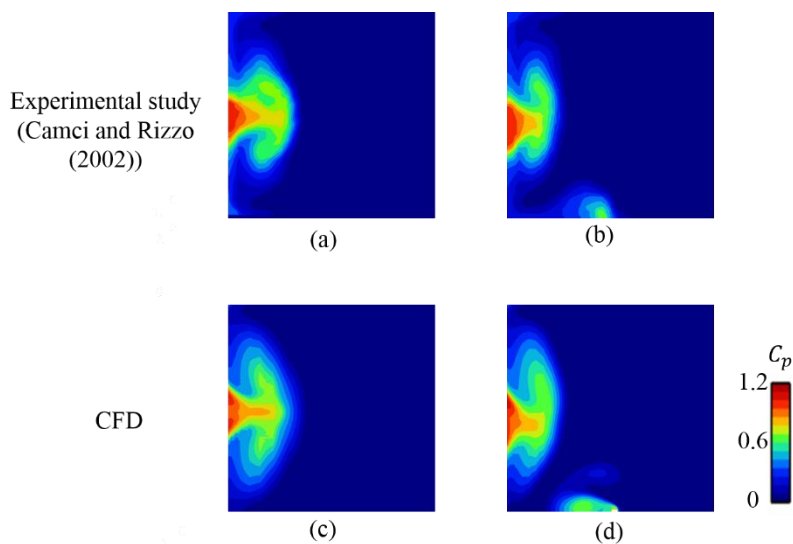
Figure 4.9: Total pressure loss coefficient C_p distributions for cases with and without single fence obtained at 90-degree plane of the duct.

Figure 4.10 shows the film cooling effectiveness distributions on end-wall. The experimental data is obtained from work by Wright et al. (2008b). Same experimental boundary conditions and turbine cascade dimension are employed in the CFD simulation. Both results indicate the purge air is quickly swept to the blade suction side after injection through the slot and cannot cover the entire passage. It can also be observed that the purge air is more diffuse in the experimental study compared with CFD result.

Experimental study (Wright et al. (2008b))   CFD
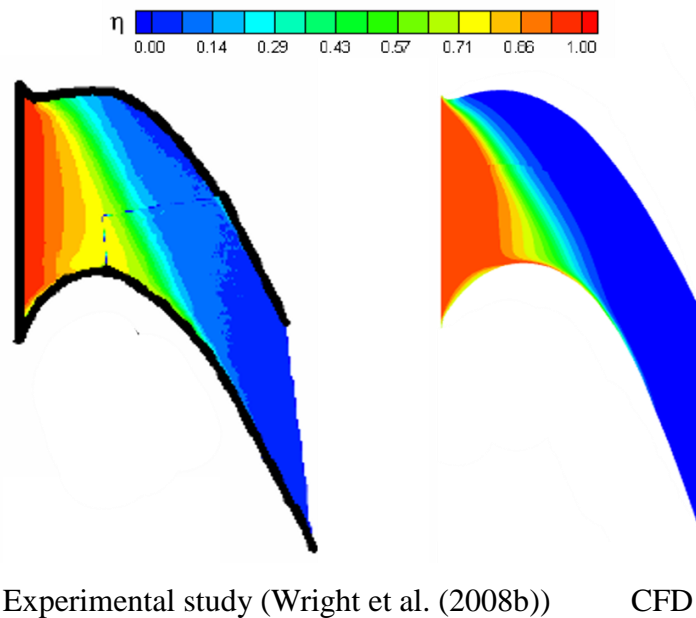
Figure 4.10: Film cooling effectiveness distributions on end-wall.

Figure 4.11 shows the heat transfer coefficient distributions on the end-wall obtained from experiments (EXP) and CFD for both smooth and ribbed surface. For experimental results, some stripes with high values of heat transfer coefficient can be observed near the end of the ribs, where the flow is dominant by small vortices developed earlier in the rib grooves. But there is a significant reduction of heat transfer coefficient for the majority of the after-rib region due to the relatively slower convection speed of the near wall coolant. The CFD simulation has a consistent agreement with the experimental data at the 45° to 90° region. For the smooth surface case, a low the heat transfer coefficient region from 20° to 45° can be observed.

This is related to the lift-off of the passage vortex from the end-wall. With the addition of ribs, the heat transfer coefficient is largely increased within the grooves due to small vortices.
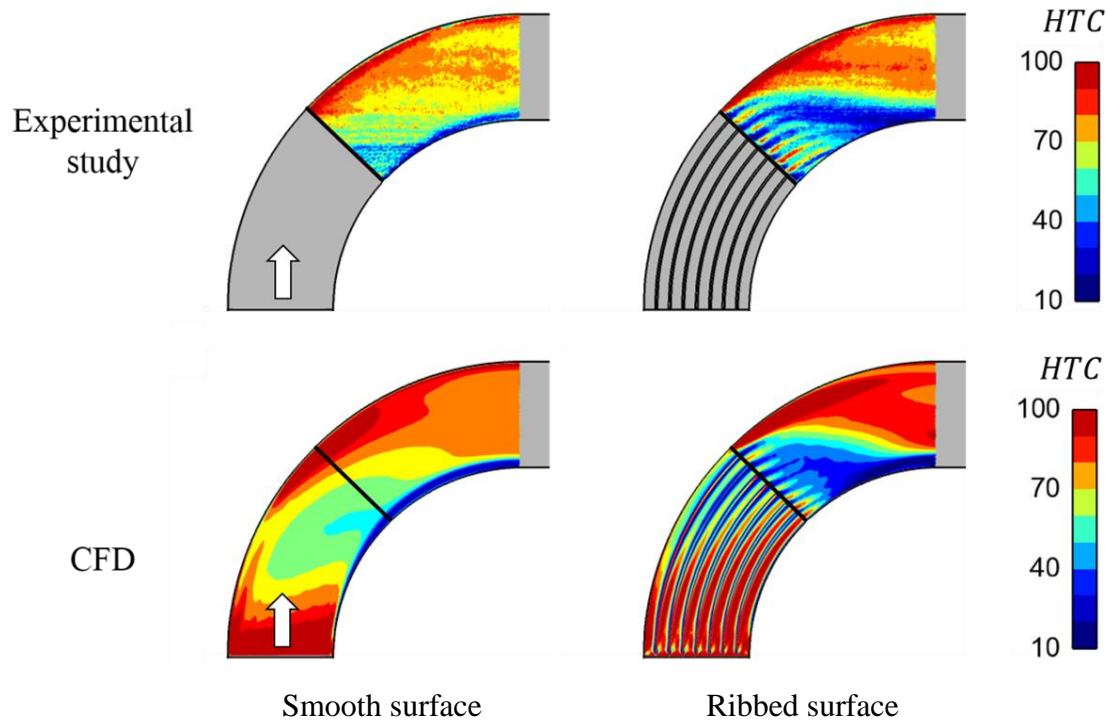
Figure 4.11: Distributions of heat transfer coefficient on the end-wall of 90-degree turning duct.

Figure 4.12 shows a quantitative comparison of the local film cooling effectiveness variation along the radial direction at the angular position of 50°. Solid lines and dash lines are used to represent the experimental data and CFD result, respectively. A significant increase of film cooling effectiveness can be observed at r/R>0.5 due to the guidance effect of ribs. The under prediction of coolant coverage near the outer wall region from CFD can also be consistently found for both smooth and ribbed walls.
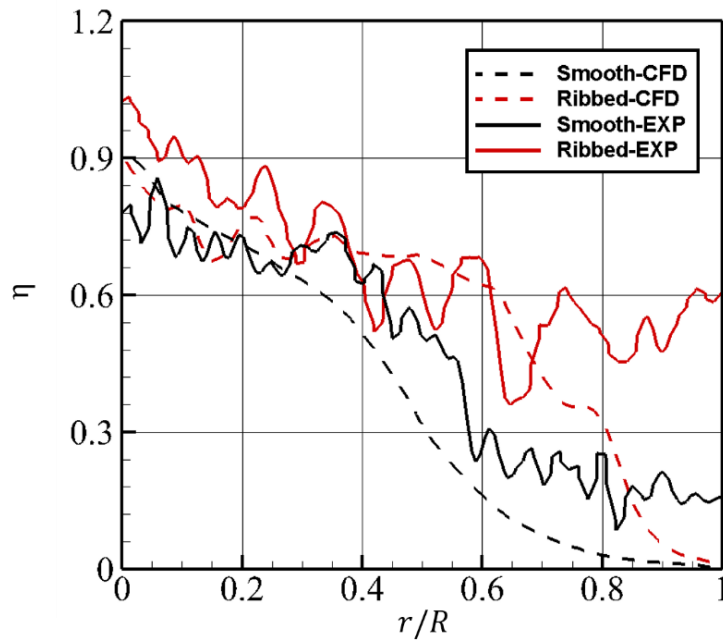
Figure 4.12: Film cooling effectiveness variation along the radius direction.

For turbine cascade cases, the distributions of heat transfer coefficient ratio h_f/h_0 from numerical prediction is used to validate against the experimental data. Where h_f is heat transfer coefficient measured with purge air flow, and h_0 represents heat transfer coefficient without purge air flow for smooth end-wall. Figure 4.13 shows the heat transfer coefficient ratio distributions for both smooth and ribbed surface case. It can be observed that CFD result shows good agreement with the experimental data. For the case without ribs, high heat transfer coefficient ratio occurs near the exit of the purge air rim seal slot. With the addition of ribs, the local heat transfer coefficient is increased in the rib region. Section 6.2 will compare the CFD and experimental results in detail.
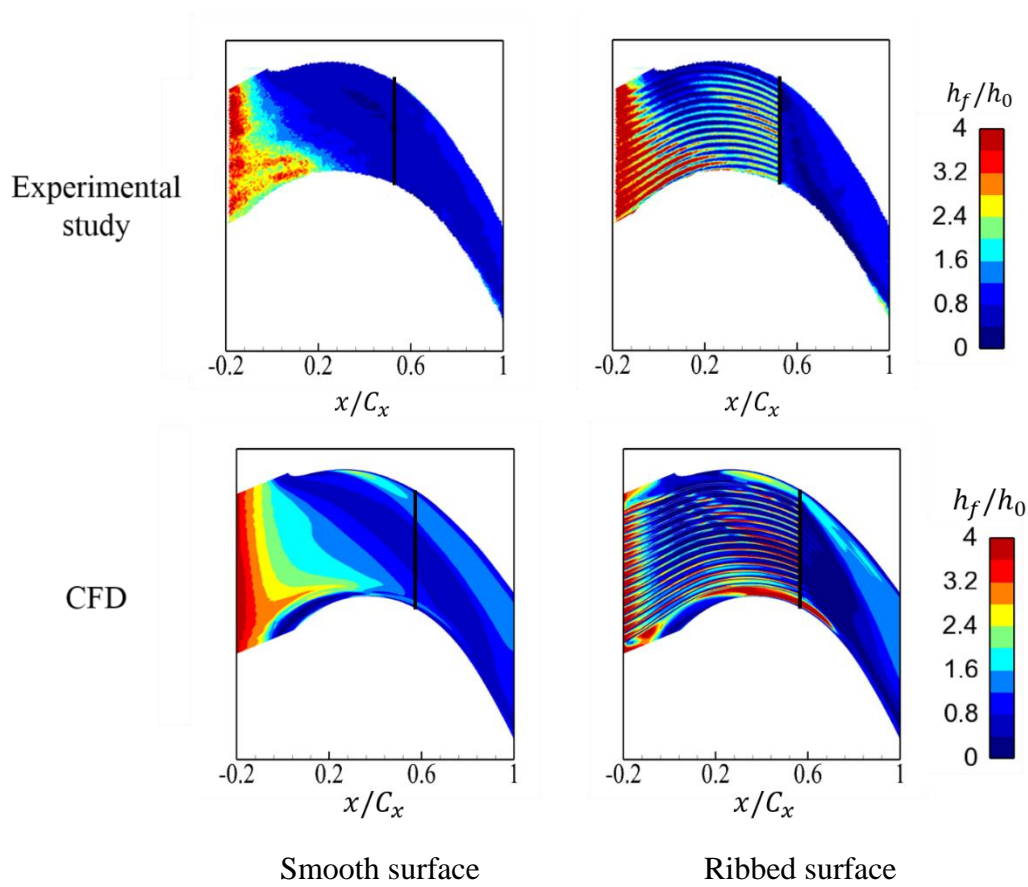
Figure 4.13: Distributions of film cooling effectiveness on the end-wall of turbine cascade.

As such, the present CFD methodology is suitable for studying the detailed secondary flow structure and end-wall heat transfer for both simplified duct and turbine cascade flow, with acceptable quantitative accuracy.

4.5   Summary

This chapter introduces the details of the computational fluid dynamics (CFD) simulations. The chapter begins with a summary of the computational domain and mesh. Four different domains are employed to study the secondary flow reduction

and purge air cooling enhancement. The domains are discretized with fully struc-
tured hexahedra mesh created by using the Pointwise software. The boundary con-
dition setting is also described in this section.

Steady Reynolds-Averaged Navier-Stokes (RANS) simulation is performed by
using ANSYS FLUENT software. The k-ω shear stress transport (SST) turbulence
model is selected to model the turbulence. The RANS equation and turbulence
model are briefly introduced in the followed section. Three grid sizes are studied to
check the grid independence for both of the 90-degree turning duct and the linear
cascade cases. The grid of 5 million cells is chosen for further analysis, considering
the total pressure loss coefficient and heat flux value is not changed with larger grid
density. Visualization of the CFD results is accomplished by using a commercial
software Ensight. Finally, the simulation strategy is validated through the compari-
son with the experimental data.

Chapter 5

Aerodynamic Performance

End-wall secondary flow control by using the engineered surface structure is investigated in this chapter. The secondary flow structure in a simplified duct is first shown in Section 5.1. The control mechanism of the engineered surface is then elaborated through the single rib case, after which the flow field resulted from multiple small ribs is discussed. The wavy groove result is also presented as a more practical case for the engineered surface. The novel concept is then applied to a linear turbine cascade in Section 5.2. Detailed flow structure is analyzed for cases with and without ribs.

5.1 Secondary Flow Control in 90-Degree Turning Duct

The fundamental flow physics and working principle of the engineered surface structure for a 90-degree turning duct are explored in this section. This simplified duct can simulate the turbine passage without introducing the horseshoe vortex. The concept is first explained through a single small rib installed on the duct end-wall. Detailed analysis of the flow produced by multiple ribs and grooves structure are then reported.

5.1.1 Secondary Flow Structure over a Smooth Wall

The generation of secondary flow, namely the passage vortex, in the 90-degree duct can be represented through the roll-up of the streamlines as shown in Fig. 5.1. Upon the lift motion of the streamlines, the passage vortex is formed and accumulated further downstream. The streamlines are released from the boundary layer and colored by dimensionless streamwise vorticity to illustrate the rotating direction.

The streamwise vorticity (Ω_s) is defined as

$$\Omega_s = \Omega_x cos\beta_{mid} + \Omega_y sin\beta_{mid} \tag{5.1}$$

where β_{mid} is the relative angle between streamwise direction and X axis in midspan. Ω_x and Ω_y is the vorticity component in X and Y direction respectively. In following results all the streamwise vorticity plotted are nondimensionalized by dividing by D/V_{in}. The negative vorticity magnitude indicates the clockwise direction from the inlet view and featured with red color, it is relevant to the passage vortex. While the positive vorticity (blue color) represents the vortex which rotates oppositely with the secondary flow vortex.

At the inlet, the vortex lines are normal to the mean flow thus the streamwise vorticity is zero. As the flow travels round the turning passage, the vortex lines begin stretching and have a non-uniform convection rate in the direction normal to the streamline. The streamwise vorticity component is then formed. The fluid is quickly

swept from the outer wall to inner wall. It can be clearly seen that a strongly clock-wise rotating passage vortex developed by the secondary motion established by the streamwise component of vorticity.
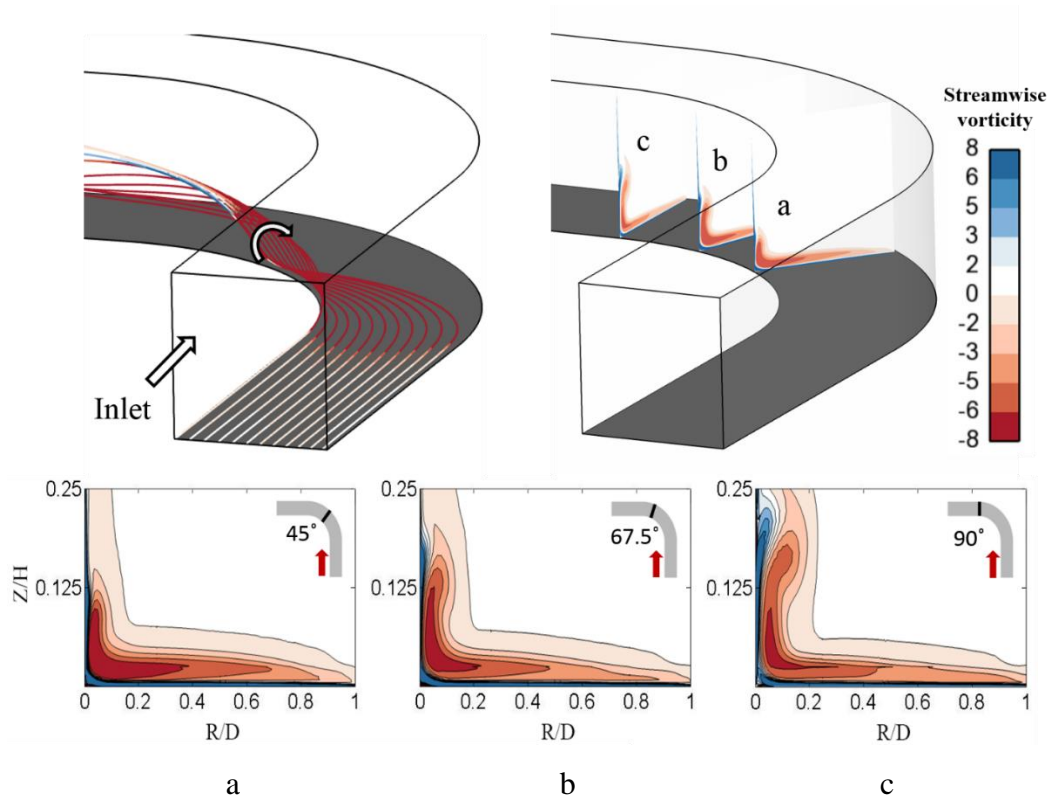
Figure 5.1: Secondary flow structure in the duct without rib and contours of streamwise vorticity in the cross flow planes (45-degree, 67.5-degree, 90-degree).

Dimensionless streamwise vorticity distributions in three cut-planes along the duct passage are further presented in Fig. 5.1. The three planes are located at 45, 67.5 and 90-degree respectively. As the fluid turning, the passage vortex develops and lifts up higher while the core of the negative streamwise vorticity reduces. This result is consistent with the mass-averaged negative streamwise vorticity alone turning passage, as shown in Fig. 5.2. Note that the negative sign only represents rotation direction, an absolute value is used in this graph. It is also clear that after 55-degree plane the mass-averaged negative streamwise vorticity decreases.
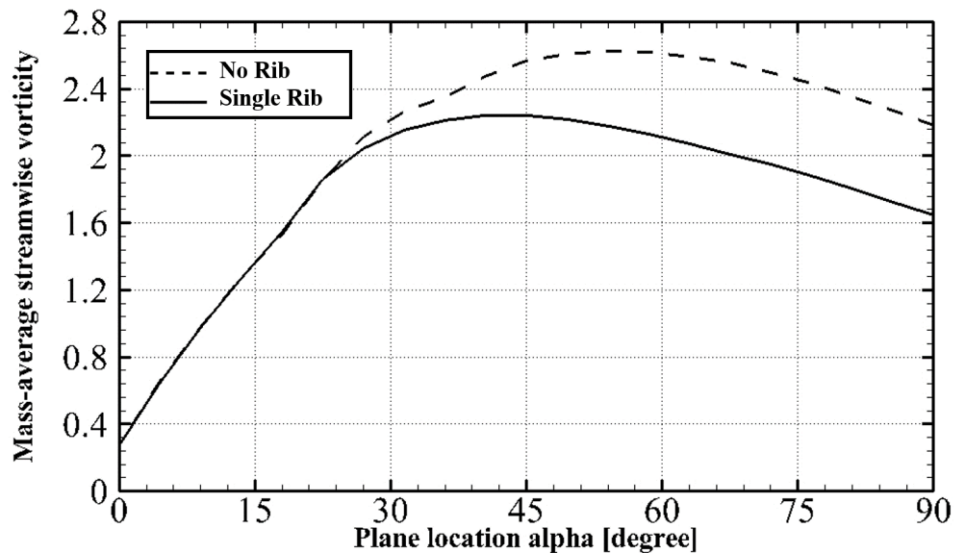
Figure 5.2: Mass-averaged negative Ω_s alone turning passage for cases with and without single rib.

5.1.2 Effect of Single Rib

Figure 5.3 presents a series of streamlines originated from the same location as those in Fig. 5.1 for comparison. The presence of the single rib blocks the inward motion of the outer streamlines. These blocked outer streamlines no longer contribute to the passage vortex and forms into a smaller "rib vortex" right past the rib with counter-rotating direction than the passage vortex. Due to the block-out mechanism, the overall strength of the passage vortex is reduced.

The evolution of the rib vortex and the passage vortex are also revealed in Fig. 5.3 through the streamwise vorticity contours. It can be seen that a rib vortex is produced with similar intensity (opposite sign) as the main passage vortex at an early stage in the 45-degree plane. The location of the rib vortex stays at the tip of the rib and does not enter the free stream. In comparison with the vorticity magnitude in the smooth duct, the passage vortex affected by the rib has a smaller size and reduced intensity in the planes shown in Fig. 5.3.

The weakening effect towards the passage vortex is further illustrated through the comparison of the mass-averaged negative streamwise vorticity for the cases with and without the rib, as shown in Fig. 5.2. The vorticity in the smooth duct has

a very steep growth rate till the plane at about 20 degrees, and a maximum intensity is achieved at the 50-degree plane, after which it is subject to decay. Different vorticity evolution is exhibited in the duct with a single rib. The initial steep growth seems to be not affected by the rib. Intensity discrepancy starts to grow after the 20-degree plane with maximum gap obtained at 50-degree plane. The weakened vorticity is caused by the single rib. As the rib vortex is fully established at the 50-degree plane, the reduction of streamwise vorticity is maintained further downstream. It can so far conclude that the sub-boundary layer rib structure is able to reduce the passage vortex intensity by shedding vortex with counter rotation.
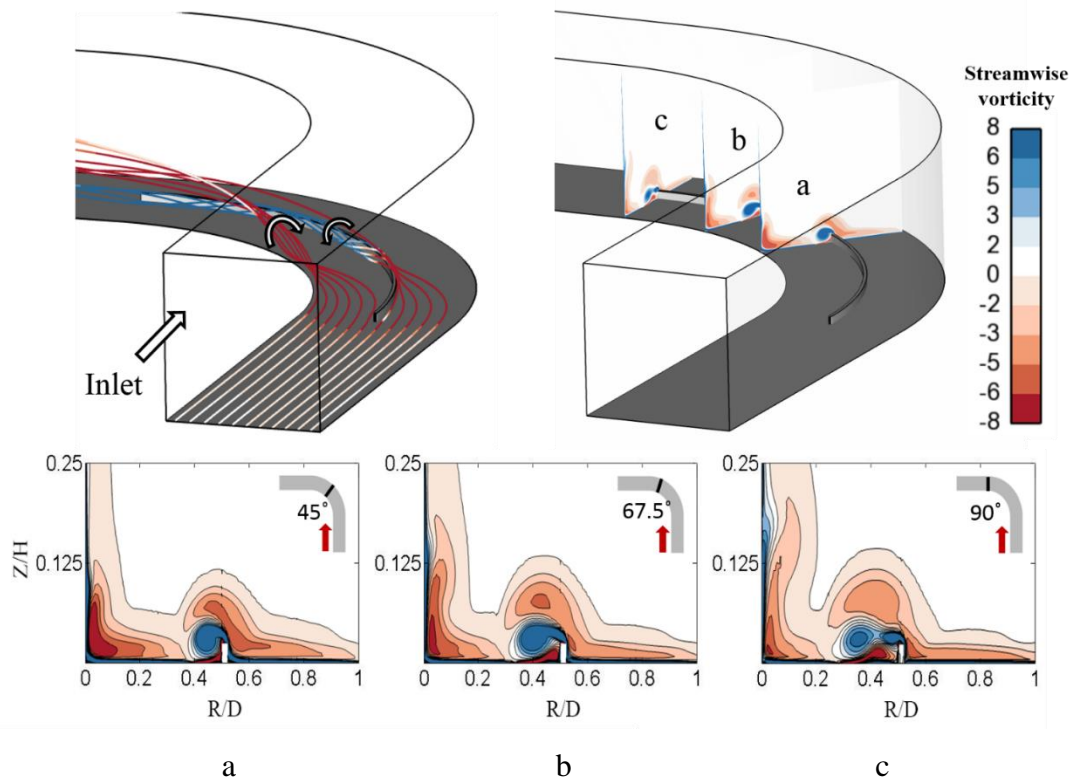
Figure 5.3: Secondary flow structure in the duct with single rib and contours of streamwise vorticity in the cross flow planes (45-degree, 67.5-degree, 90-degree).

5.1.3 Effect of Rib Numbers

Figure 5.4 shows dimensionless streamwise vorticity distributions obtained at 67.5-degree plane of the turning duct for cases with different rib numbers. The ribs divide the duct cross-section equally and rib number ranges from three to seven.

Note that the dimensionless streamwise vorticity distributions for no rib and single rib have already been presented in Figures 5.1 and 5.3 respectively. It can be clearly seen that the multiple ribs can break the passage vortex into several small vortices. As the rib number increases, the strength and size of streamwise vorticity are largely reduced and the broken vortices stay at a lower position.

| (a) 3 ribs | (b) 5 ribs | (c) 7 ribs |
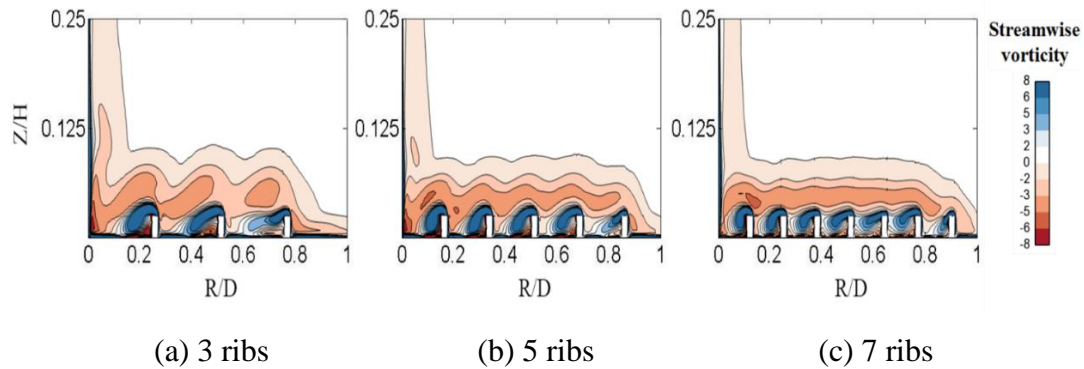
Figure 5.4: Dimensionless streamwise vorticity distributions obtained at 67.5-degree plane of the duct for multiple ribs cases.

5.1.4 Detailed Flow Physics in Multiple Ribs

The flow control mechanism by the multiple near-wall structures in the form of ribs and wavy grooves is further discussed in this section. Note that the rib and groove arrays both are composed of seven units, which are equally spaced in the duct span.

An overview of the vortical flow generated in the controlled turning channel is provided through the sparsely distributed streamlines within the boundary layer, as shown in Fig. 5.5. According to the visualization in the smooth duct (Fig. 5.5a), all the streamlines shown grows into the passage vortex. Similar to the flow behavior in the single rib flow, the streamlines lift off after a short development. Upon the completion of lift-off motion, these streamlines fall into revolution and form the vortex filaments.

(a) No rib   (b) 7 ribs   (c) 7 wavy grooves
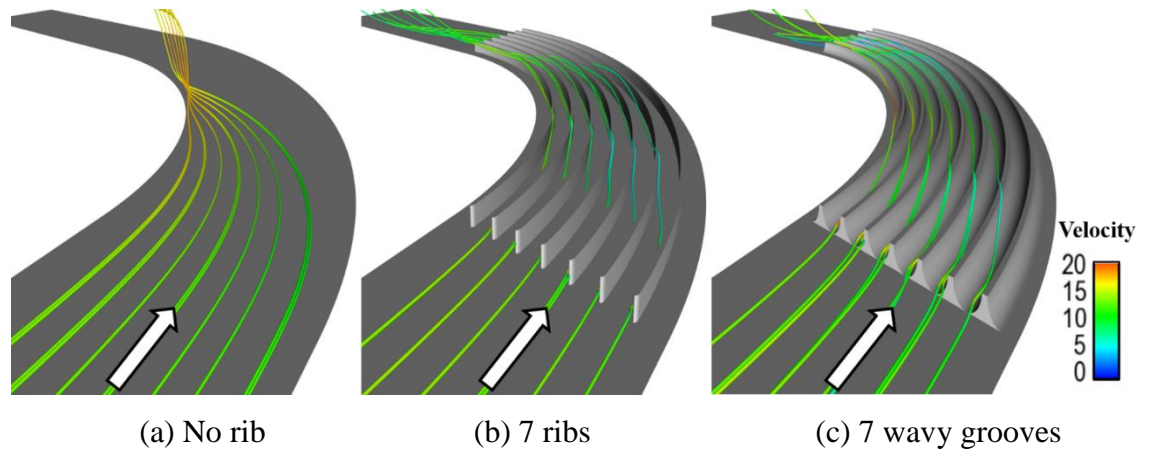
Figure 5.5: Fluid streamlines near the duct floor for case (a) no rib and (b) multiple ribs (b) wavy grooves

Figure 5.6 presents a complete visualization of the vortical structure through the iso-surface of λ_2 (Jeong and Hussain (1995), HALLER (2005)). λ_2 is the second largest eigenvalue of the sum of the square of the symmetrical and anti-symmetrical parts of the velocity gradient tensor which can be used to identify vortices from a three-dimensional fluid velocity field. The undisturbed passage vortex in the clean channel (Fig. 5.6a) lifts away from the flow surface gradually and enters the free stream. This passage vortex is affected by the rib and groove-array, however, with different level of controlling behavior. The same value of λ_2 in the flow field controlled by rib-array illustrates a significantly lower passage vortex together with vortex filaments attached in the close vicinity of the ribs. For the flow control, a lower passage vortex is desired as its interaction with the free stream is reduced. The passage vortex resulted from the groove-array has a height between that of the uncontrolled vortex and the vortex controlled by rib-array. The overlaid streamwise vorticity distribution in the 90-degree plane again indicates the location of passage vortex in the duct. This vortex visualization thus suggests that the wavy grooves array is slightly less efficient than the rib in consideration of passage vortex control.

(a) No rib   (b) 7 ribs   (c) 7 wavy grooves
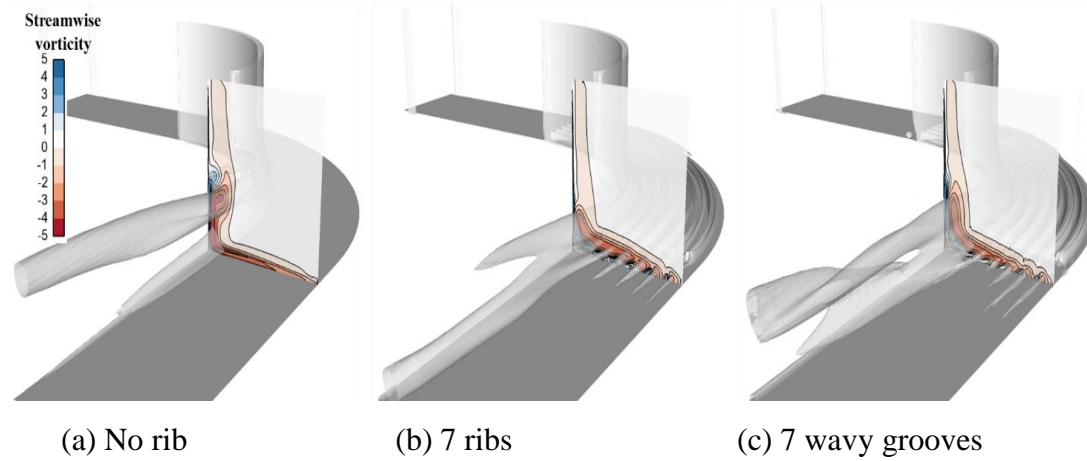
Figure 5.6: Iso-surfaces of λ_2 and dimensionless streamwise vorticity distributions at downstream of the duct passage.

The difference in the controlled passage vortex identified above can be explained through inspections on the evolution of flow structures produced by the two surface geometries. In Fig. 5.7 and Fig. 5.8, four streamwise planes at angles of 15, 45, 60 and 75 degrees are chosen to illustrate the flow development. At the early stage of the turning flow, namely in the 15-degree plane, the near wall flow follows well the sub-channels formed by the ribs and wavy grooves. The blockage provided by the ribs and wavy grooves is sufficient to prevent the cross-flow driven by the lateral pressure gradient gradually built-up after some development. In the 45-degree plane, the structure induced vortex filaments can be seen through the focused vorticity intensity as well as the overlaid projected streamlines. These small vortex filaments grow in intensity in the sub-channels. The space between the neighboring devices is gradually occupied by these filaments and even smaller vortical structures are induced in the late stages, namely in the 60-degree plane. The vorticity distribution is slightly different in the 75-degree plane, where the space between wavy grooves is almost filled with positive vorticity while that between the ribs is only partially filled. The earlier occupation by the vorticity in the sub-channel confirms the earlier lift-off of streamlines in the channels with wavy grooves as observed in Fig. 5.5. Since the cross-flow driven by lateral pressure gradient is allowed earlier

in the case of wavy grooves, it contributes to the passage vortex and results in a higher position than ribs.
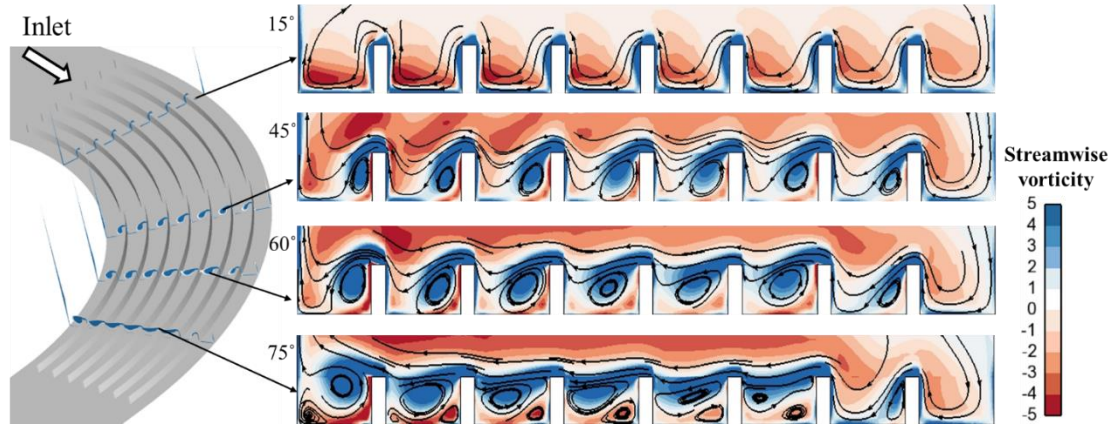
Figure 5.7: Dimensionless streamwise vorticity distributions near ribs region along the duct passage
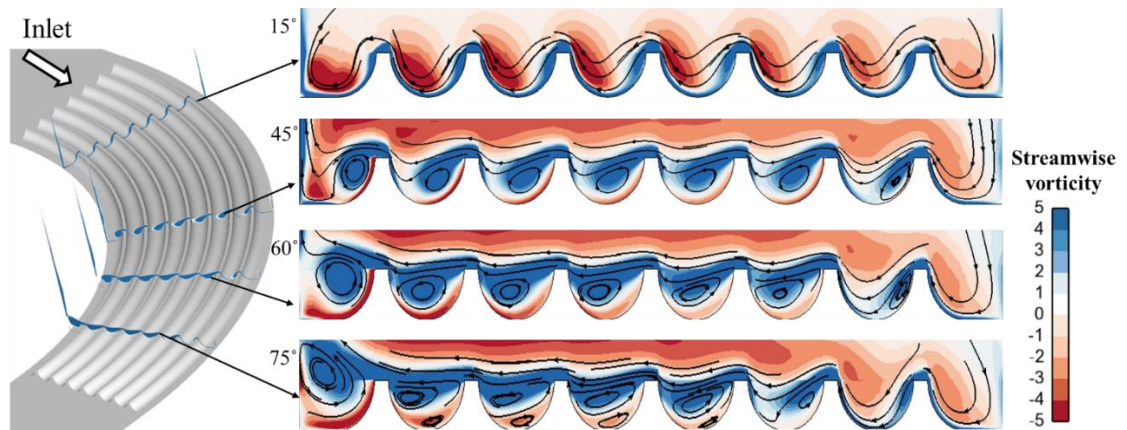
Figure 5.8: Dimensionless streamwise vorticity distributions near the wavy grooves region along the duct passage.

The flow angle relative to that in the mid-span in the same plane also measures the under-turning or over-turning caused by the secondary flow, it is defined as below:

$$\Delta\beta = \beta - \beta_{mid} \qquad (5.2)$$

The positive value of $\Delta\beta$ suggests under-turning, while the negative value suggests over-turning. Distributions of the relative flow angle in the outlet plane are compared in Fig. 5.9. A focused region of strong under-turning is produced within the free stream centered at about 0.2H with peak under-turning of 10 degrees. Both

the rib- and groove-arrays are effective in alleviating the under-turning. The region containing under-turning fluid is diverted away from the free stream and the peak under-turning angle is alleviated to 6 degrees. As a higher passaged vortex is present in the flow controlled by the wavy grooves, the under-turning region is also slightly higher.

(a) No rib   (b) 7 ribs   (c) 7 wavy grooves
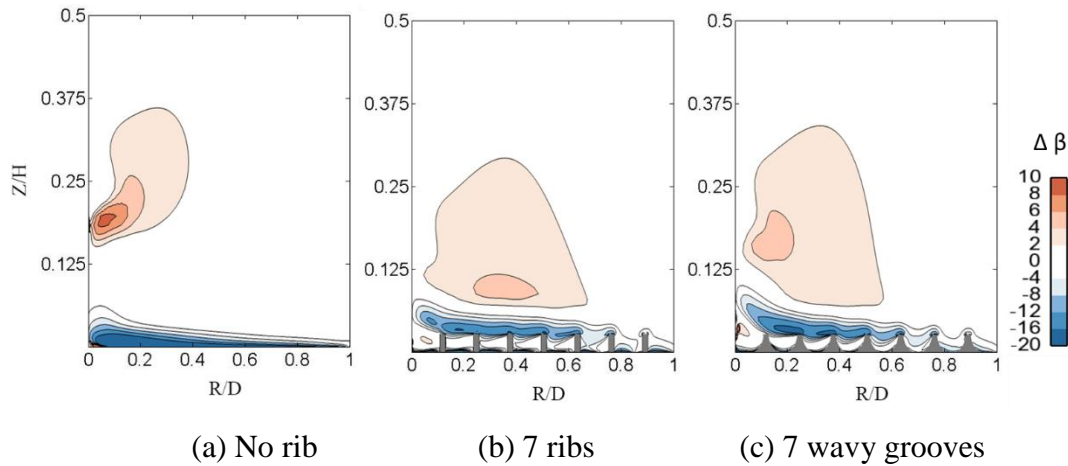
Figure 5.9: Flow angle distributions obtained at 90-degree plane.

Distribution of the aerodynamic loss coefficient C_p in the 90-degree plane is shown in the Fig. 5.10. A high concentration of C_p can be observed over the inner side wall at the height of 0.25H for the smooth wall case and it penetrates free stream with the depth of about 0.2H. This aerodynamic loss is associated with the strong passage vortex. In the channels with the engineered surface structures, as the passage vortex is controlled effectively, the resulted aerodynamics loss becomes weaker, which manifests as the smaller area covered by high C_p concentration. However, due to the presence of the surface structures, there is some additional induced aero-dynamics loss. The engineered surface structure will introduce friction loss due to the enlarged surface area, this effect cannot be avoided. It counteracts the beneficial effect of secondary flow control. Therefore, there is no significant reduction (2.5%) in the mass-averaged loss coefficient between cases with and without the engineered surface structures.

(a) No rib   (b) 7 ribs   (c) 7 wavy grooves
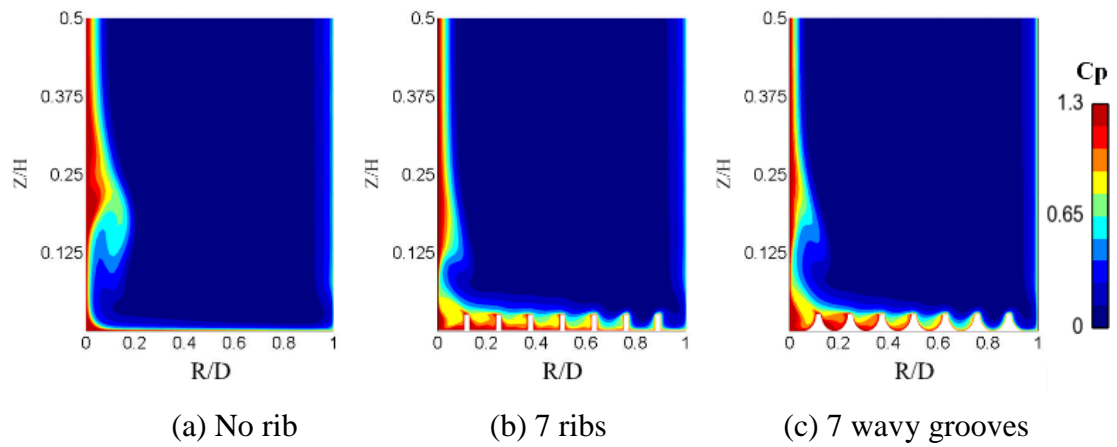
Figure 5.10: Aerodynamic loss coefficient C_p distribution at 90° plane.

5.1.5 PIV Measurement

A PIV experiment is performed in a low-speed wind tunnel to demonstrate the engineered surface structure concept, detailed experiment facility and procedure can be found in Section 3.2. The results from PIV measurement is presented in this subsection.

Figure 5.11 presents the Y and Z component of velocity distribution at the 90-degree plane of the turning duct. The black arrow shows the secondary velocity vector. Further secondary flow filed can be investigated based on V_y and V_z.

Figure 5.12 presents the mean secondary velocity magnitude over the exit plane of the turning duct. The mean secondary velocity is calculated based on Y and Z component of velocity.

$$\text{Mean secondary velocity} = \sqrt{\frac{V_z{}^2 + V_y{}^2}{V_{in}^2}} \tag{5.3}$$

(a) Smooth

(b) 5 ribs
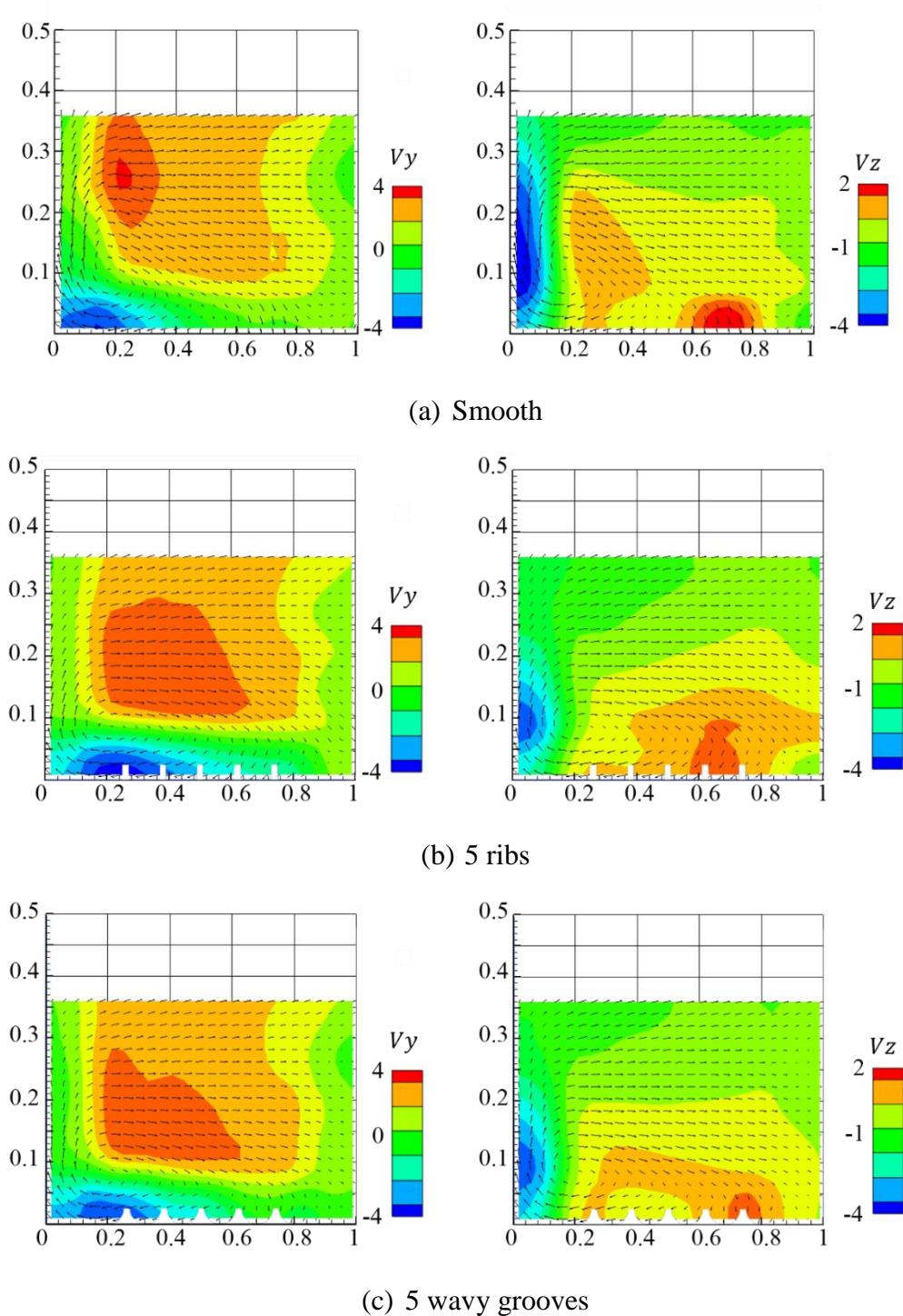
(c) 5 wavy grooves

Figure 5.11: Contour of V_y and V_z for cases (a) smooth (b) 5 ribs (c) 5 wavy grooves.

For the smooth case, a green zone with reduced secondary velocity and a red zone with full strength secondary velocity is apparent in Fig. 5.12a. With the addition

of the engineered surface structure, the high mean secondary velocity regions near the inner wall and end-wall corner are obviously reduced. The surface structure changed the direction and magnitude of the secondary flow along the duct passage and interrupted the convection of the high loss fluid from the end-wall boundary layer by the pressure gradient.

(a) No rib   (b) 5 ribs   (c) 5 wavy grooves
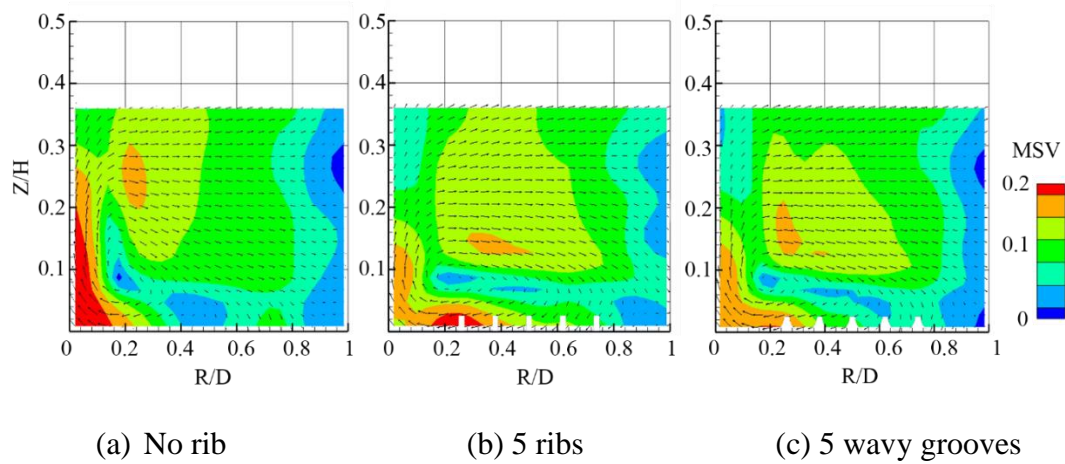
Figure 5.12: Contour of the time-mean mean secondary velocity for cases (a) smooth (b) 5 ribs (c) 5 wavy grooves.

The streamwise vorticity, which definition is contained in Equation 5.4, is one of the most important characteristics of secondary flow. It can detect the strength of each secondary vortex.

$$\Omega_s = \frac{\partial V_y}{\partial x} - \frac{\partial V_x}{\partial y} \tag{5.4}$$

The time-averaged vorticity in the 90-degree plane is shown in Fig. 5.13. In the smooth-wall channel, the vorticity has the peak intensity at the lower-left corner. It extends vertically to a height of Z/H=0.25. The vorticity distribution associated with the passage vortex confirms the simulation result in Fig. 5.6a. Both types of the engineered surface structures are able to manipulate the vorticity distribution. It is clear that the high vorticity along the inner wall is successfully removed. However, due to the presence of the surface structures, the vorticity component starts to be aligned along the wall. The intensity of the induced vorticity is much weaker than the vertical portion of the smooth wall channel.

(b) No rib   (b) 5 ribs   (c) 5 wavy grooves
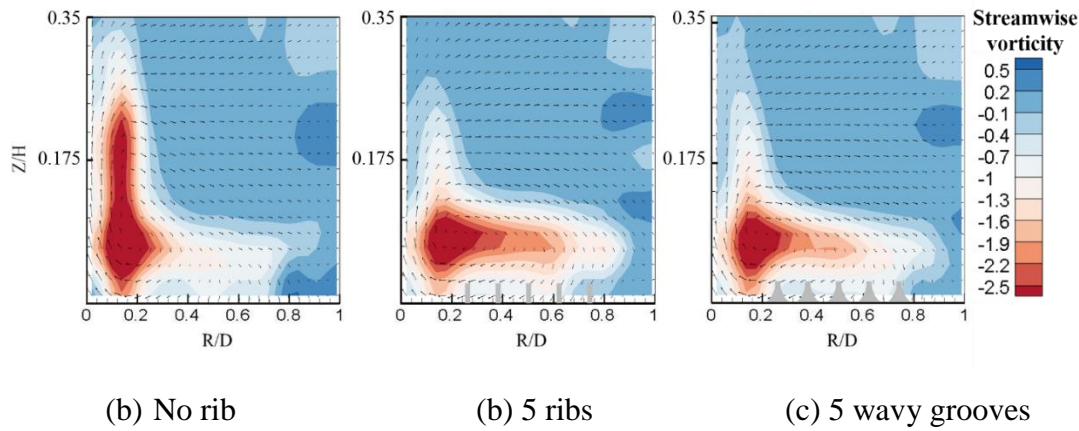
Figure 5.13: Dimensionless streamwise vorticity distributions obtained at 90-degree plane of the duct for cases (a) smooth (b) 5 ribs (c) 5 wavy grooves.

5.2 Secondary Flow Control in Turbine Cascade

Next, the concept of using the engineered surface structure to control secondary flow is applied to a more realistic linear turbine cascade. The ribs also divide the passage cross-section equally and the detailed geometry of the ribs can be found in Subsection 3.1.3.

The prominent features of the secondary flow in the turbine blade passage for the smooth and ribbed surface are visualized through iso-surfaces of λ_2, as shown in Fig. 5.14. For the smooth surface (Fig. 5.14a), the inlet boundary layer separate at the blade leading edge and forms the horseshoe vortex, then the pressure side leg of the horseshoe vortex moves into the passage and merges with the passage vortex by the cross pressure gradient. While the suction side leg of the horseshoe vortex enters into the adjacent passage and becomes the counter vortex which has an opposite sense of rotation to the passage vortex. For ribbed surface (Fig. 5.14b), it can be observed that the pressure side leg of the horseshoe vortex cannot be stopped completely, it still climbs over the ribs and migrates to the suction side. However, the development of pressure side leg of the horseshoe vortex in the turbine passage is affected significantly. The location where the pressure side leg of the horseshoe vortex meets the suction surface is delayed due to the blockage effect of ribs. Since the pressure side leg of the horseshoe vortex and passage vortex have the same rotating

direction, the strength of secondary flow can be reduced by the delay effect. It can also be noticed that there is small vortical structures exit in the rib grooves which is consistent with the findings in the 90-degree duct.

(a) Smooth surface
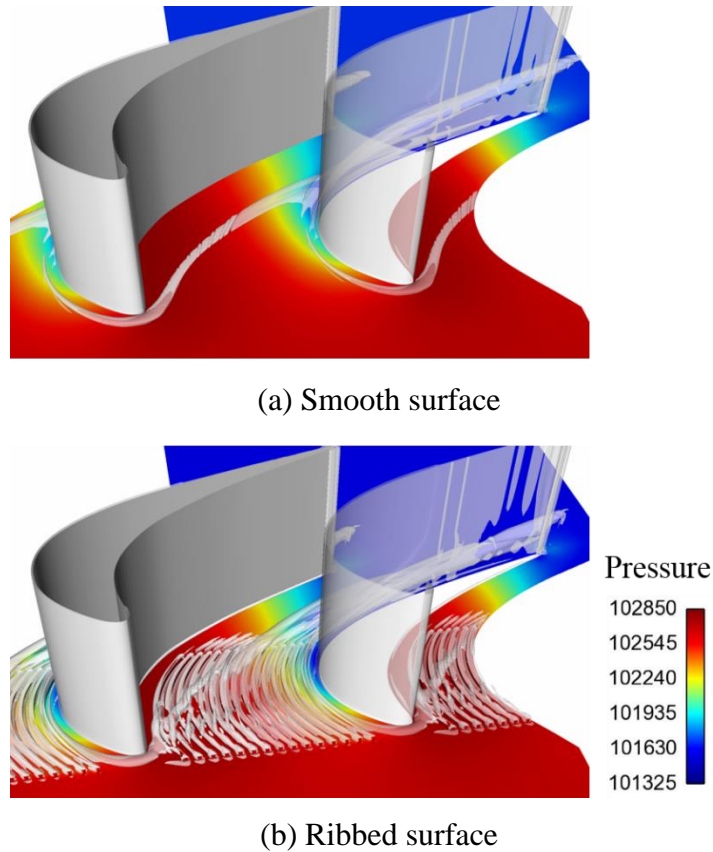
(b) Ribbed surface

Figure 5.14: Iso-surfaces of λ_2 and pressure distribution for the smooth and ribbed surface.

In order to study the development and evolution of the secondary flow, the streamwise vorticity distribution in the three cross planes at 20%, 50% and 70% C_x is shown. The streamwise vorticity is calculated by Equation 5.1 and nondimension-alized by dividing by C_x/V_{in}. For the smooth end-wall surface, the pressure side leg of the horseshoe vortex and passage vortex which has negative streamwise vorticity are quickly swept to the suction side of the blade passage as the flow turning. The high strength of streamwise vorticity region can be found in the suction surface and end-wall corner and can be lifted to the height of 0.125S at 70% C_x. While for the ribbed end-wall surface, the cross motion and the strength of the passage vortex are

largely reduced by the blockage effect of ribs. Similar to the observation in 90-degree turning duct, smaller scale of vortices is also introduced by the ribs with an opposite sign. It can also be noticed that the positive vorticity is occupied the rib grooves at 50% C_x which is earlier than that in the simplified duct.

(a) Smooth surface   (b) Ribbed surface
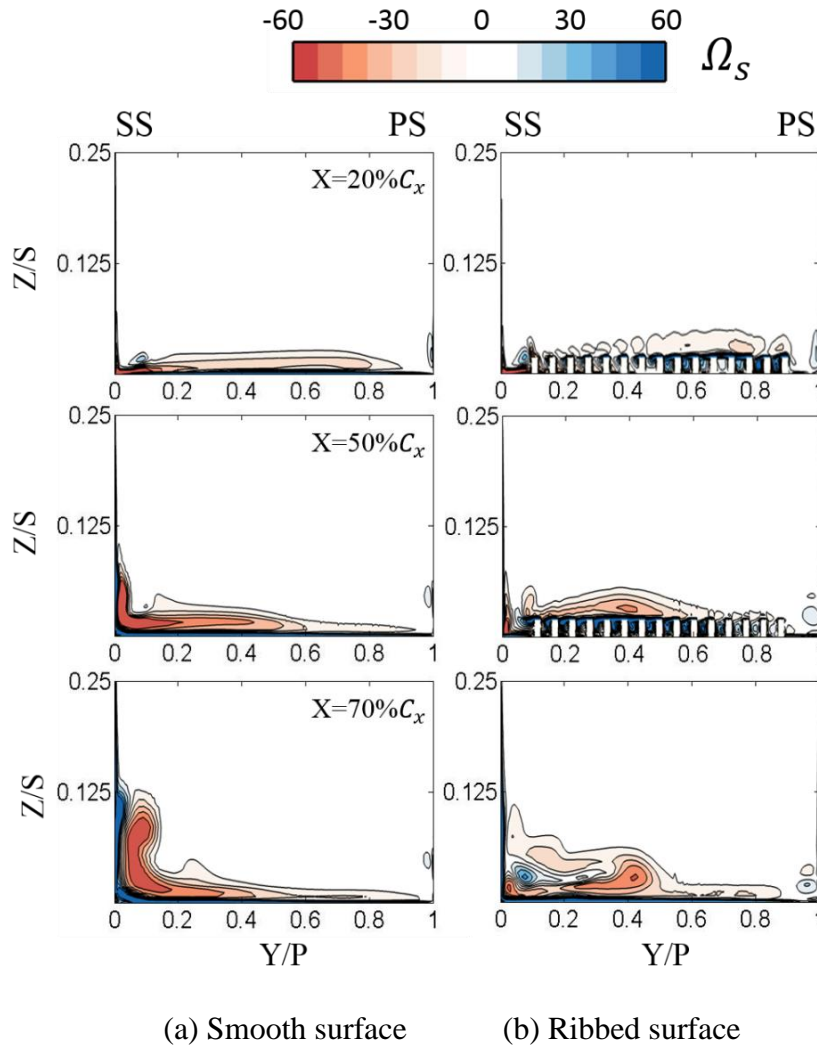
Figure 5.15: Streamwise vorticity distribution at three cross sections.

The local entropy generation rate in the turbine passage is discussed next. The detailed definition of the entropy generation rate per unit volume can be found in Section 2.3. The units of entropy generation rate are W/m^{3}K, which tends to be a large number. In the following results, all the values plotted are non-dimensionalised by dividing by $\rho_{out} V_{out}^3 / C_x T_{out}$. Figure 5.16 shows contours of this quantity at various locations through the cascade. For the smooth surface, the entropy generation rate increasing region is associated with the horseshoe vortex at 20% C_x, especially

in the pressure side leg as it crosses the passage towards the blade suction side. As the flow turning, the rates become larger at 50% C_x when the vortex starts to interact with the suction side surface. A rapidly increasing of entropy generation rate can be observed both on the suction side surface of the blade and the core of the passage vortex at 70% C_x. With the addition of ribs, the entropy generation rate associated with passage vortex is largely reduced along the turbine passage. High entropy generation rate region occurs near the rib surface.
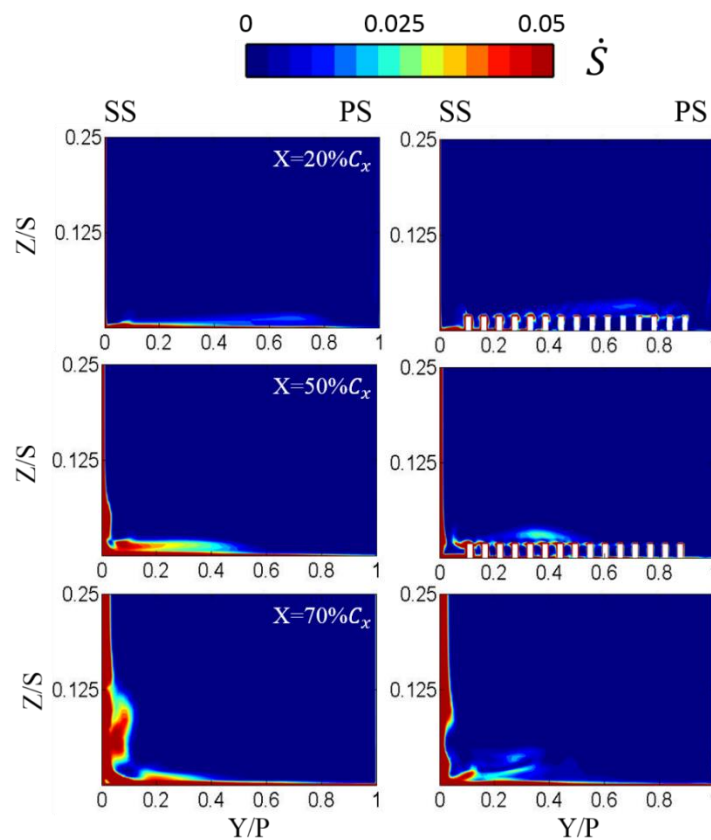
Figure 5.16: $\dot{S}$ distributions at three cross sections.

Figure 5.17 presents the vortical structure through the iso-surface of λ_2. The λ_2 value is selected the same for the smooth and ribbed surface. The streamwise vorticity distribution at 0.12 chord downstream of the passage is also shown to indicate the strength and location of passage vortex. For the smooth surface case, the passage vortex is lifted from the end-wall early and associated with the high red streamwise vorticity region. With the addition of rib structure, the location of the passage vortex is close to the end-wall at the downstream of the turbine passage and

the streamwise vorticity of passage vortex is also reduced.

(a) Smooth surface (b) Ribbed surface
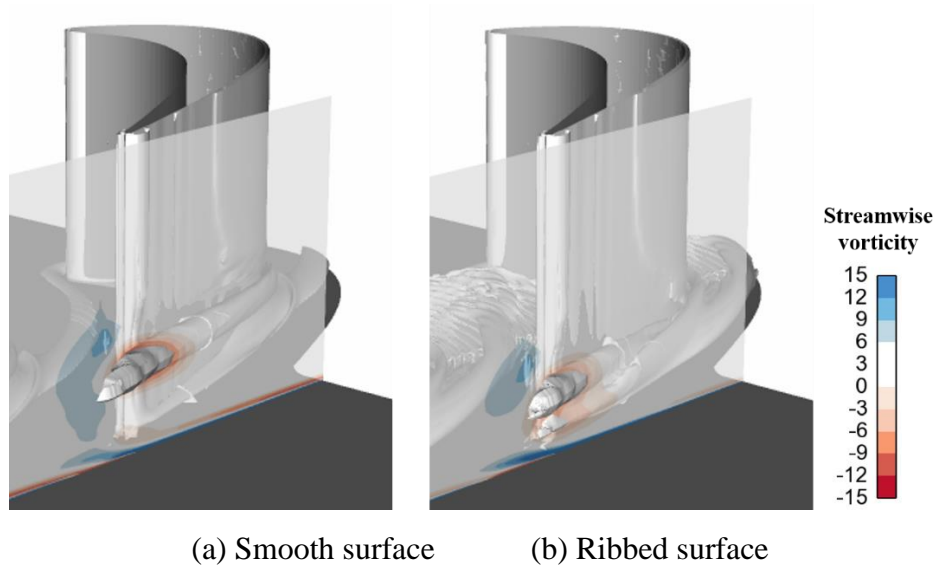
Figure 5.17: Iso-surfaces of λ_2 and dimensionless streamwise vorticity distribu-
tions at downstream of the turbine blade passage.

Figure 5.18 presents the distribution of the total pressure loss coefficient C_p at 0.12 chord downstream of the blade trailing edge. For the smooth surface case, it can be clearly observed that a passage vortex loss core is generated at the height of 0.15S. With the addition of the engineered surface structure, the passage vortex loss core is diminished significantly, and a higher loss region occurs near the end-wall. The differences in overall mass-averaged total pressure loss coefficient between the smooth and ribbed surface are less than 2%, which are within uncertainties in RANS simulation.
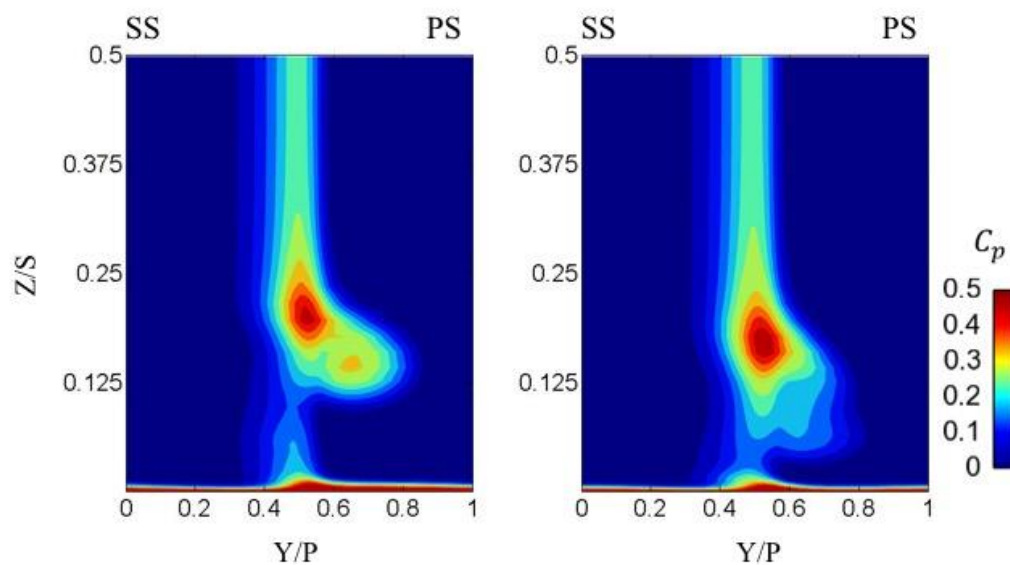
(a) Smooth surface   (b) Ribbed surface

Figure 5.18: Aerodynamic loss coefficient C_p distributions obtained at 0.12 chord downstream of the cascade blade.

Considering the various operating conditions in the real engines and complexity of secondary flow, the intention of this thesis is not to demonstrate a complete story about the engineered surface structure concept. Rather, it tries to open a new research option for end-wall secondary flow control. More geometry optimization should be conducted in the future work. Strategy-wise, the geometry of the engineered surface structure should be optimized according to the inlet boundary layer thickness, the turbulence level, blade loading and Reynolds number.

5.3   Summary

The potential of the engineered surface structures in controlling the undesired end-wall secondary flow is explored in this chapter. Due to the limitation of the experimental facility, only low-speed experiment and simulation are performed. The Reynolds number, which is based on the maximum inlet velocity and the duct width, is 69000. A simplified 90-degree turning duct is first used to control the secondary

flow. Studying this simplified flow model is useful in obtaining the physical understanding of the working mechanism of this flow control concept without considering the complex horseshoe vortex developed in the turbine system. It is found that a single rib installed on the end-wall can block the cross-flow motion driven by the lateral pressure gradient and result in a weaker passage vortex. Arrays of rib and wavy grooves are found to be effective in alleviating passage vortex as well as flow over-turning. The groove array is shown slightly different control result than the rib array, which is attributed to the earlier formation of the vortex filaments induced by the wavy grooves.

The engineered surface structure effect on secondary flow control in a linear turbine cascade is then investigated through numerical study. The comparisons between smooth and ribbed surface suggest that the end-wall ribs greatly reduce the strength of the passage vortex and alleviate the lift up of the passage vortex.

The physical understanding presented in the present study would the help the potential implementation of this flow control concept in gas turbine aerodynamic design.

Chapter 6

Purge Air Cooling Enhancement

The concept of the engineered end-wall surface structure is applied to purge air cooling enhancement in this chapter. The purge air flow structure and its interaction with the secondary flow in a 90-degree turning duct are presented first. The cooling enhancement mechanism with the ribbed surface is then discussed. The cooling effectiveness and Net Heat Flux Reduction (NHFR) obtained from experimental data are presented. The feasibility of enhancing purge air cooling effectiveness through the engineered surface structure is then experimentally and numerically investigated in a low-speed turbine cascade. The working mechanism and flow physics associated with the end-wall ribs are discussed based on detailed CFD analysis. Enhanced cooling effectiveness and net heat flux reduction are compared and analyzed from both experimental data and CFD results in the followed sections. Finally, in order to represent real engine operating conditions, the purge air cooling effectiveness is studied in a high-speed flow.

6.1 Cooling Performance in a 90-Degree Turning Duct

6.1.1 Purge Air Flow Structure

In order to investigate the effect of the engineered end-wall surface structure on purge air cooling enhancement, an additional purge air system is added to the computational domain and experimental setup. The purge air is injected into the turning duct through an inclined slot. The detailed slot geometry and purge air blowing ratio can be found in Section 3.3. The end-wall ribs only cover the angular range from $0°$ to $45°$ and the latter half of the turning duct is smooth.

The working mechanism of purge air cooling is quite similar to conventional film cooling technique. A thin layer of low temperature air is expected to cover the end-wall surface effectively. To visualize the cold purge air coverage area, Figure 6.1 shows an iso-temperature surface θ, defined as,

$$\theta = \frac{T - T_c}{T_\infty - T_c} = 0.6 \qquad (6.1)$$

where T_c is the cold purge air temperature, T_∞ is mainstream temperature and T is the local temperature. The parameter θ also represent the purge air concentration (a lower θ value indicates a colder local fluid temperature).

For the smooth end-wall case, driven by a radial pressure gradient, the iso-temperature surface associated with cold purge air quickly sweeps towards the duct inner side. Figure 6.1b shows that the ribbed surface effectively extends the iso-temperature further downstream from about 45º to about 60º, after which the three-dimensional vortical motion occurs.

(a) Smooth surface   (b) Ribbed surface
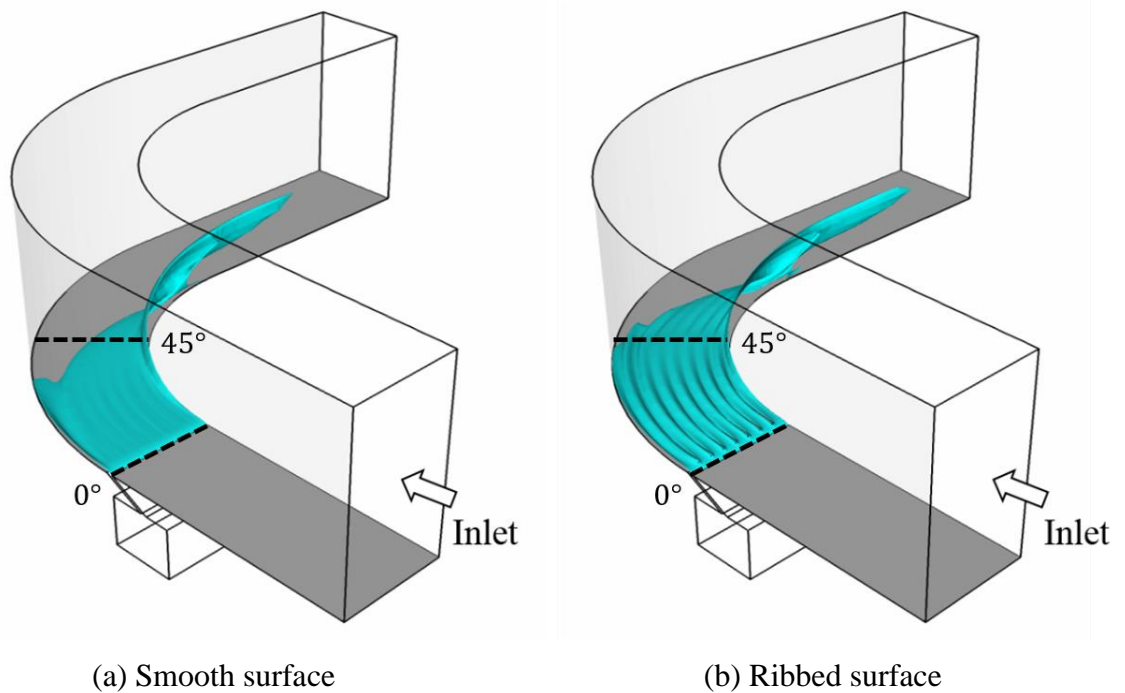
Figure 6.1: An iso-temperature surface with $\theta = 0.6$.

Figure 6.2 shows the non-dimensional fluid temperature θ distribution at three angular cross sections along the duct passage. The cross sections are located at 30º, 45º and 60º of the turning duct. In the duct with the smooth end-wall surface, the low temperature air gradually moves from the outer wall to the inner wall as the fluid travels along the passage. At the 60º plane, most of the cold air lifts off away from the end-wall and the passage vortex contains a majority of the purge air. In contrast, for the ribbed surface, most purge air can stay near the end-wall and fully occupy the rib grooves at both 30º and 45º cross sections, and this is even more apparent at the 60° section. Compared with the smooth case, the near end-wall fluid temperature with ribs is much lower.
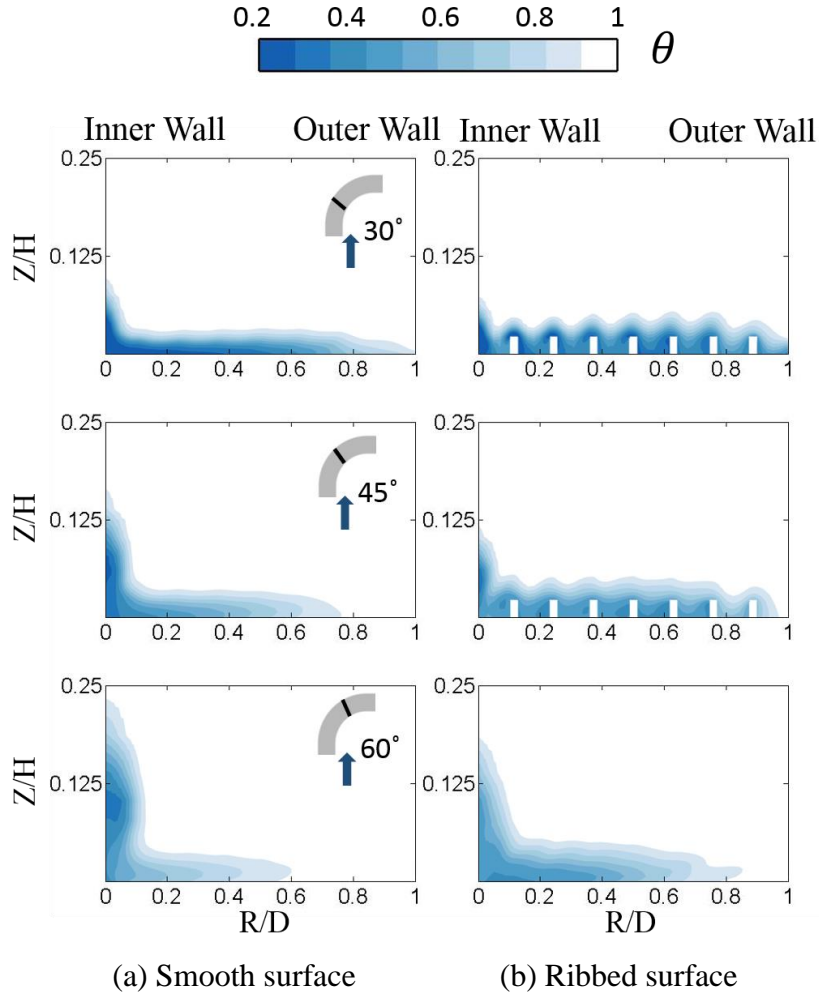
Figure 6.2: Non-dimensional temperature θ distribution at three angular cross sections.

The secondary flow in the turning duct is associated with the streamwise component of vorticity. Three typical radial cross-sectional planes at 30°, 45° and 60° were extracted to reveal the evolution of the secondary flow. The streamwise vorticity (Ω_s) is the tangential component in a cylindrical coordinate system, and it is calculated as

$$\Omega_s = \Omega_x cos\beta_{mid} + \Omega_y sin\beta_{mid} \tag{6.2}$$

where β_{mid} is the relative angle between streamwise direction and X axis in midspan. Ω_x and Ω_y is the vorticity component in X and Y direction respectively. In Figure 6.3, the streamwise vorticity is further nondimensionalized by D/V_∞. The

negative vorticity (red color), is associated with the secondary flow vortex, while the positive vorticity (blue color) represents the vortex which rotates oppositely with the secondary flow vortex.

(a) Smooth surface   (b) Ribs surface
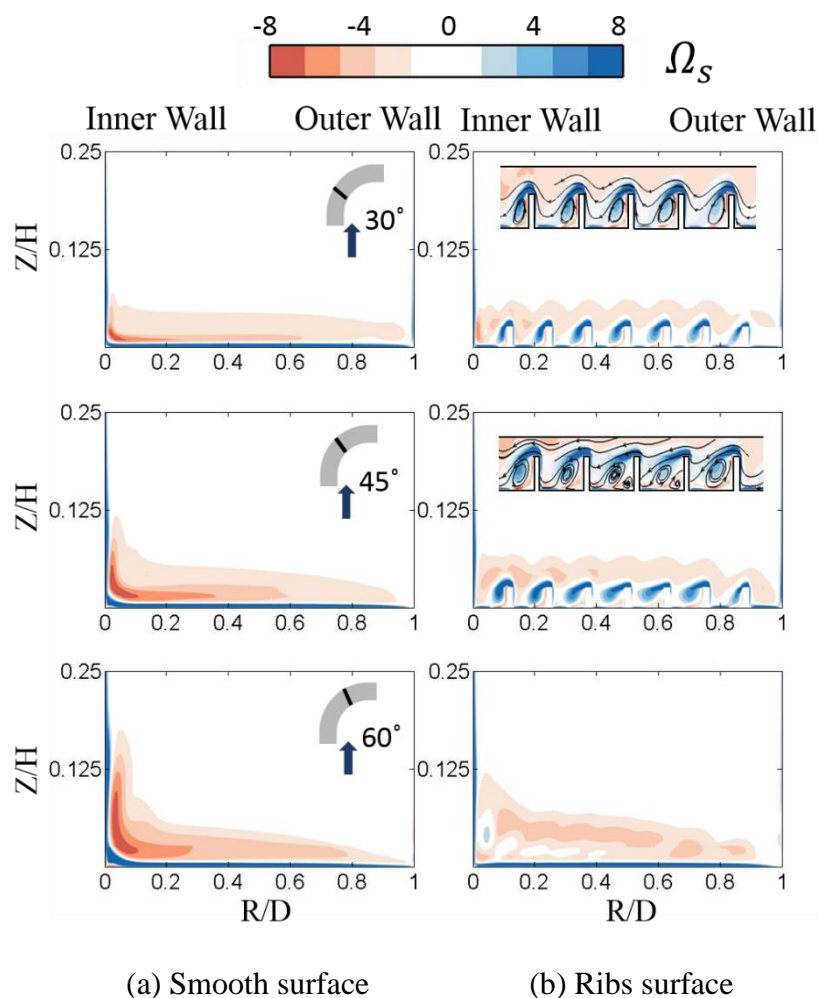
Figure 6.3: Streamwise vorticity distributions at three angular cross sections.

Figure 6.3a shows that, in the duct with smooth end-wall, the concentration of negative vorticity gradually builds up at the lower inner-corner within the selected angular range, suggesting the growth of the secondary flow vortex.

In Fig. 6.3b, the ribs on the end-wall surface modify the vorticity distribution throughout the angular range. Apparently, the intensity of negative vorticity associated with the secondary flow vortex is reduced. In the smooth surface duct, the secondary flow accumulates in the inner-end-wall corner and gradually extends along

the inner vertical wall; however, the presence of the ribs eliminates this accumulation of secondary flow effectively. The ribs also introduce vortices with an opposite sign, which have been revealed as vortices of a smaller scale than the secondary flow vortex. Since the ribs only extend from 0º to 45º in the present design, the array of positive vorticity associated with these ribs disappears in the cross section at 60º.

(a) Smooth surface   (b) Ribs surface
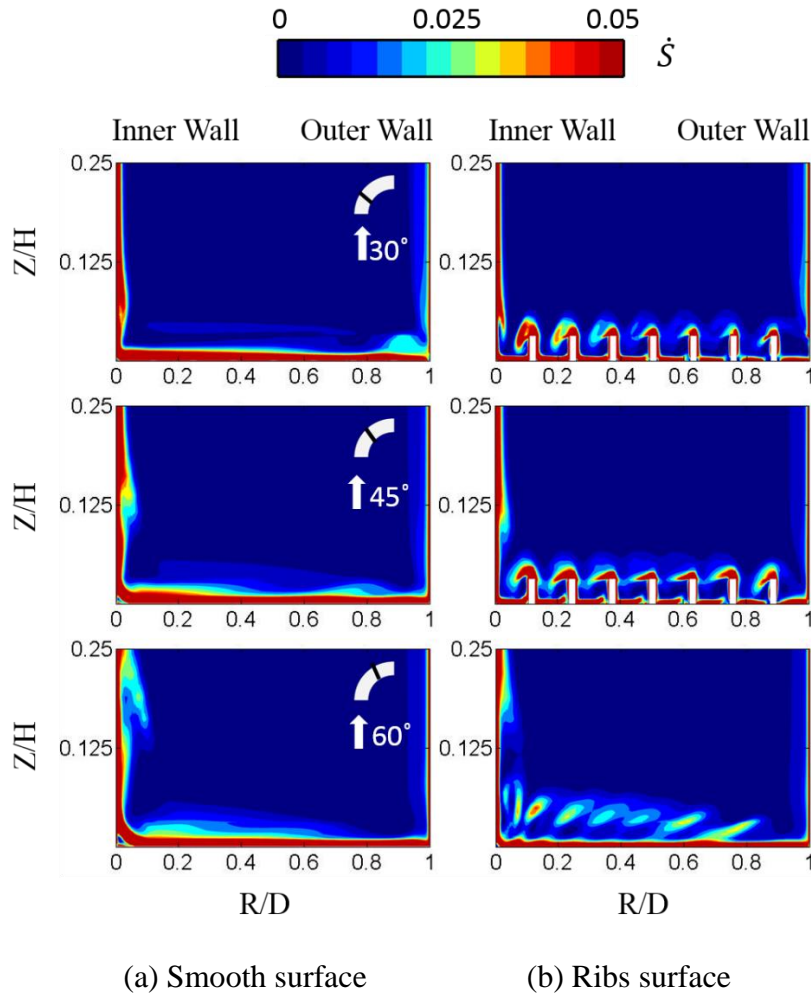
Figure 6.4: $\dot{S}$ distributions at three angular cross sections.

Figure 6.4 shows the dimensionless entropy generation rate per unit volume distributions at three angular cross sections along the duct passage. The details of entropy generation rate per unit volume can be found in Section 2.3, and the rate value is presented in dimensionless form by dividing by $\rho_{out} V_{out}^3 / C_x T_{out}$. For the smooth surface, a thick layer with high entropy generation rate can be found on the end-wall surface. As the flow turning, the rate increases rapidly on the inner surface. While

with the addition of ribs, the entropy generation rate increases when the flow cross over the rib structures. At 60-degree plane, the purge air exits the rib grooves and sweeps towards the inner surface by the cross pressure gradient. Thus high rate occurs due to the mixing process.

In order to consider all the contributions due to viscous effects and heat transfer between the mainstream and purge flow, the aerodynamics loss coefficient is defined as (Lakshminarayana (1996))

$$\zeta = 1 - \frac{\left(\dot{m}_c \cdot c_{p,c} \cdot T_{0,c} + \dot{m}_{in} \cdot c_{p,in} \cdot T_{0,in}\right)\left(1 - \left(\frac{P}{P_0}\right)^{\left(\frac{\gamma-1}{\gamma}\right)}\right)}{\dot{m}_{in} \cdot c_{p,in} \cdot T_{0,in} \cdot \left(1 - \left(\frac{P_{mid}}{P_{0,in}}\right)^{\left(\frac{\gamma-1}{\gamma}\right)_{in}}\right) + \dot{m}_c \cdot c_{p,c} \cdot T_{0,c} \cdot \left(1 - \left(\frac{P_{mid}}{P_{0,c}}\right)^{\left(\frac{\gamma-1}{\gamma}\right)_c}\right)} \quad (6.3)$$

Figure 6.5 shows the distribution of aerodynamics loss coefficient at the 90-degree plane in smooth and ribbed cases. It can be observed that the loss core of the passage vortex is close the end-wall with the addition of ribs. In the corner region between inner wall and end-wall the loss is increased slightly. The mass-averaged loss coefficient between smooth and ribbed cases is less than 2.3%. Therefore the additional aerodynamic penalty introduced by the small ribs is negligible.

(a) Smooth surface   (b) Ribbed surface
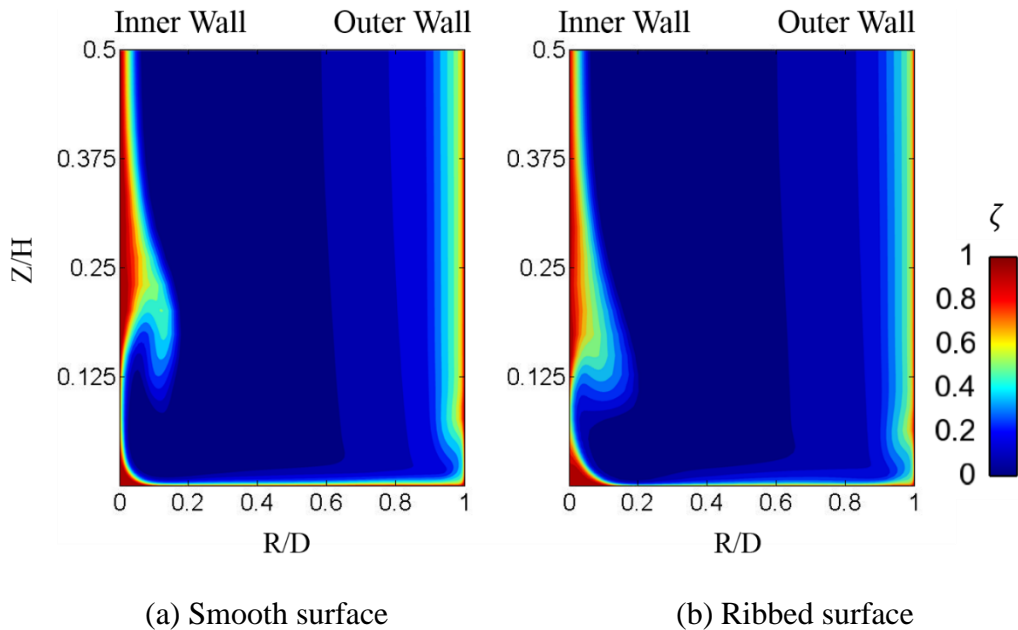
Figure 6.5: Distributions of ζ at the exit plane.

6.1.2 Cooling Effectiveness

Film cooling effectiveness measured over the wall after the ribbed and smooth end-wall surfaces (from 45° to 90°) is presented and further compared with CFD analysis in this section.

The calculation of film cooling effectiveness η follows the relation below

$$\eta = \frac{T_\infty - T_{ad}}{T_\infty - T_c} \tag{6.4}$$

where T_c is the cold purge air temperature, T_∞ is the mainstream temperature and T_{ad} is the adiabatic wall temperature.

Figure 6.6 presents the contours of η obtained in the experiments for both end-walls. The region of higher η, namely $\eta>0.5$, can be clearly observed in Fig. 6.6a. At the angular position of 45°, the high film cooling efficiency covers about half of the duct width, while the highest η is close to the inner side wall. The region of high η quickly shrinks in size further downstream and it fully disappears after 70°. The rapid decay of the film cooling effectiveness is caused by the sweeping effect of the secondary flow vortex, which carries the cold purge air flow away from the end-wall towards the inner wall through its vortical motion. In contrast, the ribbed surface has improved the cooling performance significantly. The region of $\eta>0.5$ covers the entire duct width at the angular position of 45°, while the high η region extends further downstream till 80° near the inner wall. The total area with good cooling air coverage over the ribbed surface is about twice of that over the smooth surface. Some very high η regions with $\eta>0.7$ can still be observed, and they are aligned with the grooves formed between adjacent ribs. This discreet distribution of high cooling effectiveness region is due to the near wall small scale vortex array generated by the ribs. It seems that these small vortices are very efficient in maintaining the purge air flow close to the end-wall surface.

(a) Smooth surface   (b) Ribbed surface
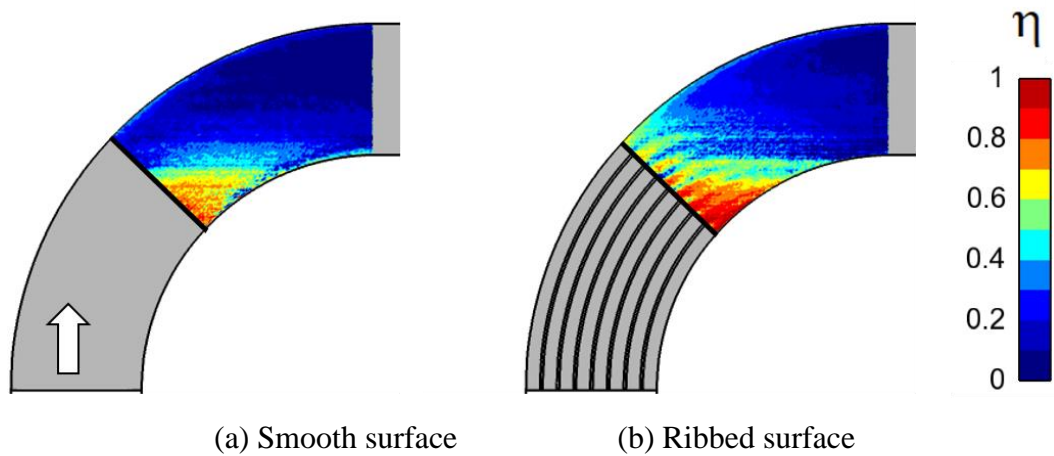
Figure 6.6: Film cooling effectiveness (experimental data).

(a) Smooth surface   (b) Ribbed surface
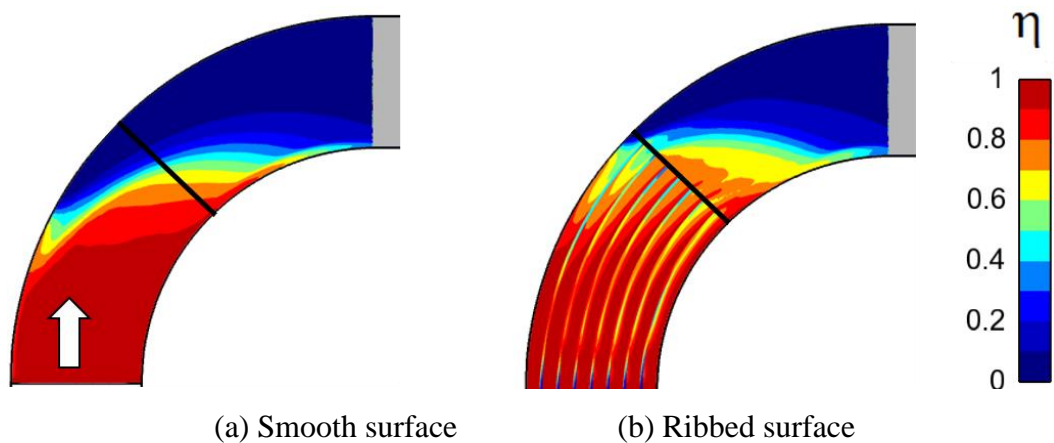
Figure 6.7: Film cooling effectiveness (CFD results).

Figure 6.7 shows the film cooling effectiveness calculated by numerical simulation. The qualitative trend is consistent. The simulation has a reasonably good agreement with the experimental data in terms of the overall cooling effectiveness distribution and the enhancement by the ribs is also quite similar in terms of the increased coverage area. Very high cooling performance inside the rib grooves can be observed by the simulation. Both experiment and CFD results confirm that the ribbed surface enables cooling enhancement by maintaining the cold purge air attached to the end-wall to a much larger extent. Quantitively, the CFD data are less diffused than the measurement results. Nearly no cooling flow can be observed from some of the grooves near the outer wall, while there is more cooling coverage near

the inner wall region. Such discrepancy is a common performance from a standard RANS solver. The interaction between secondary flow and cooling fluid needs to be better resolved by CFD solvers with high-fidelity.
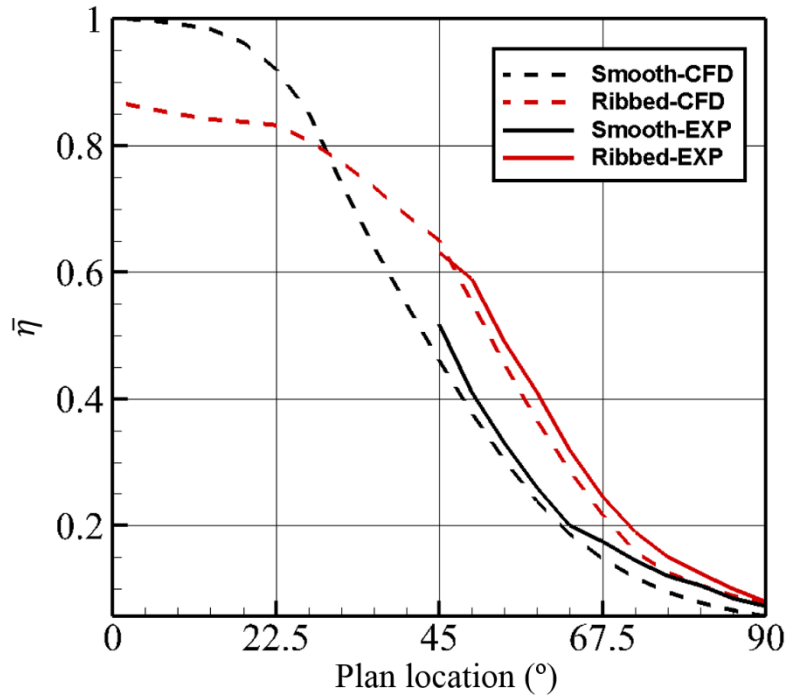
Figure 6.8: Laterally-averaged film cooling effectiveness $\bar{\eta}$ along the duct passage for both experimental and CFD results.

The cooling performance along the duct passage is further illustrated through the comparison of the Laterally-averaged film cooling effectiveness for the smooth (black color) and ribbed surface (red color), as shown in Fig. 6.8. The CFD result is shown as dash lines, while the experimental data is presented as solid lines. After the 20° location, a rapid decline of the $\bar{\eta}$ value can be observed because the passage vortex sweeps the purge air from the outer wall to inner wall. For the ribbed surface, the $\bar{\eta}$ starts from about 0.85 since the purge air is not able to fully cover the top surface of the rib structure. Due to the blockage effect of rib structure, the early overturning of the purge air is largely reduced, and more cooling air can stay near the end-wall. Therefore, comparing with the results from the smooth case the value for the ribbed surface decreases more gradually. The experimental data have a very good agreement with CFD results both qualitatively and quantitatively in the region where test data is available.

6.1.3 Net Heat Flux Reduction (NHFR)

To further examine the cooling performance, a net reduction in heat transfer relative to an uncooled duct channel is calculated. This quantity is calculated by using measurements of the film cooling effectiveness and the change in heat transfer coefficients (h_f/h_0) for the film cooled surface to determine the Net Heat Flux Reduction (NHFR), which is the fractional decrease in heat flux due to film cooling

$$NHFR = 1 - \frac{q_f''}{q_0''} \tag{6.5}$$

q_f'' and q_0'' represent the convective heat flux with film cooling and the convective heat flux without film cooling respectively, and they are represented as below:

$$q_f'' = h_f(T_{ad} - T_w) \tag{6.6}$$

$$q_0'' = h_0(T_\infty - T_w) \tag{6.7}$$

The net heat flux reduction can be further written as:

$$\Delta q_r = 1 - \frac{h_f}{h_0}(1 - \eta\varphi) \tag{6.8}$$

The non-dimensional metal temperature φ is defined as:

$$\varphi = \frac{T_\infty - T_c}{T_r - T_b} \tag{6.9}$$

where T_∞ is the mainstream temperature, T_c is the coolant total temperature, T_b is the blade metal temperature, T_r is the recovery temperature. A value of 1.6 is used for typical engine conditions (Sen et al. (1996)).

(a) Smooth surface   (b) Ribbed surface
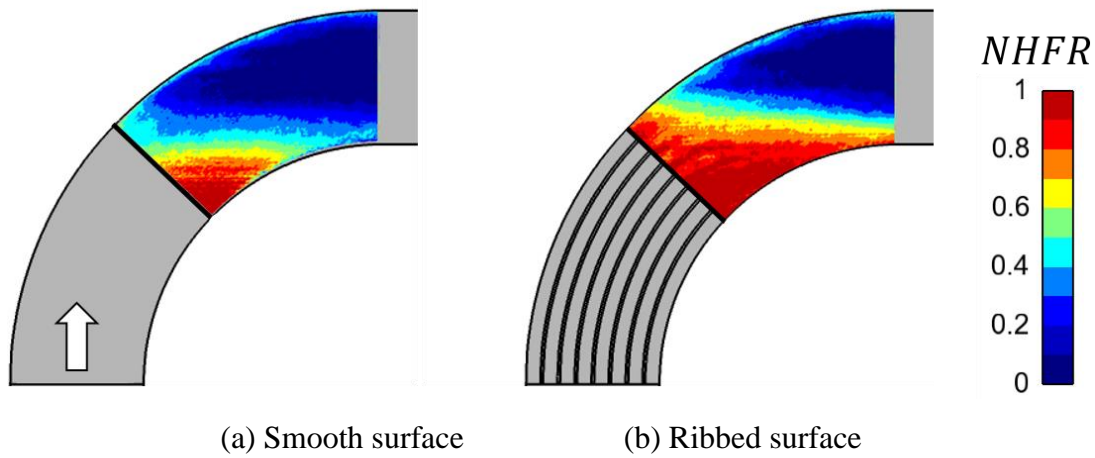
Figure 6.9: Distributions of NHFR (experimental data).

(a) Smooth surface   (b) Ribbed surface
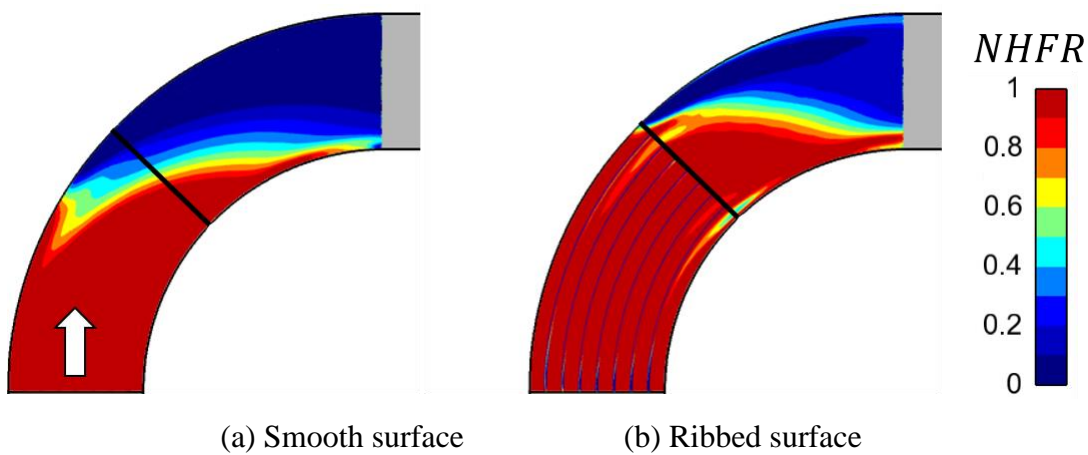
Figure 6.10: Distributions of NHFR (CFD results).

The NHFR distributions on the smooth and ribbed surfaces in the experiments are shown in Fig. 6.9. The blue color represents the region with low heat flux reduction, while the red color corresponds to the region benefiting from purge air cooling. Figure 6.10 shows a similar pattern to the experimental data in Fig. 6.9. In comparison, the region of reduced net heat flux shown in red color takes up the much larger area over the ribbed surface. On the rear part of the end-wall, the purge air has already been largely swept away by secondary flow and very low NHFR can be found (blue region). It can be seen that with the addition of rib structure, more area of the end-wall region can benefit from purge air cooling.

Then the NHFR at the latter half of the end-wall is area-weighted average for

both experimental and CFD results. Overall, the ribbed surface provides a 53% increase in area-weighted average NHFR from experiments and a 60% increase from CFD study.

6.1.4 Practical Considerations and Design Optimization Strategy

For practical application in the turbine system, the ribbed surface has to be fully protected by the coolant without being exposed to the hot gas. Even with a significant improvement in NHFR, the rib design has to be carefully optimized to achieve a reasonable level of cooling effectiveness near the rib structures for their long-term survival.

As pointed out in the previous discussions, there is a poor coolant coverage over the rib top surface near the duct entry region. The non-dimensional temperature θ distribution near entry region is shown in Fig.6.11a for the previous ribbed end-wall design. The purge air injected through the slot blocks the cooling fluid and it cannot reach the top surface of the rib. Apparently, the rib height selected needs to be further optimized.

(a) h/δ=0.25 (b) h/δ=0.15
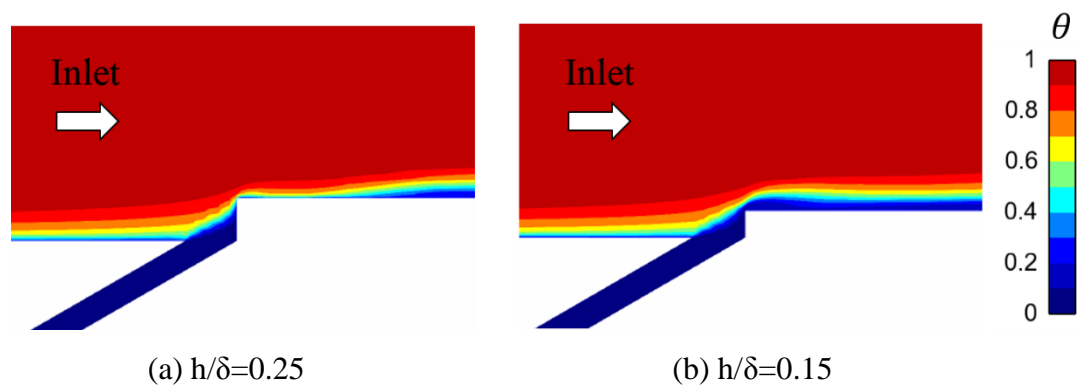
Figure 6.11: Non-dimensional temperature θ distribution near the purge air entry region for ribbed surface.

Improved cooling performance is achieved from another optimized CFD case with a 40% reduction of overall rib height, as illustrated in Fig. 6.11b and Fig. 6.12. The film cooling effectiveness near the upstream region is significantly enhanced by

adding ribs with an optimal height.

<table>
<tr><td>(a) h/δ=0.25</td><td>(b) h/δ=0.15</td></tr>
</table>
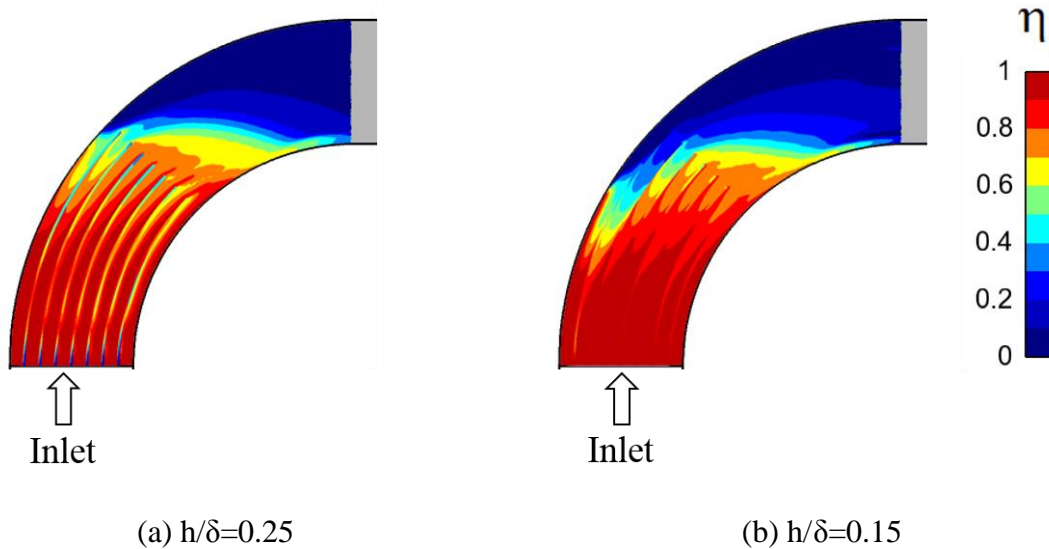
Figure 6.12: Distributions of film cooling effectiveness.

Another region which deserves further attention is the ribs close to the outer wall. The discrete blue stripes showed from the experimental data in Fig. 6.6b, as well as the low η region near the duct outer wall in Fig. 6.12, indicate the ribs could be vulnerable for hot gas. Figure 6.13 presents fluid streamlines colored by temperature which illustrate the development of purge air flow within the grooves of the ribbed end-wall. Apparently, the ribs cannot completely stop the radial migration of the purge air flow, especially near the outer wall region. According to many previous studies related to purge air cooling (Wright et al. (2007); Knost and Thole (2004); Nicklas (2001)), additional film cooling is always needed to provide sufficient coverage to the end-wall. The ribbed end-wall concept should also be combined with conventional film cooling (or effusion cooling) to overcome its limitation. However, results from the present study indicate that the needs from conventional end-wall cooling design should be greatly reduced.

(a) Smooth surface   (b) Ribbed surface h/δ=0.25   (c) Ribbed surface

h/δ=0.15
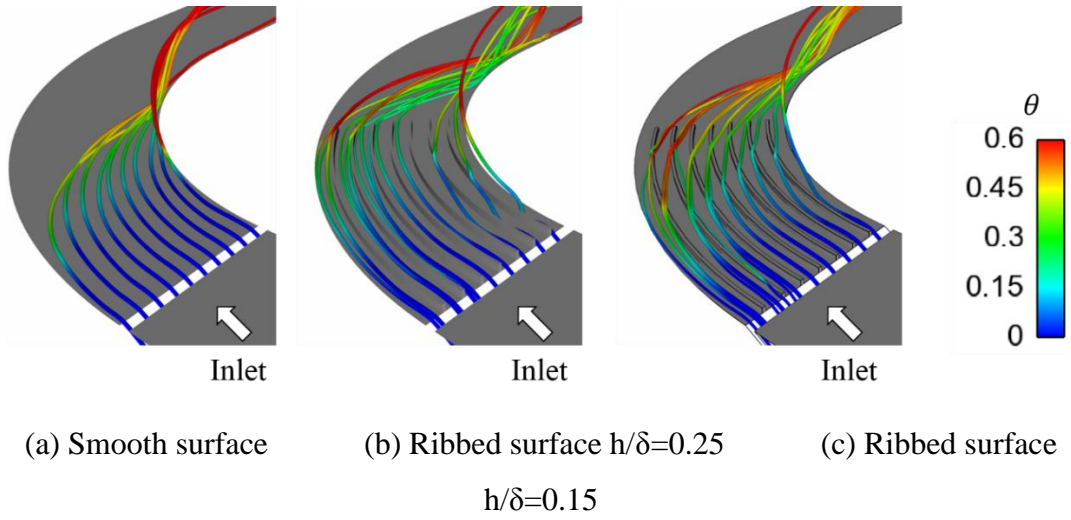
Figure 6.13: Cooling fluid streamlines near the end-wall ribs.

For the end-wall region with ribs, the heat load introduced by the additional surface area needs to be taken into account. To fully assess the performance of the ribbed structure, it may be more sensible to compare the total heat load rather than heat flux. A Net Heat Load Reduction (NHLR) can be expressed as,

$$NHLR = 1 - \frac{\int_{A_f} h_f (T_{ad} - T_w) dA_f}{\int_{A_0} h_0 (T_\infty - T_w) dA_0} = 1 - \frac{\int_{A_f} h_f \left({T_{ad}}/{T_w} - 1\right) dA_f}{\int_{A_0} h_0 \left({T_\infty}/{T_w} - 1\right) dA_0} \quad (6.10)$$

where the temperature ratios T_∞/T_w, and T_{ad}/T_w can be replaced by typical values at engine conditions. The NHLR definition can be further simplified as follows:

$$NHLR = 1 - \frac{\int_{A_f} h_f (1 - \eta\varphi) dA_f}{\int_{A_0} h_0 dA_0} \quad (6.11)$$

Distributions of NHLR along the duct passage is shown in Fig.6.14. As expected, the case with larger rib height (h/δ=0.25) does not show an overall improvement in heat load reduction due to some local poor coolant coverage. However, the case with reduced rib height (h/δ=0.15) gives consistent improvement for all the duct locations. An overall 11% improvement in NHLR is obtained.
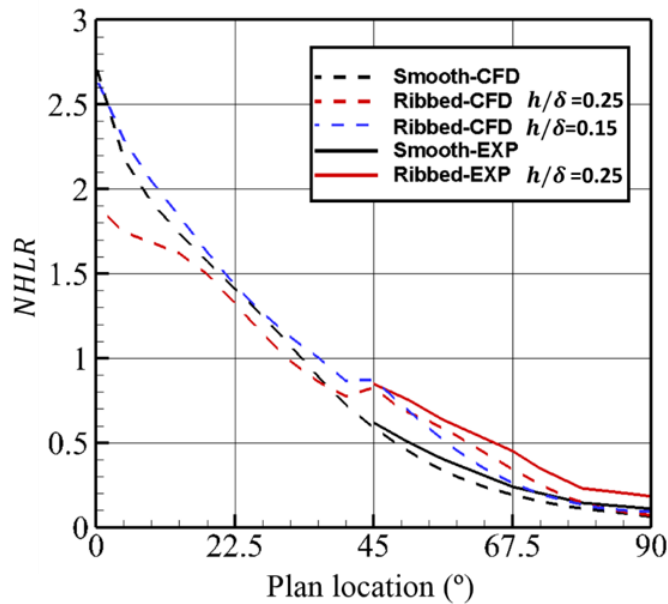
Figure 6.14: Distributions of Net Heat Load Reduction along the duct passage.

In terms of practical design optimization strategy, the surface feature should be determined according to the incoming flow boundary layer characteristics, the purge air blowing ratio, blade loading, etc. Rib structure with variable heights along the flow passage should be able to achieve better performance. Instead of the protrusion, groove structure could also be implemented. It is exciting to know that such additional design flexibility from the aerothermal perspective are being made feasible by the advances in Additive Manufacturing.

6.2 Cooling Performance in a Turbine Cascade

6.2.1 Purge Air Flow Structure

The vortices developing in the turbine blade passage with and without ribbed surface structure are visualized through λ_2, as shown in Fig. 6.15. The end-wall surface is colored by the film cooling effectiveness η. For the smooth surface (Fig. 6.15a), the low momentum boundary layer fluids separate at the blade leading edge

and develop into the horseshoe vortex, which splits into two legs. One leg of the horseshoe vortex develops over the blade suction surface and finally joins the passage vortex. The purge air injected through the rim seal is merged within the pressure side of the horseshoe vortex and swept to suction side quickly. This is consistent with the film cooling effectiveness contour on the end-wall surface. Figure 6.15b shows the horseshoe vortex is greatly modified by the ribbed surface. The strength of the suction side leg of the horseshoe vortex is much reduced, so as the passage vortex developed further downstream (discussed later).
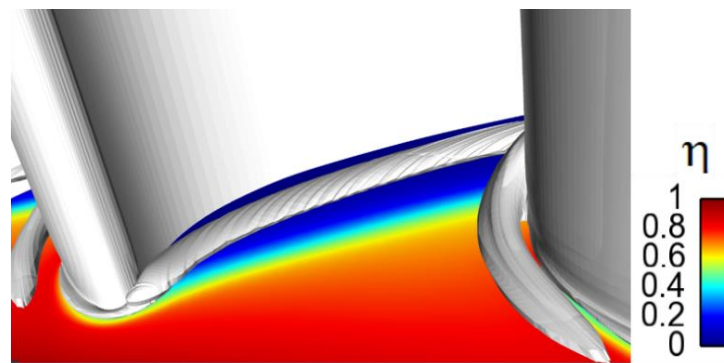
(a) Smooth surface
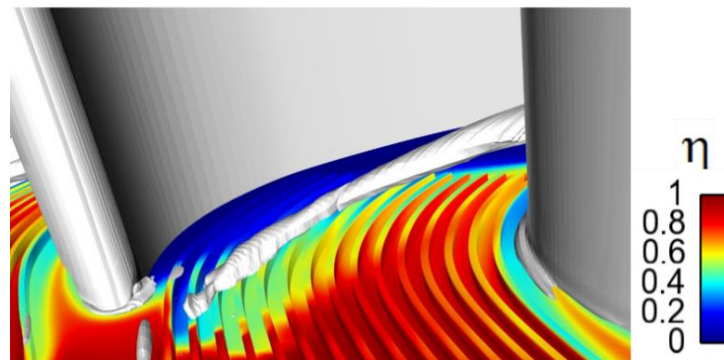
(b) Ribbed surface

Figure 6.15: Iso-surfaces of λ_2 for smooth and ribbed surface.

To visualize the coolant coverage over the end-wall, an iso-temperature surface with non-dimensional fluid temperature $\theta = 0.6$ is shown in Fig. 6.16. The value of θ is also defined as Equation 6.1. Lower θ value indicates a colder local fluid temperature, thus θ is also an indication of the purge air concentration. Figure 6.16a clearly shows the injected purge air is swept towards the blade suction side

due to the strong cross pressure gradient. With the addition of rib structures on the surface, the purge air cannot be immediately swept towards the suction side, instead, it follows the streamlined ribs, and remains close to the end-wall surface for a longer distance, resulting in a larger coverage over the end-wall.

(a) Smooth surface   (b) Ribbed surface
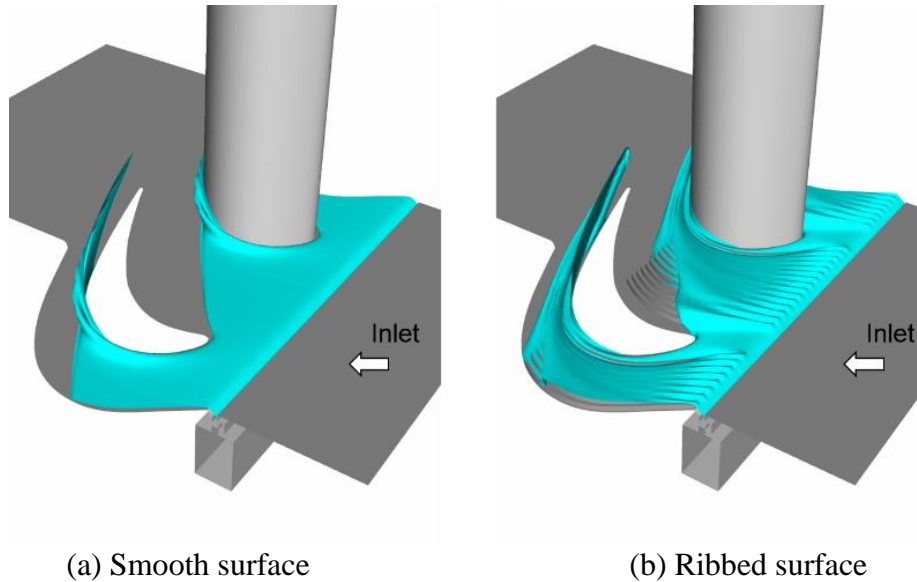
Figure 6.16: An iso-temperature surface with $\theta = 0.6$.

The distribution of non-dimensional fluid temperature θ within three cross-sections along the turbine cascade passage is shown in Fig. 6.17. The three cross-sectional planes are located at 20%, 50% and 70% chord from the leading edge. As revealed in Fig. 6.17, the low-temperature air tends to accumulate onto the suction side for both cases. At the 70% C_x plane of the smooth end-wall case, the cold air has been lifted off the wall and are contained in the passage vortex. For the ribbed surface case, most purge air concentration spreads wider in the pitchwise direction while stays closer to the end-wall and occupy the rib grooves at 20% and 50% C_x cross sections. Compared with the smooth case, the near wall temperature in ribs surface passage is much lower.

(a) Smooth surface   (b) Ribbed surface
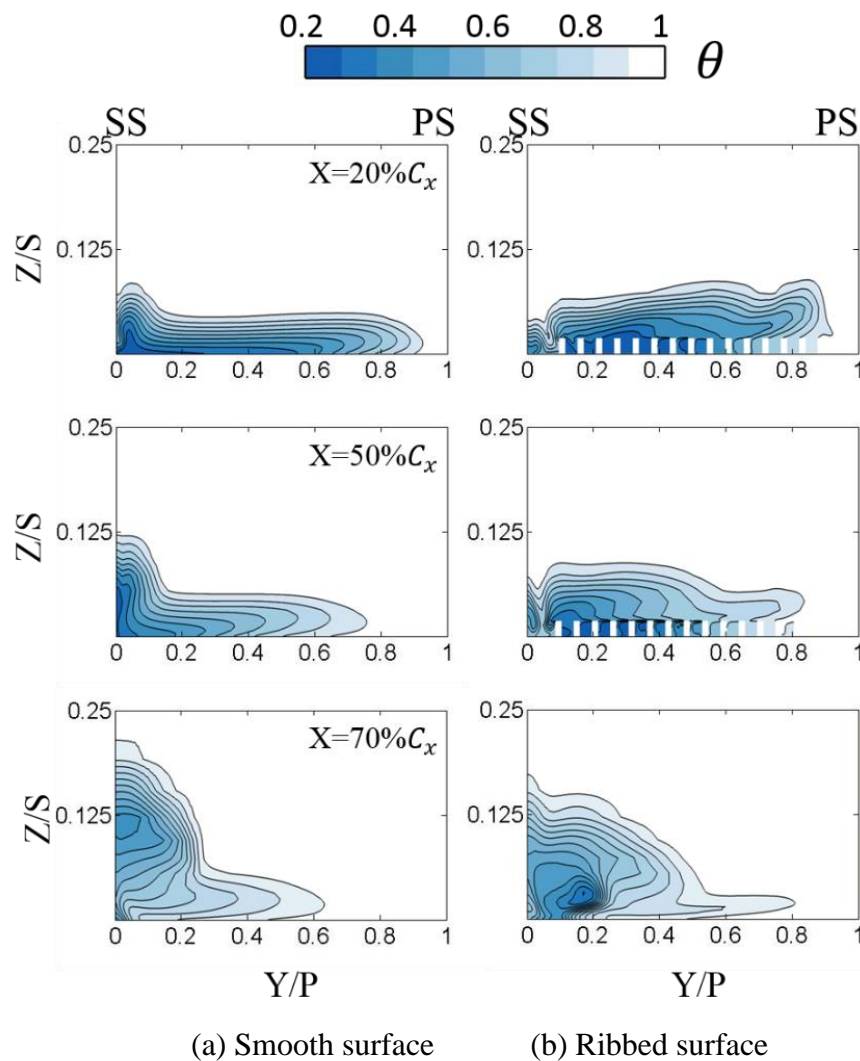
Figure 6.17: Non-dimensional temperature θ distributions at three cross sections.

The streamwise vorticity in the three cross planes at 20%, 50% and 70% C_x are used to reveal the evolution of the secondary flow. The streamwise vorticity is calculated from Equation 6.2. The streamwise vorticity is further non-dimensionalized by C_x/V_∞. The negative vorticity (red color) is associated with the secondary vortex, while the positive vorticity (blue color) represents the vortex with an opposite rotation.

(a) Smooth surface   (b) Ribbed surface
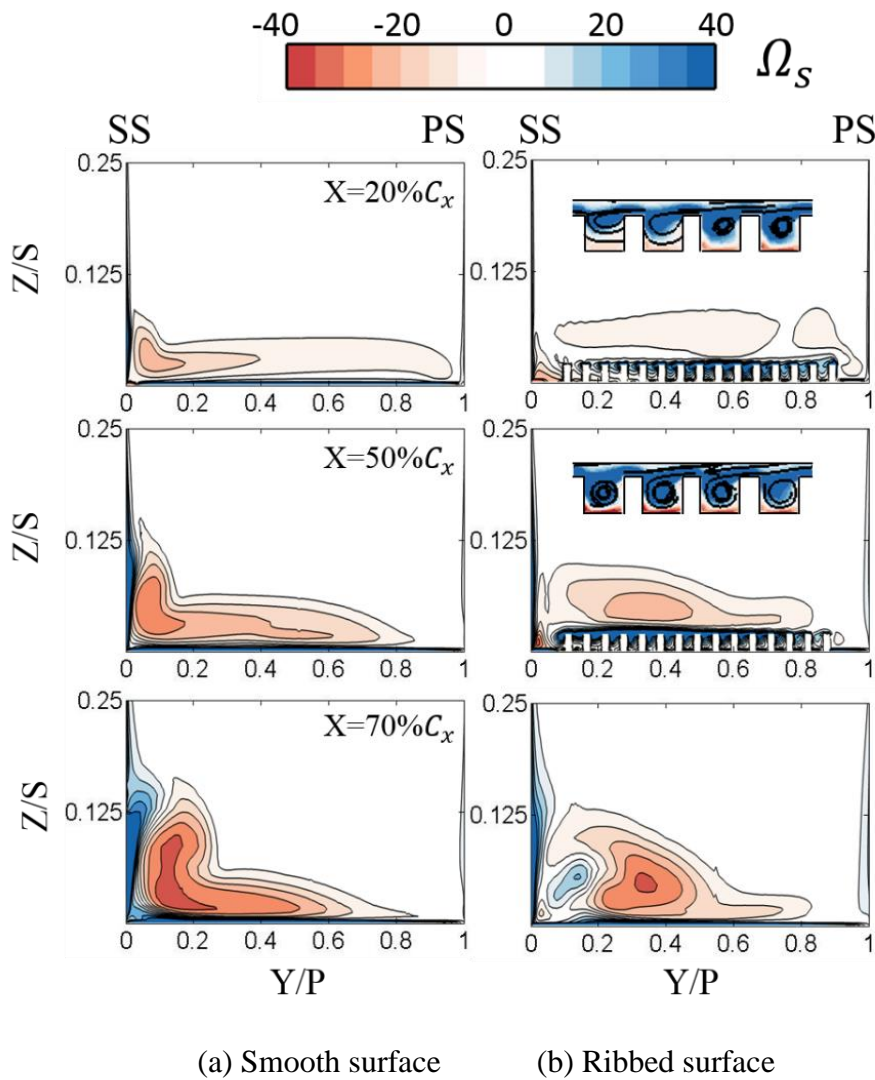
Figure 6.18: Streamwise vorticity distribution at three cross sections.

For the case of smooth end-wall, as the flow is turning, the passage vortex which has negative streamwise vorticity develops and moves quickly across the passage. It accumulates in the suction surface and end-wall corner at 70% C_x. While in the ribbed case, the strength of the passage vortex is largely reduced by the blockage effect of ribs. The ribs also introduce vorticity with an opposite sign, which has been revealed as vortices of a smaller scale than the passage vortex. Two zoomed in pictures are also shown in Fig. 6.18b to illustrate the detailed flow development over these ribs. The black lines indicate the secondary streamlines projected to the cross plane. Due to the occupation of the positive vorticity, the cross flow cannot follow

the ribs curvature well and an earlier lift-off of the streamlines can be observed. These flow structures are consistent and similar to previous findings by Miao et al. (2016).

(a) Smooth surface   (b) Ribbed surface
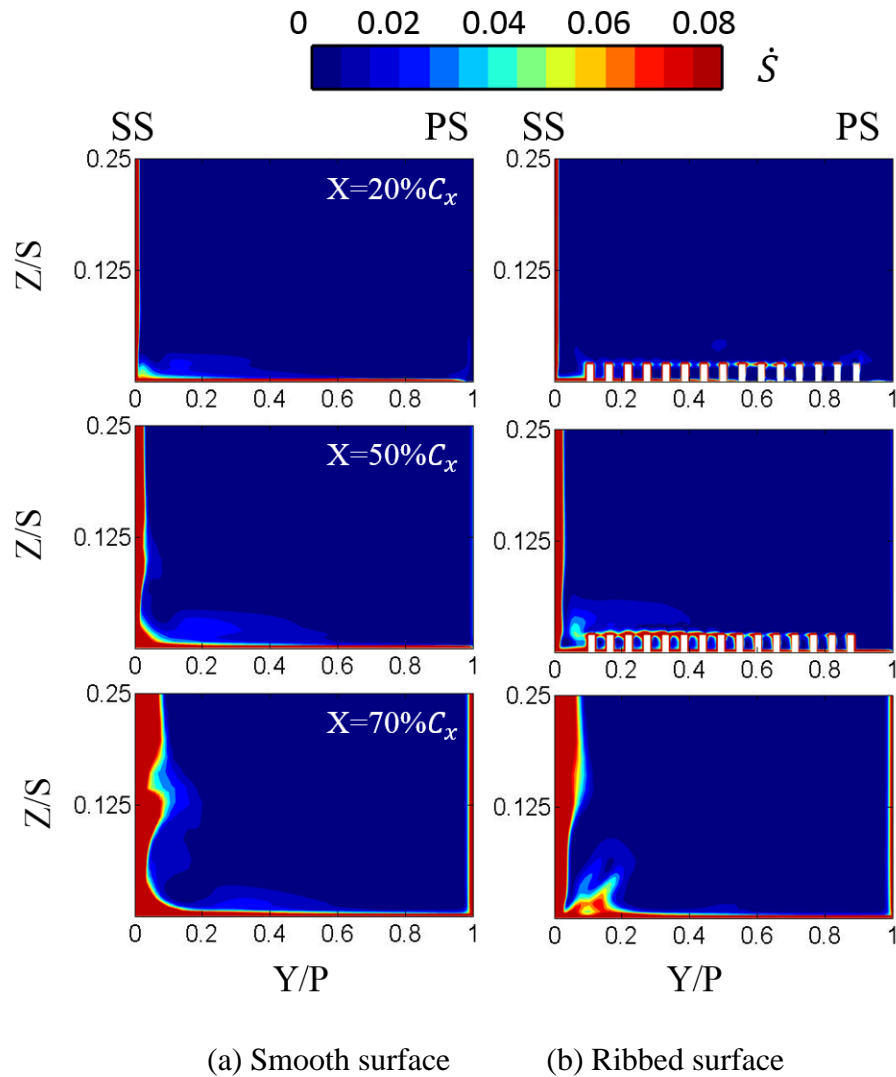
Figure 6.19: $\dot{S}$ distributions at three cross sections.

Dimensionless entropy generation rate per unit volume distributions at three cross sections along the turbine passage is shown in Fig.6.19. The entropy generation rate per unit volume is calculated based on Equation 2.19 and non-dimensionalised by dividing by $\rho_{out}V_{out}^3/C_xT_{out}$. For the smooth surface, the entropy generation rate associated with passage vortex increases when the vortex crosses the passage and rolls up near the suction side surface. The highest rate region can be seen on the suction side surface. For the ribbed surface, high entropy generation rate is produced

by the friction of ribs. When the purge air exits the rib grooves, a higher rate region occurs due to the mixing loss at 70% C_x.

   Figure 6.20 presents the distributions of aerodynamics loss coefficient at the exit plane of the blade passage. The aerodynamics loss coefficient is defined by Equation 6.3. The difference between smooth and ribbed cases in aerodynamic loss is within 2%, which is negligible considering the numerical accuracy of the CFD calculations. The further experimental investigation is needed to confirm this numerical observation.
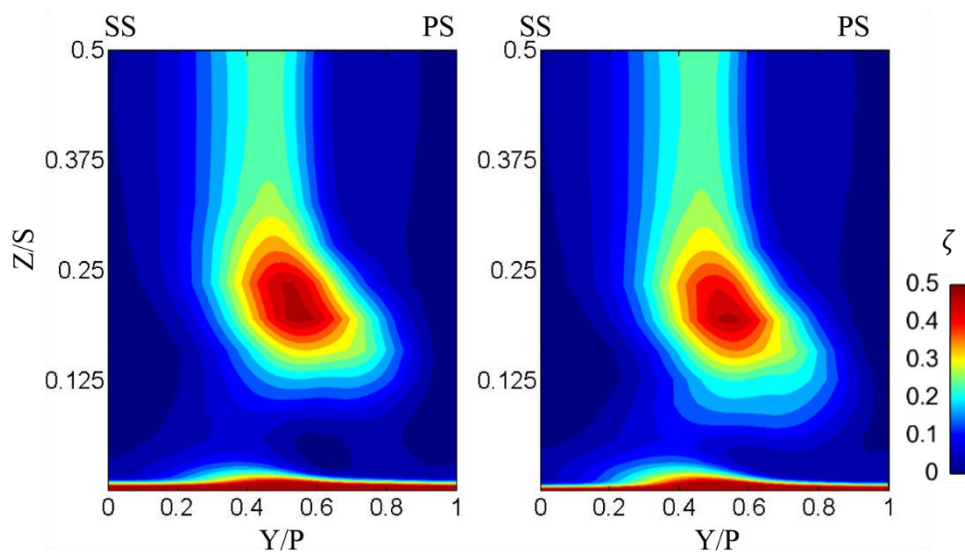
(a) Smooth surface   (b) Ribbed surface

Figure 6.20: Distributions of ζ at the exit plane.

6.2.2   Cooling Effectiveness

   Film cooling effectiveness η measured on the smooth surface and rib-surface are compared in Fig. 6.21. The film cooling effectiveness is calculated from Equation 6.4. It should be mentioned that measurement results right on the ribbed surfaces are not as accurate due to the emissivity issue of infrared measurement over the roughened surface structure (with varying view factor). However, the qualitative trend could be recognized.

(a) Smooth surface   (b) Ribbed surface
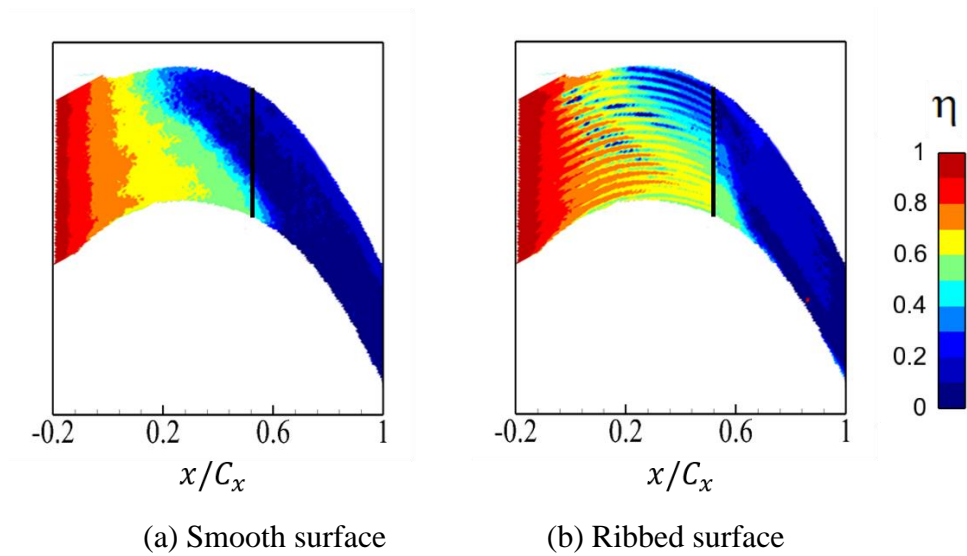
Figure 6.21: Distributions of film cooling effectiveness. (experimental data)

(a) Smooth surface   (b) Ribbed surface
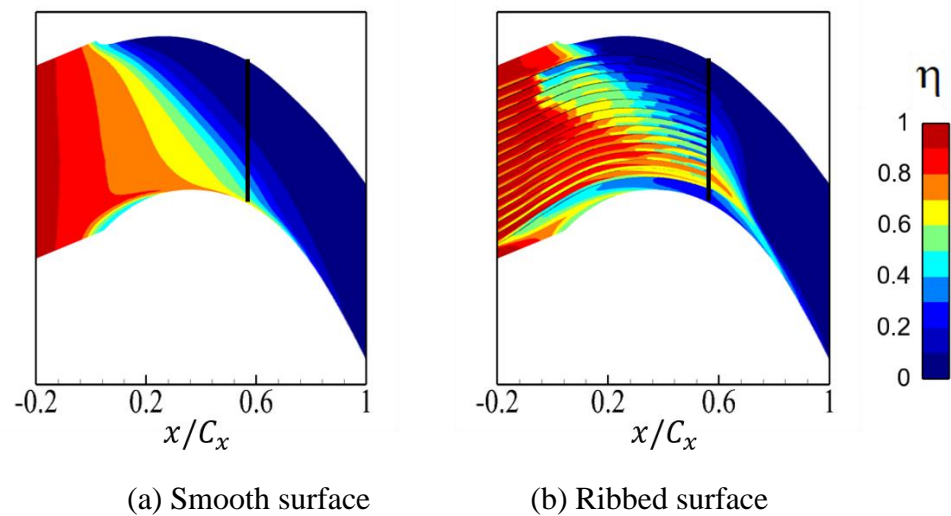
Figure 6.22: Distributions of film cooling effectiveness. (CFD results)

For the smooth end-wall case shown in Fig. 6.21a, the film cooling effectiveness is larger than 0.8 close to the exit of the rim seal, while the cooling effectiveness drops quickly near the blade pressure side. Due to the lateral migration of the horse-shoe vortex and passage vortex, the rear part of the blade passage does not receive any cooling benefit from the purge air injection.

Adding small ribs to the end-wall surface improves the film cooling effectiveness, as shown in Fig. 6.21b. Clearly, the cooling purge air is allowed to penetrate further downstream and provide a much large coverage area.

Figure 6.22 presents CFD results of the film cooling effectiveness. Consistently, a good qualitative overall agreement can be observed.
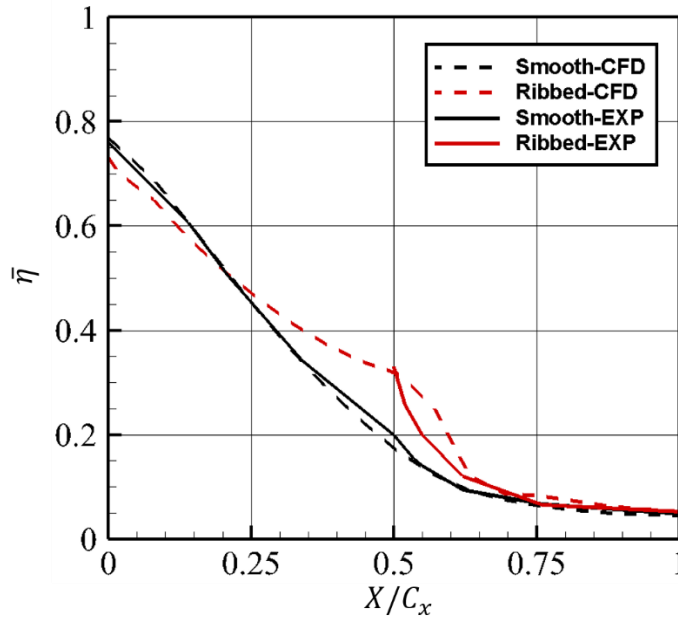
Figure 6.23: Pitch-wise averaged film cooling effectiveness $\overline{\eta}$ along the turbine passage for both experimental and CFD results.

The pitch-wise averaged cooling effectiveness along the axial direction for the smooth (black color) and ribbed surface (red color) is further illustrated in Fig. 6.23. The CFD result is shown as dash lines, while the experimental data is presented as solid lines. For the smooth surface, it can be observed that the cooling effectiveness value falls consistently from 0.76 to 0.05 along the turbine passage because the passage vortex and pressure side leg of the horseshoe vortex sweep the purge air from pressure side to suction side. As previously discussed, the engineered small-scale surface ribs can align and control the purge air cooling flow, more purge air can stay in the near wall region. Therefore, the value of cooling effectiveness for the ribbed surface is larger than the smooth surface. After 50% C_x, the $\overline{\eta}$ value decreases rapidly because the purge air is quickly swept to the suction side due to the cross pressure gradient when it exits the ribs grooves. The experimental data and CFD results

have the same trend in the region where test data is available.

6.2.3 Net Heat Flux Reduction (NHFR)

The Net Heat Flux Reduction (NHFR), which is combined outcome of the changes in film cooling effectiveness and heat transfer coefficient, is further examined next in Fig. 6.24 and Fig. 6.25. The NHFR is defined the same as Equation 6.8. φ is the non-dimensional metal temperature, which is dependent on the metal conductivity and internal cooling technology. For a typical operational film cooled turbine blade, a value of 1.6 is used based on the work of Sen et al. (1996).

For the end-wall region with ribs, the heat load introduced by the additional surface area needs to be taken into account. To fully assess the performance of the ribbed structure, a Net Heat Load Reduction (NHLR) is defined as Equation 6.10 and can be further simplified as Equation 6.11.

Due to the experimental errors near the small ribs and lack of information from the rib side walls, it is not possible to estimate and compare experimental NHLR values. NHLR data can only be assessed based CFD data discussed next.

Significant NHFR enhancement by ribbed surface can be observed both experimentally and numerically, as illustrated in Fig. 6.24 and Fig. 6.25. The improvement is less significant compared with the results previously reported in Section 6.1, which can be attributed to the limited effect of surface features on the horseshoe vortex. The overall Net Heat Load Reduction (NHLR) based on all the exposed surface area of the ribbed end-wall only has a marginal 2% improvement over the smooth case. Similar to the performance shown in Section 6.1, the RANS CFD results are less diffused than the measurement data. The complex interactions between the horseshoe vortex, passage vortex, and end-wall ribs need to be better resolved by CFD solvers with high-fidelity (such as LES).

(a) Smooth surface   (b) Ribbed surface
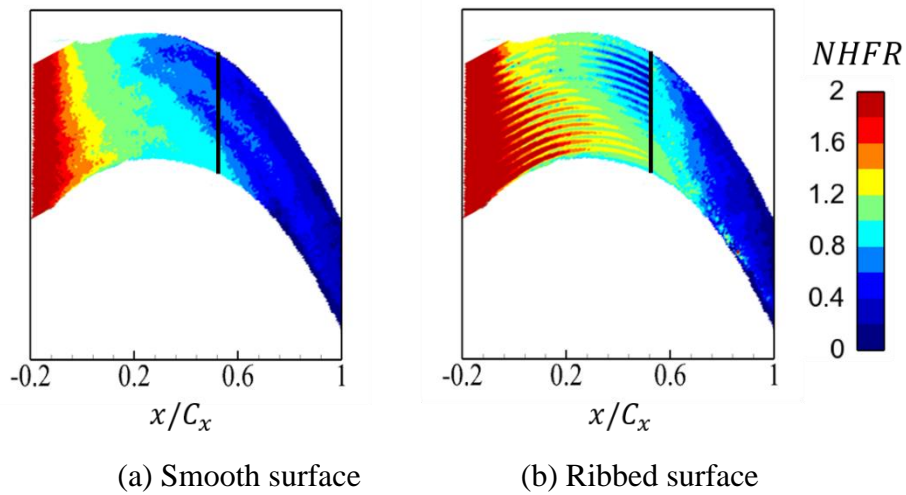
Figure 6.24: Distribution of NHFR. (**experimental** data)

(a) Smooth surface   (b) Ribbed surface
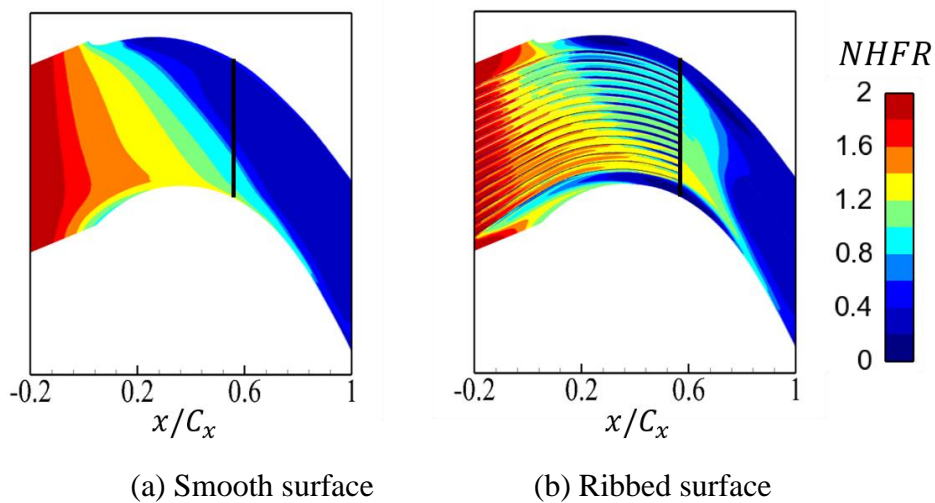
Figure 6.25: Distribution of NHFR. (**CFD** results)

6.2.4 Purge Air Cooling Enhancement in High-speed Condition

In the previous study, the engineered surface structure has been proved to be effective in reducing the passage vortex and providing a larger area of coolant cov-

erage in low-speed condition. In order to investigate the purge air cooling enhancement under real engine operating condition, high-speed flow cases are numerically studied. The computational domain and purge air blowing ratio are the same as that in low-speed cases. The cascade inlet Mach number and Reynolds number are 0.2 and 3.06×10^5, which are representative of real engine conditions. The exit Mach number and Reynolds number are 0.6 and 7.42×10^5. The inlet turbulence intensity is approximately 1%.

(a) Smooth surface　　　(b) Ribbed surface
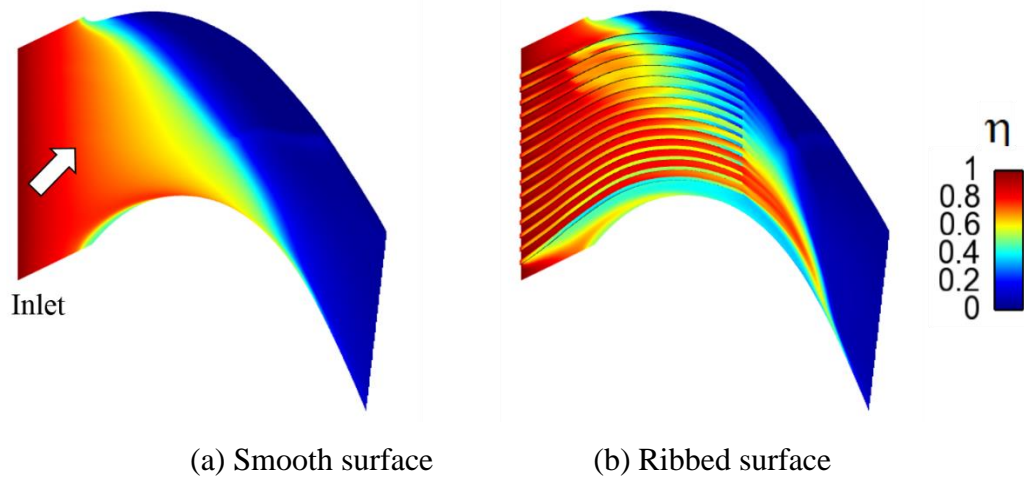
Figure 6.26: Distributions of film cooling effectiveness in high-speed condition. (CFD results)

Film cooling effectiveness η is calculated by using Equation 6.4 based on numerical simulation. Figure 6.26 presents the distribution of η for both the smooth surface and rib-surface. Similar with the result in low-speed condition, the purge is quickly swept from pressure side to suction side of the blade. Although the film cooling effectiveness approaches the ideal value and has good unity at the exit of the slot, the η quickly decreases more than half of the passage is left protected. With the addition of ribs on the end-wall surface, the purge air can travel to the further to the downstream and protect more area of blade passage. Thus the film cooling effectiveness is increased significantly. Compared with the film cooling effectiveness distribution in low-speed condition (see Fig. 6.22), the end-wall ribs can provide better performance in high-speed.

Figure 6.27 shows distributions of pitch-wise averaged cooling effectiveness along the axial direction. It can be observed that the $\overline{\eta}$ is declined rapidly from the

blade leading edge to 50% C_x due to the migration of passage vortex and pressure side of horseshoe vortex, while the value of averaged film cooling effectiveness decreases gradually because more purge air is aligned by the end-wall ribs. The purge air is quickly migrated to the suction side of the passage by strong cross pressure gradient when it exits from the rib grooves at 50% C_x, thus the $\bar{\eta}$ for ribbed surface drops and has the same value after 80% C_x.
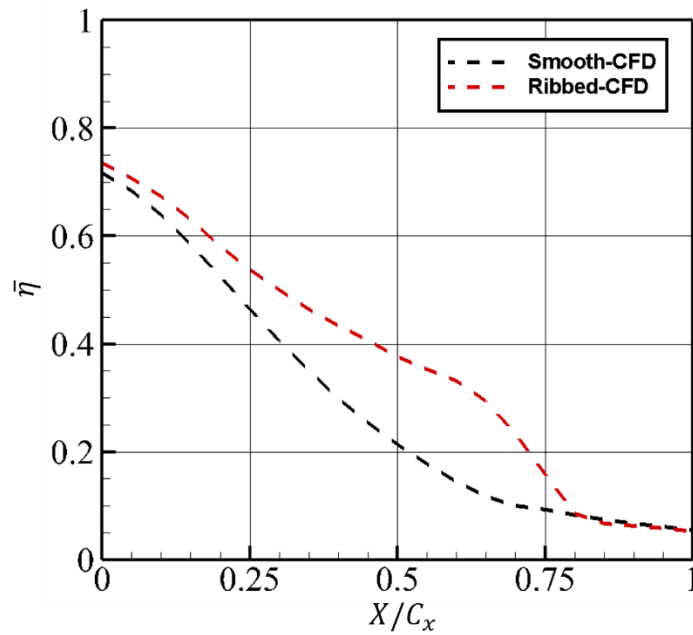
Figure 6.27: Distribution of pitch-wise averaged cooling effectiveness in high-speed condition.

(a) Smooth surface   (b) Ribbed surface
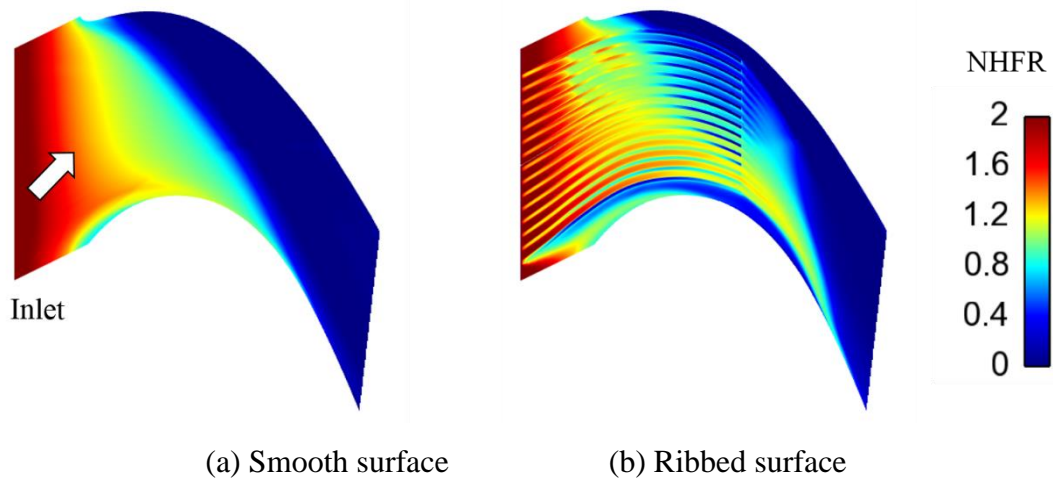
Figure 6.28: Distribution of NHFR in high-speed condition. (**CFD** results)

The numerical predictions of net heat flux reduction on the smooth and ribbed surface is shown in Fig. 6.28. The NHFR is calculated based on Equation 6.8. The blue color represents the region with low heat flux reduction, while the red color corresponds to the region benefiting from purge air cooling. It can be seen that the NHFR is positive in regions covered by purge air. Similar to the trend in low-speed condition, adding end-wall ribs can largely enhance the NHFR.

6.3 Summary

In this chapter, the novel flow control technique is used for purge air cooling enhancement. The engineered small-scale surface ribs can also be envisaged as the devices for controlling and aligning the purge air cooling flow. The purge air cooling is investigated in a simplified duct and linear turbine cascade flow through closely coupled experimental and numerical studies. Studying the simplified flow model is useful in obtaining the fundamental physical understanding of the working mechanism of this flow control concept without considering the complex horseshoe vortex developed in the turbine system. The transient thermal measurement is taken in a low-speed wind tunnel. Further analysis of the detailed flow structure is carried out by using a commercial CFD code.

For the 90-degree duct, the CFD analysis reveals that a ribbed end-wall can guide the purge air flow further to cover the more end-wall surface. The secondary flow vortex can be reduced by the ribs blockage for cross-flow migration and the vortices generated in the rib grooves maintain the purge air attached to the end-wall. The film cooling effectiveness and Net Heat Flux Reduction (NHFR) obtained in transient thermal measurement consistently validate the numerical findings. With the addition of engineered surface structure, the film cooling effectiveness is significantly increased. An over 50% increase in NHFR has been achieved in the present study without efforts on design optimization.

Similar to the findings from the simplified turning duct study, it has been consistently observed that the ribs are able to reduce the horseshoe vortex and passage vortex and provide favorable alignment to the cooling flow. The purge air flow is

found to cover a larger area over the turbine end-wall. The CFD study indicates that the additional aerodynamic penalty introduced by the small ribs is negligible. The further experimental evidence is needed to validate this numerical finding. The film cooling effectiveness and NHFR is measured by using the transient thermal measurement technique. The numerical results have a good agreement with the EXP data. Both results show that the ribbed surface can enhance the film cooling effectiveness and NHFR significantly.

Finally, the effect of the engineered surface structure on purge air cooling enhancement is studied in high-speed flow to represent the real engine operating condition. The film cooling effectiveness and NHFR on both smooth and ribbed surface are compared qualitatively and quantitatively. Similar with the results in a low-speed condition, the ribs can largely increase the film cooling effectiveness and NHFR.

This novel engineered surface structure concept proposed in this chapter provides a large improved design space and new research dimension in turbine end-wall cooling.

Chapter 7

Summary and Conclusions

This chapter reviews the work performed in this thesis, as well as the approach taken to address the research objectives in Section 1.2. The key findings of the research are summarized, and suggestions for future work are given in the followed sections.

7.1   Summary

The present thesis investigates the turbine end-wall aero-thermal management with engineered surface structure. The research is motivated by the latest advances in manufacturing techniques, especially Additive Manufacturing (AM). The engineered surface structure was employed on the end-wall to study the effect on turbine aerothermal management.

The PIV and transient heat transfer experimental facility and procedure were

introduced in detail. All experimental measurements were performed in the low-speed wind tunnel which has the capacity to maintain the inlet velocity at 20m/s. A transparent 90-degree turning duct was first designed for both PIV and heat transfer experiment to simulate the turbine passage without introducing horseshoe vortex. Then the engineered surface structure was applied to a linear turbine cascade for transient thermal measurements. The test section consists of four blades and three flow passages and good flow periodicity was checked. The TSI Nd: YAG laser and high-speed camera were used in the PIV experiment to obtain the exit flow field. A heater mesh provided a step mainstream temperature change at the inlet while a vortex tube generated the cold purge air through additional purge air supply facility to simulate the purge air injection through the rim seal. For both test sections, the detachable end-wall surface structure was manufactured by using the 3D printing technique and was easy to change. A pitot probe and a boundary layer probe were used to measure the total pressure, static pressure and boundary layer thickness respectively. The pressure and temperature signals were instrumented by the National Instruments (NI) Data Acquisition (DAQ) system.

The principle of PIV and transient thermal measurement technique was described. In PIV experiment, two images were shot in a short period of time, the distance of individual particles traveled within this time was calculated by analyzing these two images. Thus the velocity field was obtained from the known time difference and the measured displacement. The transient thermal measurement assumes that the solid can be considered as semi-infinite, one-dimensional conduction. Therefore, end-wall surface heat flux can be reconstructed from temperature traces, the heat transfer coefficient and adiabatic wall temperature then obtained from linear regression. Linear regression uncertainty and repeatability analysis were also discussed.

The details of the computational fluid dynamics (CFD) simulations were introduced, including the computational domain, solver and turbulence model selection, grid independence and code validation. Boundary condition setting was presented in detail, the inlet velocity profile was the same as that measured in the experiment and programmed in UDF code. Steady Reynolds-Averaged Navier-Stokes (RANS) simulation was performed by using ANSYS FLUENT software. The k-ω shear stress

transport (SST) turbulence model was selected to model the turbulence. Three different density meshes were checked to study the grid independence. The simulation strategy was then validated through the comparison with an existing experimental data.

End-wall secondary flow control by using the engineered surface structure was studied in a 90-degree turning duct first. This simplified duct can be considered as a basic model for the turbine passage without introducing the horseshoe vortex. Different fence number and fence structure were studied. The working principle of the engineered surface structure is revealed through detailed analysis. Then the concept was applied to a linear turbine cascade. Detailed flow physics were investigated by comparing the smooth surface and ribbed surface.

The novel flow control technique was then used for purge air cooling enhancement. The engineered surface structures were added to the end-wall of a 90-degree turning duct to investigate its effect on purge air cooling performance through combined CFD and experimental study. Purge air flow structure and the interaction between secondary flow and purge air was analyzed from CFD results. The film cooling effectiveness and NHFR obtained in transient thermal measurement for both smooth and ribbed surface were compared and validated the numerical results. The fundamental working mechanism and cooling performance in a 90-degree turning duct were presented.

Finally, the engineered surface structures concept was applied in a more realistic linear turbine cascade. Purge air flow structure and end-wall heat transfer in low-speed condition were analyzed. A transient thermal experiment was conducted to validate the CFD results. The numerical study on purge air cooling enhancement by using the engineered surface structure in high-speed condition was performed. The film cooling effectiveness and NHFR were further discussed.

7.2   Conclusions

The present section summarizes the significant conclusions of the current thesis.

One of the main aims of this thesis is to understand the effect of engineered surface structure on secondary flow control. In order to do this, a 90-degree turning

duct is first selected to simulate the turbine cascade passage without considering the complex horseshoe vortex. Then the engineered end-wall surface structure is applied to a linear turbine cascade for secondary flow reduction study.

The significant contributions of the work are summarized below:

- Arrays of rib and wavy grooves are found to be more effective in alleviating passage vortex as well as flow over-turning. The strength of the passage vortex can be largely reduced by multiple engineered surface structure.

- The groove array is shown to be slightly less efficient than the rib array due to the earlier formation of the vortex filaments induced by the wavy grooves.

- The PIV measurements conducted in this research qualitatively confirm the numerical finding. The multiple rib and wavy grooves can effectively reduce the streamwise vorticity thus weaken the strength of the passage vortex,

- The engineered surface structure introduces additional loss penalty. Friction and the mixing loss from the small-scale vortices near ribs will accumulate and be convected downstream through the passage. The beneficial effect of secondary flow control needs to overcome these unavoidable side effects.

Another major objective of this thesis is to investigate the engineered surface structure effect on purge air cooling enhancement. Similar with the research methodology in the study of secondary flow control, a simplified duct is firstly used to improve the understanding of the fundamental working mechanism, then the novel concept is applied to a turbine cascade environment. The key findings of this study are concluded below:

- The ribs employed on the end-wall of 90-degree turning duct and turbine cascade can guide the purge air flow further to cover a larger area over the end-wall and keep the purge air attached to the end-wall surface.

- The secondary flow vortex can be reduced by the ribs blockage for cross-flow migration, while the additional aerodynamic penalty introduced by the small ribs is negligible.

- Film cooling effectiveness and net heat flux reduction are significantly improved in both experimental and CFD results with the addition of engineered surface structure.

- The overall improvement in Net Heat Load Reduction for 90-degree turning duct and turbine cascade is 11% and 2% respectively.

In summary, the current research has achieved the primary objective of the thesis by enhancing the understanding of engineered surface structure effect on secondary flow control and purge air cooling performance.

7.3   Future Work

In addition to the contributions of the present thesis, the current research has identified a number of possible directions for future work. Several recommendations for future work are summarized in this section.

Increasing the strength of secondary flow can obtain a larger loss reduction. As discussed in Section 2.2, secondary flow strength is largely affected by many cascade characteristics, such as Reynolds number, turning angle, blade loading, and blade aspect ratio. The cases considered in the present thesis has a high aspect ratio and low Reynolds number, the secondary losses accounted for a small proportion of total loss. Therefore, higher Reynolds number flows is recommended for the future work.

The present experiments were completed in a low-speed testing facility which cannot represent the real engine operating condition. In order to study the effect of engineered surface structure on secondary flow control and purge air cooling enhancement in high-speed condition, a transonic optical linear cascade has been manufactured. Detailed PIV and transient thermal measurements should be performed in a high-speed condition.

Steady Reynolds-Averaged Navier-Stokes (RANS) simulation was performed in the present study due to the limitation of computational capacity. Small-scale vortices in the rib groves can be predicted accurately by using Large Eddy Simulation (LES) or Direct Numerical Simulation (DNS) approach in the future work.

There will be a large design optimization space for the engineered surface structure. Present results show that employing engineered surface structure on turbine end-wall is an effective method to reduce secondary flow and secondary flow loss; it should be noticed that additional losses are also introduced by the small-scale vortices in the end-wall rib grooves. The flow structure in the near wall region can be changed by different geometries and lengths of ribs. The detailed geometry should be determined according to the inlet boundary layer thickness, the turbulence intensity, blade loading and Reynolds number. Therefore, further design optimization should be considered in the future work.

Bibliography

ADRIAN, R. 1986. Multi-point optical measurements of simultaneous vectors in unsteady flow—a review. *International journal of heat and fluid flow,* 7**,** 127-145.

ADRIAN, R. J. 1991. Particle-imaging techniques for experimental fluid mechanics. *Annual review of fluid mechanics,* 23**,** 261-304.

ADRIAN, R. J. 2005. Twenty years of particle image velocimetry. *Experiments in fluids,* 39**,** 159-169.

BARIGOZZI, G., BENZONI, G., FRANCHINI, G. & PERDICHIZZI, A. 2006. Fan-shaped hole effects on the aero-thermal performance of a film-cooled endwall. *Journal of turbomachinery,* 128**,** 43-52.

BARIGOZZI, G., FRANCHINI, G., PERDICHIZZI, A. & QUATTRORE, M. 2010. Endwall Film Cooling Effects on Secondary Flows in a Contoured Endwall Nozzle Vane. *Journal of Turbomachinery,* 132**,** 041005.

BARIO, F., LEBOEUF, F., ONVANI, A. & SEDDINI, A. Aerodynamics of Cooling Jets Introduced in the Secondary Flow of a Low Speed Turbine Cascade. ASME 1989 International Gas Turbine and Aeroengine Congress and Exposition, 1989. American Society of Mechanical Engineers, V001T01A078-V001T01A078.

BECZ, S., MAJEWSKI, M. & LANGSTON, L. Leading edge modification effects on turbine cascade endwall loss. ASME Turbo Expo 2003, collocated with the 2003 International Joint Power Generation Conference, 2003. American Society of Mechanical Engineers, 359-367.

BECZ, S., MAJEWSKI, M. S. & LANGSTON, L. S. An experimental investigation of contoured leading edges for secondary flow loss reduction. ASME Turbo Expo

150

2004: Power for Land, Sea, and Air, 2004. American Society of Mechanical Engineers, 1407-1415.

BERGER, S., TALBOT, L. & YAO, L. 1983. Flow in curved pipes. *Annual review of fluid mechanics,* 15**,** 461-512.

BERGMAN, T. L., LAVINE, A. S., INCROPERA, F. P. & DEWITT, D. P. 2011. Fundamentals of heat and mass transfer. John Wiley & Sons Hoboken, NJ.

BIKAS, H., STAVROPOULOS, P. & CHRYSSOLOURIS, G. 2016. Additive manufacturing methods and modelling approaches: a critical review. *The International Journal of Advanced Manufacturing Technology,* 83**,** 389-405.

BLAIR, M. An experimental study of heat transfer and film cooling on large-scale turbine endwalls. ASME 1974 International Gas Turbine Conference and Products Show, 1974. American Society of Mechanical Engineers, V01AT01A033-V01AT01A033.

BLANCKAERT, K. & DE VRIEND, H. J. 2004. Secondary flow in sharp open-channel bends. *Journal of Fluid Mechanics,* 498**,** 353-380.

BOGARD, D. G. & THOLE, K. A. 2006. Gas turbine film cooling. *Journal of propulsion and power,* 22**,** 249-270.

BOLETIS, E. 1985. Effects of Tip Endwall Contouring on the Three-Dimensional Flow Field in an Annular Turbine Nozzle Guide Vane: Part 1—Experimental Investigation. *Journal of engineering for Gas Turbines and Power,* 107**,** 983-990.

BRENNAN, G., HARVEY, N., ROSE, M., FOMISON, N. & TAYLOR, M. Improving the Efficiency of the Trent 500 HP Turbine Using Non-Axisymmetric End Walls: Part 1—Turbine Design. ASME Turbo Expo 2001: Power for Land, Sea, and Air, 2001. American Society of Mechanical Engineers, V001T03A066-V001T03A066.

BRUUN, H. H. 1996. Hot-wire anemometry: principles and signal analysis. IOP Publishing.

BUCHHAVE, P. 1992. Particle image velocimetry—status and trends. *Experimental Thermal and Fluid Science,* 5**,** 586-604.

BUNKER, R., METZGER, D. & WITTIG, S. 1992a. Local Heat Transfer in Turbine Disk Cavities: Part I—Rotor and Stator Cooling With Hub Injection of Coolant. *Journal of turbomachinery,* 114**,** 211-220.

BUNKER, R., METZGER, D. & WITTIG, S. 1992b. Local Heat Transfer in Turbine Disk Cavities: Part II—Rotor Cooling With Radial Location Injection of Coolant. *Journal of turbomachinery,* 114**,** 221-228.

BURD, S. W., SATTERNESS, C. J. & SIMON, T. W. Effects of Slot Bleed Injection Over a Contoured End Wall on Nozzle Guide Vane Cooling Performance: Part II— Thermal Measurements. ASME Turbo Expo 2000: Power for Land, Sea, and Air,

2000. American Society of Mechanical Engineers, V003T01A008-V003T01A008.

BURD, S. W. & SIMON, T. W. Effects of Slot Bleed Injection Over a Contoured Endwall on Nozzle Guide Vane Cooling Performance: Part I—Flow Field Measurements. ASME Turbo Expo 2000: Power for Land, Sea, and Air, 2000a. American Society of Mechanical Engineers, V003T01A007-V003T01A007.

BURD, S. W. & SIMON, T. W. 2000b. Flow measurements in a nozzle guide vane passage with a low aspect ratio and endwall contouring. *Journal of turbomachinery,* 122**,** 659-666.

CAMCI, C. & RIZZO, D. H. 2002. Secondary flow and forced convection heat transfer near endwall boundary layer fences in a 90 turning duct. *International Journal of Heat and Mass Transfer,* 45**,** 831-843.

CARDWELL, N., SUNDARAM, N. & THOLE, K. 2007. The effects of varying the combustor-turbine gap. *Journal of Turbomachinery,* 129**,** 756-764.

CARTER, A. 1948. Three-dimensional-flow theories for axial compressors and turbines. *Proceedings of the Institution of Mechanical Engineers,* 159**,** 255-268.

CENGEL, Y. A. & BOLES, M. A. 2002. Thermodynamics: an engineering approach. *Sea,* 1000**,** 8862.

CHO, J., KIM, K., KIM, J. & JEONG, E. 2011. Controlling the secondary flows near endwall boundary layer fences in a 90° turning duct using approximate optimization method. *Journal of mechanical science and technology,* 25**,** 2025.

CHUNG, J. & SIMON, T. Effectiveness of the gas turbine endwall fences in secondary flow control at elevated freestream turbulence levels. ASME 1993 International Gas Turbine and Aeroengine Congress and Exposition, 1993. American Society of Mechanical Engineers, V001T03A019-V001T03A019.

CHUNG, J., SIMON, T. & BUDDHAVARAPU, J. Three-dimensional flow near the blade/endwall junction of a gas turbine: application of a boundary layer fence. ASME 1991 International Gas Turbine and Aeroengine Congress and Exposition, 1991. American Society of Mechanical Engineers, V004T09A008-V004T09A008.

CHYU, M. K. 2001. Heat transfer near turbine nozzle endwall. *Annals of the New York Academy of Sciences,* 934**,** 27-36.

COLBAN, W., THOLE, K. & ZESS, G. Combustor Turbine Interface Studies: Part 1—Endwall Effectiveness Measurements. ASME Turbo Expo 2002: Power for Land, Sea, and Air, 2002. American Society of Mechanical Engineers, 993-1001.

CUMPSTY, N. & HEYES, A. 2015. *Jet propulsion*, Cambridge University Press.

DANNHAUER, A. Analysis of Cooling Effectiveness and Heat Transfer Variations on the

152

End Wall of a Nozzle Guide Vane Caused by Turbine Leakage Flows. ASME Turbo Expo 2008: Power for Land, Sea, and Air, 2008. American Society of Mechanical Engineers, 543-552.

DE LA ROSA BLANCO, E., HODSON, H. & VAZQUEZ, R. 2009. Effect of the leakage flows and the upstream platform geometry on the endwall flows of a turbine cascade. *Journal of turbomachinery,* 131**,** 011004.

DEICH, M., ZARYANKIN, A., FILLIPOV, G. & ZATSEPIN, M. 1960. Method of increasing the efficiency of turbine stages with short blades. *Teploenergetika,* 2**,** 240-254.

DENKENA, B., KÖHLER, J. & WANG, B. 2010. Manufacturing of functional riblet structures by profile grinding. *CIRP Journal of Manufacturing Science and Technology,* 3**,** 14-26.

DÉNOS, R. & PANIAGUA, G. Influence of the Hub Endwall Cavity Flow on the Time-Averaged and Time-Resolved Aero-Thermodynamics of an Axial HP Turbine Stage. ASME Turbo Expo 2002: Power for Land, Sea, and Air, 2002. American Society of Mechanical Engineers, 207-217.

DENTON, J. 1993. Loss Mechanisms in Turbomachines. *Journal of Turbomachinery,* 115**,** 621.

DENTON, J. & CUMPSTY, N. 1987. Loss Mechanisms in Turbomachines, ImechE Paper, No. *C260/87.*

DENTON, J. & PULLAN, G. A numerical investigation into the sources of endwall loss in axial flow turbines. ASME Turbo Expo 2012: Turbine Technical Conference and Exposition, 2012. American Society of Mechanical Engineers, 1417-1430.

DEVORE, J. L. 2015. *Probability and Statistics for Engineering and the Sciences*, Cengage Learning.

DIXON, S. L. & HALL, C. 2010. *Fluid mechanics and thermodynamics of turbomachinery*, Butterworth-Heinemann.

DOOLAN, C., COTON, F. & GALBRAITH, R. Measurement of three-dimensional vortices using a hot wire anemometer. 30th Fluid Dynamics Conference, 1999. 3810.

DOSSENA, V., PERDICHIZZI, A. & SAVINI, M. 1999. The influence of endwall contouring on the performance of a turbine nozzle guide vane. *Journal of Turbomachinery,* 121**,** 200-208.

DUDDERAR, T., MEYNART, R. & SIMPKINS, P. 1988. Full-field laser metrology for fluid velocity measurement. *Optics and Lasers in Engineering,* 9**,** 163-199.

ECKERLE, W. A. & LANGSTON, L. Horseshoe vortex formation around a cylinder.

ASME 1986 International Gas Turbine Conference and Exhibit, 1986. American Society of Mechanical Engineers, V001T01A109-V001T01A109.

FLIR SYSTEMS: USER'S MANUAL - FLIR A3xx/A6xx sc series, 2012.

FRIEDRICHS, S., HODSON, H. & DAWES, W. Distribution of film-cooling effectiveness on a turbine endwall measured using the ammonia and diazo technique. ASME 1995 International Gas Turbine and Aeroengine Congress and Exposition, 1995. American Society of Mechanical Engineers, V004T09A001-V004T09A001.

FRIEDRICHS, S., HODSON, H. & DAWES, W. 1997. Aerodynamic aspects of endwall film-cooling. *Journal of turbomachinery,* 119**,** 786-793.

FRIEDRICHS, S., HODSON, H. & DAWES, W. The design of an improved endwall film-cooling configuration. ASME 1998 International Gas Turbine and Aeroengine Congress and Exhibition, 1998. American Society of Mechanical Engineers, V004T09A082-V004T09A082.

GE AVIATION. 2001. "The GE90–world record holder", http://www.geaviation.com/engines/commercial/ge90/world_record_holder.html.

GE ENERGY. 2011. "Gas turbines – aeroderivative", product overview http://www.ge-energy.com/products_and_services/products/gas_turbines_aeroderivative/index.jsp.

GIRGIS, S., VLASIC, E., LAVOIE, J.-P. & MOUSTAPHA, S. The effect of secondary air injection on the performance of a transonic turbine stage. ASME Turbo Expo 2002: Power for Land, Sea, and Air, 2002. American Society of Mechanical Engineers, 147-158.

GOLDMAN, L. J. & MCLALLIN, K. L. 1977. Effect of endwall cooling on secondary flows in turbine stator vanes.

GOLDSTEIN, R. & SPORES, R. 1988. Turbulent transport on the endwall in the region between adjacent turbine blades. *Journal of Heat Transfer,* 110**,** 862-869.

GOLDSTEIN, R. J. 1971. Film cooling. *Advances in heat transfer.* Elsevier.

GOVARDHAN, M., RAJENDER, A. & UMANG, J. 2006. Effect of streamwise fences on secondary flows and losses in a two-dimensional turbine rotor cascade. *Journal of Thermal Science,* 15**,** 296-305.

GRANT, I. 1997. Particle image velocimetry: a review. *Proceedings of the Institution of Mechanical Engineers, Part C: Journal of Mechanical Engineering Science,* 211**,** 55-76.

GRAZIANI, R., BLAIR, M. F., TAYLOR, J. & MAYLE, R. 1980. An experimental study of endwall and airfoil surface heat transfer in a large scale turbine blade cascade.

Journal of Engineering for Power, 102**,** 257-267.

GREGORY-SMITH, D. 1997. Secondary and tip-clearance flows in axial turbines. *VKI LS,* 1.

GREGORY-SMITH, D. & GRAVES, C. 1983. Secondary flows and losses in a turbine cascade. DURHAM UNIV (ENGLAND) DEPT OF ENGINEERING.

GREITZER, E. M., TAN, C. S. & GRAF, M. B. 2007. *Internal flow: concepts and applications*, Cambridge University Press.

GREWE, R. P., MILLER, R. J. & HODSON, H. P. The effect of endwall manufacturing variations on turbine performance. ASME Turbo Expo 2014: Turbine Technical Conference and Exposition, 2014. American Society of Mechanical Engineers, V02CT38A008-V02CT38A008.

HALLER, G. 2005. An objective definition of a vortex. *Journal of fluid mechanics,* 525**,** 1-26.

HAN, J.-C. 2004. Recent studies in turbine blade cooling. *International Journal of Rotating Machinery,* 10**,** 443-457.

HAN, J.-C., DUTTA, S. & EKKAD, S. 2012. *Gas turbine heat transfer and cooling technology*, CRC Press.

HAN, S. & GOLDSTEIN, R. 2006. Influence of blade leading edge geometry on turbine endwall heat (mass) transfer. *Journal of turbomachinery,* 128**,** 798-813.

HARASGAMA, S. & BURTON, C. Film Cooling Research on the Endwall of a Turbine Nozzle Guide Vane in a Short Duration Annular Cascade: Part 2—Analysis and Correlation of Results. ASME 1991 International Gas Turbine and Aeroengine Congress and Exposition, 1991. American Society of Mechanical Engineers, V004T09A012-V004T09A012.

HARASGAMA, S. & BURTON, C. 1992. Film Cooling Research on the Endwall of a Turbine Nozzle Guide Vane in a Short Duration Annular Cascade: Part 1—Experimental Technique and Results. *Journal of turbomachinery,* 114**,** 734-740.

HARRISON, K. L. & BOGARD, D. G. Use of the adiabatic wall temperature in film cooling to predict wall heat flux and temperature. ASME Turbo Expo 2008: Power for Land, Sea, and Air, 2008. American Society of Mechanical Engineers, 1197-1207.

HARTLAND, J., GREGORY-SMITH, D., HARVEY, N. & ROSE, M. Non-Axisymmetric Turbine End Wall Design: Part II—Experimental Validation. ASME 1999 International Gas Turbine and Aeroengine Congress and Exhibition, 1999. American Society of Mechanical Engineers, V001T03A050-V001T03A050.

HARVEY, N. W., ROSE, M. G., TAYLOR, M. D., SHAHPAR, S., HARTLAND, J. &

GREGORY-SMITH, D. G. Non-Axisymmetric Turbine End Wall Design: Part I—Three-Dimensional Linear Design System. ASME 1999 International Gas Turbine and Aeroengine Congress and Exhibition, 1999. American Society of Mechanical Engineers, V001T03A049-V001T03A049.

HAWTHORNE, W. 1955. Rotational flow through cascades Part I. The components of vorticity. *The Quarterly Journal of Mechanics and Applied Mathematics,* 8**,** 266-279.

HERMANSON, K. & THOLE, K. Effect of Non-Uniform Inlet Conditions on Endwall Secondary Flows. ASME Turbo Expo 2002: Power for Land, Sea, and Air, 2002. American Society of Mechanical Engineers, 245-254.

HORLOCK, J. & LAKSHMINARAYANA, B. 1973. Secondary flows: theory, experiment, and application in turbomachinery aerodynamics. *Annual Review of Fluid Mechanics,* 5**,** 247-280.

HORLOCK, J. H. 1958. *Axial flow compressors: fluid mechanics and thermodynamics*, Butterworths scientific publications.

HORLOCK, J. H. 1973. *Axial flow turbines: fluid mechanics and thermodynamics*, Krieger Pub Co.

HUMPHREY, J., WHITELAW, J. & YEE, G. 1981. Turbulent flow in a square duct with strong curvature. *Journal of Fluid Mechanics,* 103**,** 443-463.

HYLTON, L., MIHELC, M., TURNER, E., NEALY, D. & YORK, R. 1983. Analytical and experimental evaluation of the heat transfer distribution over the surfaces of turbine vanes.

INGRAM, G., GREGORY-SMITH, D., ROSE, M., HARVEY, N. & BRENNAN, G. The effect of end-wall profiling on secondary flow and loss development in a turbine cascade. ASME turbo expo 2002: Power for land, sea, and air, 2002. American Society of Mechanical Engineers, 135-145.

JABBARI, M., MARSTON, K., ECKERT, E. & GOLDSTEIN, R. 1996. Film cooling of the gas turbine endwall by discrete-hole injection. *Journal of Turbomachinery,* 118**,** 278-284.

JANSOHN, P. 2013. *Modern gas turbine systems: High efficiency, low emission, fuel flexible power generation*, Elsevier.

JEONG, J. & HUSSAIN, F. 1995. On the identification of a vortex. *Journal of fluid mechanics,* 285**,** 69-94.

JIANG, H., CHEN, W., ZHANG, Q. & HE, L. 2015. Analytical-Solution Based Corner Correction for Transient Thermal Measurement. *Journal of Heat Transfer,* 137**,**

111302.

KAWAI, T. 1994. Effect of combined boundary layer fences on turbine secondary flow and losses. *JSME International Journal Series B Fluids and Thermal Engineering,* 37**,** 377-384.

KNOST, D. & THOLE, K. Adiabatic effectiveness measurements of endwall film-cooling for a first stage vane. ASME Turbo Expo 2004: Power for Land, Sea, and Air, 2004. American Society of Mechanical Engineers, 353-362.

KOPPER, F., MILANOT, R. & VANCOT, M. 1981. Experimental investigation of endwall profiling in a turbine vane cascade. *AIAA Journal,* 19**,** 1033-1040.

KOST, F. & NICKLAS, M. Film-Cooled Turbine Endwall in a Transonic Flow Field: Part I—Aerodynamic Measurements. ASME Turbo Expo 2001: Power for Land, Sea, and Air, 2001. American Society of Mechanical Engineers, V003T01A028-V003T01A028.

KWAK, J. S. & HAN, J.-C. 2003. Heat-transfer coefficients of a turbine blade-tip and near-tip regions. *Journal of thermophysics and heat transfer,* 17**,** 297-303.

LAKSHMINARAYANA, B. 1996. Turbine cooling and heat transfer. *Fluid Dynamics and Heat Transfer of Turbomachinery***,** 597-721.

LANGSTON, L. 1980. Crossflows in a turbine cascade passage. *Journal of engineering for power,* 102**,** 866-874.

LANGSTON, L. 2001. Secondary flows in axial turbines—a review. *Annals of the New York Academy of Sciences,* 934**,** 11-26.

LANGSTON, L., NICE, M. & HOOPER, R. 1977. Three-dimensional flow within a turbine cascade passage. *Journal of Engineering for Power,* 99**,** 21-28.

LAUTERBORN, W. & VOGEL, A. 1984. Modern optical techniques in fluid mechanics. *Annual Review of Fluid Mechanics,* 16**,** 223-244.

LEE, S. W., JUN, S. B., PARK, B.-K. & LEE, J. S. Effects of High Free-Stream Turbulence on the Near-Wall Flow and Heat/Mass Transfer on the Endwall of a Linear Turbine Rotor Cascade. ASME Turbo Expo 2002: Power for Land, Sea, and Air, 2002. American Society of Mechanical Engineers, 231-243.

LEI, D. & LIXIN, C. 2015. Effects of residual riblets of impeller's hub surface on aerodynamic performance of centrifugal compressors. *Engineering Applications of Computational Fluid Mechanics,* 9**,** 99-113.

LETHANDER, A. T., THOLE, K. A., ZESS, G. & WAGNER, J. Optimizing the vane-endwall junction to reduce adiabatic wall temperatures in a turbine vane passage. ASME Turbo Expo 2003, collocated with the 2003 International Joint Power

Generation Conference, 2003. American Society of Mechanical Engineers, 711-721.

LETHANDER, A. T., THOLE, K. A., ZESS, G. & WAGNER, J. 2004. Vane-endwall junction optimization to reduce turbine vane passage adiabatic wall temperatures. *Journal of Propulsion and Power,* 20**,** 1096-1104.

LIANG, G. 2006. Cooling system for an airfoil vane. Google Patents.

LIANG, G. 2009. Turbine vane with leading edge fillet region impingement cooling. Google Patents.

LIN, Y.-L., SHIH, T. I., CHYU, M. & BUNKER, R. Effects of Gap Leakage on Fluid Flow in a Contoured Turbine Nozzle Guide Vane. ASME Turbo Expo 2000: Power for Land, Sea, and Air, 2000. American Society of Mechanical Engineers, V003T01A100-V003T01A100.

LUNDGREN, T. & ASHURST, W. 1989. Area-varying waves on curved vortex tubes with application to vortex breakdown. *Journal of Fluid Mechanics,* 200**,** 283-307.

LYNCH, S. & THOLE, K. 2008. The effect of combustor-turbine interface gap leakage on the endwall heat transfer for a nozzle guide vane. *Journal of Turbomachinery,* 130**,** 041019.

LYNCH, S. P., THOLE, K. A., KOHLI, A., LEHANE, C. & PRAISNER, T. Aerodynamic Loss for a Turbine Blade with Endwall Leakage Features and Contouring. ASME Turbo Expo 2013: Turbine Technical Conference and Exposition, 2013. American Society of Mechanical Engineers, V06AT36A022-V06AT36A022.

MAFFULLI, R. & HE, L. Dependence of external heat transfer coefficient and aerodynamics on wall temperature for 3-D turbine blade passage. ASME Turbo Expo 2014: Turbine Technical Conference and Exposition, 2014. American Society of Mechanical Engineers, V02CT38A046-V02CT38A046.

MAHMOOD, G., GUSTAFSON, R. & ACHARYA, S. 2005. Experimental investigation of flow structure and Nusselt number in a low-speed linear blade passage with and without leading-edge fillets. *Journal of heat transfer,* 127**,** 499-512.

MAN TURBO & DIESEL. 2011. "Industrial gas turbines." product overview http://www.mandieselturbo.com/0001188/Products/Turbomachinery/Industrial-Gas-Turbines.html.

MARINI, R. & GIRGIS, S. The effect of blade leading edge platform shape on upstream disk cavity to mainstream flow interaction of a high-pressure turbine stage. ASME Turbo Expo 2007: Power for Land, Sea, and Air, 2007. American Society of Mechanical Engineers, 587-596.

MCLEAN, C., CAMCI, C. & GLEZER, B. Mainstream Aerodynamic Effects Due to

158

Wheelspace Coolant Injection in a High-Pressure Turbine Stage: Part I—
Aerodynamic Measurements in the Stationary Frame. ASME Turbo Expo 2001:
Power for Land, Sea, and Air, 2001a. American Society of Mechanical Engineers,
V003T01A006-V003T01A006.

MCLEAN, C., CAMCI, C. & GLEZER, B. 2001b. Mainstream Aerodynamic Effects Due
to Wheelspace Coolant Injection in a High-Pressure Turbine Stage: Part II—
Aerodynamic Measurements in the Rotational Frame. *Journal of Turbomachinery,*
123**,** 697-703.

MENTER, F. R. 1994. Two-equation eddy-viscosity turbulence models for engineering
applications. *AIAA journal,* 32**,** 1598-1605.

MIAO, X., ZHANG, Q., ATKIN, C. & SUN, Z. End-Wall Secondary Flow Control Using
Engineered Residual Surface Structure. ASME Turbo Expo 2016:
Turbomachinery Technical Conference and Exposition, 2016. American Society of
Mechanical Engineers, V02BT38A040-V02BT38A040.

MOFFAT, R. J. 1988. Describing the uncertainties in experimental results. *Experimental
thermal and fluid science,* 1**,** 3-17.

MOFFAT, R. J. hadiabatic and u'max. ASME 2003 International Mechanical Engineering
Congress and Exposition, 2003. American Society of Mechanical Engineers, 565-
575.

MORRIS, A. & HOARE, R. Secondary loss measurements in a cascade of turbine blades
with meridional wall profiling. American Society of Mechanical Engineers,
Winter Annual Meeting, Houston, Tex, 1975. 1975.

MOUSTAPHA, S. & WILLIAMSON, R. 1986. Effect of two endwall contours on the
performance of an annular nozzle cascade. *AIAA journal,* 24**,** 1524-1530.

NAVROTSKY, V., GRAICHEN, A. & BRODIN, H. 2015. Industrialisation of 3D printing
(additive manufacturing) for gas turbine components repair and manufacturing.
VGB PowerTech, 12**,** 48-52.

NICKLAS, M. 2001. Film-cooled turbine endwall in a transonic flow field: Part ii—heat
transfer and film-cooling effectiveness. *Journal of Turbomachinery,* 123**,** 720-729.

NOURI, B., LEHMANN, K. & KÜHHORN, A. Investigations on nusselt number
enhancement in ribbed rectangular turbine blade cooling channels of different
aspect ratios and rotation numbers. ASME Turbo Expo 2013: Turbine Technical
Conference and Exposition, 2013. American Society of Mechanical Engineers,
V03AT12A023-V03AT12A023.

O'DOWD, D., ZHANG, Q., HE, L., CHEONG, B. & TIBBOTT, I. 2013. Aerothermal

Performance of a Cooled Winglet at Engine Representative Mach and Reynolds Numbers. *JOURNAL OF TURBOMACHINERY-TRANSACTIONS OF THE ASME,* 135**,** 011041-011041.

O'DOWD, D., ZHANG, Q., HE, L., LIGRANI, P. & FRIEDRICHS, S. 2011. Comparison of heat transfer measurement techniques on a transonic turbine blade tip. *Journal of Turbomachinery,* 133**,** 021028.

O'DOWD, D., ZHANG, Q., LIGRANI, P., HE, L. & FRIEDRICHS, S. Comparison of Heat Transfer Measurement Techniques on a Transonic Turbine Blade Tip. ASME Turbo Expo 2009: Power for Land, Sea, and Air, 2009. American Society of Mechanical Engineers, 323-335.

OHMI, K. & LI, H.-Y. 2000. Particle-tracking velocimetry with new algorithms. *Measurement Science and Technology,* 11**,** 603.

OKE, R., SIMON, T., SHIH, T., ZHU, B., LIN, Y. L. & CHYU, M. Measurements over a film-cooled, contoured endwall with various coolant injection rates. ASME Turbo Expo 2001: Power for Land, Sea, and Air, 2001. American Society of Mechanical Engineers, V003T01A025-V003T01A025.

OKE, R. A. & SIMON, T. W. Film cooling experiments with flow introduced upstream of a first stage nozzle guide vane through slots of various geometries. ASME Turbo Expo 2002: Power for Land, Sea, and Air, 2002. American Society of Mechanical Engineers, 33-40.

OLDFIELD, M. 2008. Impulse response processing of transient heat transfer gauge signals. *Journal of Turbomachinery,* 130**,** 021023.

OLDFIELD, M., JONES, T. & SCHULTZ, D. 1978. On-line computer for transient turbine cascade instrumentation. *IEEE Transactions on Aerospace and Electronic Systems***,** 738-749.

OWEN, J. M. & WILSON, M. 2001. Some Current Research in Rotating-Disc Systems. *Annals of the New York Academy of Sciences,* 934**,** 206-221.

PANIAGUA, G., DENOS, R. & ALMEIDA, S. Effect of the hub endwall cavity flow on the flow-field of a transonic high-pressure turbine. ASME Turbo Expo 2004: Power for Land, Sea, and Air, 2004. American Society of Mechanical Engineers, 1153-1163.

PAUL, A. R., RANJAN, P., UPADHYAY, R. R. & JAIN, A. Flow control in twin air-intakes using vortex generators. Proceedings of the 2011 international conference on Applied & computational mathematics, 2011. World Scientific and Engineering Academy and Society (WSEAS), 107-116.

160

PIGGUSH, J. & SIMON, T. 2013. Flow Measurements in a First Stage Nozzle Cascade Having Endwall Contouring, Leakage, and Assembly Features. *Journal of Turbomachinery,* 135**,** 011002.

POPOVIC, I. & HODSON, H. Aerothermal impact of the interaction between hub leakage and mainstream flows in highly-loaded hp turbine blades. ASME Turbo Expo 2010: Power for Land, Sea, and Air, 2010. American Society of Mechanical Engineers, 965-976.

POPOVIĆ, I. & HODSON, H. P. 2013a. Aerothermal impact of the interaction between hub leakage and mainstream flows in highly-loaded high pressure turbine blades. *Journal of Turbomachinery,* 135**,** 061014.

POPOVÍC, I. & HODSON, H. P. 2013b. Improving turbine stage efficiency and sealing effectiveness through modifications of the rim seal geometry. *Journal of Turbomachinery,* 135**,** 061016.

POPOVIĆ, I. & HODSON, H. P. 2013c. The effects of a parametric variation of the rim seal geometry on the interaction between hub leakage and mainstream flows in high pressure turbines. *Journal of Engineering for Gas Turbines and Power,* 135**,** 112501.

PRAISNER, T., ALLEN-BRADLEY, E., GROVER, E., KNEZEVICI, D. & SJOLANDER, S. 2013. Application of nonaxisymmetric endwall contouring to conventional and high-lift turbine airfoils. *Journal of turbomachinery,* 135**,** 061006.

PRASAD, A. K. 2000. Particle image velocimetry. *CURRENT SCIENCE-BANGALORE-,* 79**,** 51-60.

PRESTON, J. 1954. A simple approach to the theory of secondary flows. *The Aeronautical Quarterly,* 5**,** 218-234.

PRÜMPER, H. 1972. Application of boundary layer fences in turbomachinery(Application of boundary layer fences in turbomachinery). *1972.***,** 311-331.

PRÜMPER, H. 1975. Verbesserung des Wirkungsgrades axialer Turbinenstufen durch Reduzierung der Sekundärverluste.

RAFFEL, M., WILLERT, C. E., SCARANO, F., KÄHLER, C. J., WERELEY, S. T. & KOMPENHANS, J. 2018. *Particle image velocimetry: a practical guide*, Springer.

RANSON, W., THOLE, K. & CUNHA, F. 2005. Adiabatic effectiveness measurements and predictions of leakage flows along a blade endwall. *Journal of turbomachinery,* 127**,** 609-618.

REID, K., DENTON, J., PULLAN, G., CURTIS, E. & LONGLEY, J. The effect of stator-rotor hub sealing flow on the mainstream aerodynamics of a turbine. ASME turbo expo 2006: power for land, sea, and air, 2006. American Society of Mechanical

Engineers, 789-798.

ROLLS ROYCE, P. 2015. *The jet engine*, John Wiley & Sons.

ROSE, M. G. Non-axisymmetric endwall profiling in the HP NGV's of an axial flow gas turbine. ASME 1994 international gas turbine and aeroengine congress and exposition, 1994. American Society of Mechanical Engineers, V001T01A090-V001T01A090.

ROY, R., SQUIRES, K., GERENDAS, M., SONG, S., HOWE, W. & ANSARI, A. Flow and Heat Transfer at the Hub Endwall of Inlet Vane Passages—Experiments and Simulations. ASME Turbo Expo 2000: Power for Land, Sea, and Air, 2000. American Society of Mechanical Engineers, V003T01A006-V003T01A006.

SAHA, A. K. & ACHARYA, S. 2008. Computations of turbulent flow and heat transfer through a three-dimensional nonaxisymmetric blade passage. *Journal of Turbomachinery,* 130**,** 031008.

SARAVANAMUTTOO, H. I. H., ROGERS, G. F. C. & COHEN, H. 2001. *Gas turbine theory*, Pearson Education.

SAUER, H., MULLER, R. & VOGELER, K. 2001. Reduction of secondary flow losses in turbine cascades by leading edge modifications at the endwall. *Journal of turbomachinery,* 123**,** 207-213.

SCARANO, F. 2000. *Particle Image Velocimetry Development and Application: Investigation of Coherent Structures in Turbulent Shear Flows*, Von Karman Institute for Fluid Dynamics.

SCHOBEIRI, M. & LU, K. 2014. Endwall contouring using continuous diffusion: A new method and its application to a three-stage high pressure turbine. *Journal of Turbomachinery,* 136**,** 011006.

SCHULER, P., KURZ, W., DULLENKOPF, K. & BAUER, H.-J. The influence of different rim seal geometries on hot-gas ingestion and total pressure loss in a low-pressure turbine. ASME turbo expo 2010: power for land, sea, and air, 2010. American Society of Mechanical Engineers, 1123-1134.

SCHULZ, A. 2000. Infrared thermography as applied to film cooling of gas turbine components. *Measurement Science and Technology,* 11**,** 948.

SEN, B., SCHMIDT, D. L. & BOGARD, D. G. 1996. Film cooling with compound angle holes: heat transfer. *Journal of Turbomachinery,* 118**,** 800-806.

SHAHPAR, S., LAPWORTH, B., DE PABLOS, T. & TAYLOR, M. A linear approach to the multi-parameter design of three-dimensional turbomachinery blades. 37th Aerospace Sciences Meeting and Exhibit, 1999. 363.

SHARMA, O. & BUTLER, T. Predictions of endwall losses and secondary flows in axial flow turbine cascades. ASME 1986 International Gas Turbine Conference and Exhibit, 1986. American Society of Mechanical Engineers, V001T01A098-V001T01A098.

SIEMENS. 2011. "Industrial gas turbines – the comprehensive product range from 5 to 50 megawatts." product brochure http://www.energy.siemens.com/hq/en/power-gener-ation/gas-turbines/#content=Output%20Overview%20.

SIEVERDING, C. 1985. Recent progress in the understanding of basic aspects of secondary flows in turbine blade passages. *Journal of Engineering for Gas Turbines and Power,* 107**,** 248-257.

SIEVERDING, C. & VAN DEN BOSCHE, P. 1983. The use of coloured smoke to visualize secondary flows in a turbine-blade cascade. *Journal of Fluid Mechanics,* 134**,** 85-89.

SIEVERDING, C. & WILPUTTE, P. 1981. Influence of Mach Number and End Wall Cooling on Secondary Flows in a Straight Nozzle Cascade. *Journal of Engineering for Power,* 103**,** 257-263.

SIMON, T. & PIGGUSH, J. 2006. Turbine endwall aerodynamics and heat transfer. *Journal of propulsion and power,* 22**,** 301-312.

SNEDDEN, G., DUNN, D., INGRAM, G. & GREGORY-SMITH, D. The application of non-axisymmetric endwall contouring in a single stage, rotating turbine. ASME Turbo Expo 2009: Power for Land, Sea, and Air, 2009. American Society of Mechanical Engineers, 831-840.

SNEDDEN, G., DUNN, D., INGRAM, G. & GREGORY-SMITH, D. The performance of a generic non-axisymmetric end wall in a single stage, rotating turbine at on and off-design conditions. ASME Turbo Expo 2010: Power for Land, Sea, and Air, 2010. American Society of Mechanical Engineers, 1069-1080.

SOLAR TURBINES. 2011. "Turbomachinery systems for oil and gas applications." bro-chure http://mysolar.cat.com/cda/layout?m=35420&x=7.

SPRENGER, H. 1969. Druckverluste in 90°-Krümmern für Rechteckrohre. *Schweiz. Bauztg,* 87**,** 223-231.

SQUIRE, H. 1951. The secondary flow in a cascade of airfoils in a nonuniform stream. *Journal of the Aeronautical Sciences,* 18**,** 271-277.

SULLEREY, R. & PRADEEP, A. 2004. Secondary flow control using vortex generator jets. *Journal of fluids engineering,* 126**,** 650-657.

SURYANARAYANAN, A., MHETRAS, S., SCHOBEIRI, M. & HAN, J. 2009. Film-

cooling effectiveness on a rotating blade platform. *Journal of Turbomachinery,* 131**,** 011014.

SURYANARAYANAN, A., OZTURK, B., SCHOBEIRI, M. & HAN, J. 2010. Film-cooling effectiveness on a rotating turbine platform using pressure sensitive paint technique. *Journal of Turbomachinery,* 132**,** 041001.

TAKEISHI, K., MATSUURA, M., AOKI, S. & SATO, T. An experimental study of heat transfer and film cooling on low aspect ratio turbine nozzles. ASME 1989 International Gas Turbine and Aeroengine Congress and Exposition, 1989. American Society of Mechanical Engineers, V004T08A021-V004T08A021.

THOLE, K., RADOMSKY, R., KANG, M. & KOHLI, A. 2002. Elevated freestream turbulence effects on heat transfer for a gas turbine vane. *International journal of heat and fluid flow,* 23**,** 137-147.

THOLE, K. A. & KNOST, D. G. 2005. Heat transfer and film-cooling for the endwall of a first stage turbine vane. *International Journal of Heat and Mass Transfer,* 48**,** 5255-5269.

THOMSON, J. 1877. V. On the origin of windings of rivers in alluvial plains, with remarks on the flow of water round bends in pipes. *Proceedings of the Royal Society of London,* 25**,** 5-8.

THRIFT, A., THOLE, K. & HADA, S. 2011. Effects of an axisymmetric contoured endwall on a nozzle guide vane: convective heat transfer measurements. *Journal of Turbomachinery,* 133**,** 041008.

TRUAX, B. E., DEMAREST, F. C. & SOMMARGREN, G. E. 1984. Laser Doppler velocimeter for velocity and length measurements of moving surfaces. *Applied Optics,* 23**,** 67-73.

VAKIL, S. S. & THOLE, K. Flow and Thermal Field Measurements in a Combustor Simulator Relevant to a Gas Turbine Aero-Engine. ASME Turbo Expo 2003, collocated with the 2003 International Joint Power Generation Conference, 2003. American Society of Mechanical Engineers, 215-224.

WANG, H.-P., OLSON, S. J., GOLDSTEIN, R. J. & ECKERT, E. R. Flow visualization in a linear turbine cascade of high performance turbine blades. ASME 1995 International Gas Turbine and Aeroengine Congress and Exposition, 1995. American Society of Mechanical Engineers, V004T09A007-V004T09A007.

WANG, Z., ZHANG, Q., YAN, Y. & LIU, K. Secondary Flow and Extra Heat Transfer Enhancement of Ribbed Surface After Jet Impingement. ASME Turbo Expo 2016: Turbomachinery Technical Conference and Exposition, 2016. American Society of

Mechanical Engineers, V05AT13A022-V05AT13A022.

WARNER, R. & TRAN, M. 'Recent Developments to Improve High-Pressure and Intermediate-Pressure Turbine Efficiency. I. Mech. E. Turbo Conference, 1987. C275.

WILSON, M., ARNOLD, P., LEWIS, T., MIRZAEE, I., REES, D. & OWEN, J. 1997. Instability of flow and heat transfer in a rotating cavity with a stationary outer casing. *Eurotherm 55 (Heat Transfer in a Single Phase Flow)*.

WRIGHT, L. M., BLAKE, S. & HAN, J.-C. 2007. Effectiveness Distributions on Turbine Blade Cascade Platforms Through Simulated Stator-Rotor Seals. *Journal of thermophysics and heat transfer,* 21**,** 754-762.

WRIGHT, L. M., BLAKE, S. A. & HAN, J.-C. 2008a. Film cooling effectiveness distributions on a turbine blade cascade platform with stator-rotor purge and discrete film hole flows. *Journal of Turbomachinery,* 130**,** 031015.

WRIGHT, L. M., GAO, Z., YANG, H. & HAN, J.-C. 2008b. Film cooling effectiveness distribution on a gas turbine blade platform with inclined slot leakage and discrete film hole flows. *Journal of Heat Transfer,* 130**,** 071702.

WRIGHT, L. M., MALAK, M. F., CRITES, D. C., MORRIS, M. C., YELAVKAR, V. & BILWANI, R. Review of Platform Cooling Technology for High Pressure Turbine Blades. ASME Turbo Expo 2014: Turbine Technical Conference and Exposition, 2014. American Society of Mechanical Engineers, V05BT13A046-V05BT13A046.

YAN, J., GREGORY-SMITH, D. & WALKER, P. Secondary flow reduction in a nozzle guide vane cascade by non-axisymmetric end-wall profiling. ASME 1999 International Gas Turbine and Aeroengine Congress and Exhibition, 1999. American Society of Mechanical Engineers, V001T03A051-V001T03A051.

YAN, X. & GU, P. 1996. A review of rapid prototyping technologies and systems. *Computer-Aided Design,* 28**,** 307-318.

YORK, R., HYLTON, L. & MIHELC, M. 1984. An experimental investigation of endwall heat transfer and aerodynamics in a linear vane cascade. *Journal of Engineering for Gas Turbines and Power,* 106**,** 159-167.

ZESS, G. & THOLE, K. Computational design and experimental evaluation of using a leading edge fillet on a gas turbine vane. ASME Turbo Expo 2001: Power for Land, Sea, and Air, 2001. American Society of Mechanical Engineers, V003T01A083-V003T01A083.

ZHANG, L. & MOON, H. K. Turbine nozzle endwall inlet film cooling: The effect of a back-facing step. ASME Turbo Expo 2003, collocated with the 2003 International

Joint Power Generation Conference, 2003. American Society of Mechanical Engineers, 203-211.

ZHANG, L. J. & JAISWAL, R. S. Turbine Nozzle Endwall Film Cooling Study Using Pressure Sensitive Paint.   ASME Turbo Expo 2001: Power for Land, Sea, and Air, 2001. American Society of Mechanical Engineers, V003T01A030-V003T01A030.

ZHANG, Q., HE, L., WHEELER, A., LIGRANI, P. & CHEONG, B. 2011. Overtip shock wave structure and its impact on turbine blade tip heat transfer. *Journal of Turbomachinery,* 133**,** 041001.

ZHANG, Q., O'DOWD, D., HE, L., OLDFIELD, M. & LIGRANI, P. Transonic Turbine Blade Tip Aero-Thermal Performance With Different Tip Gaps: Part I—Tip Heat Transfer.   ASME Turbo Expo 2010: Power for Land, Sea, and Air, 2010. American Society of Mechanical Engineers, 335-346.

ZHONG, J., HAN, J.-A., LIU, Y. & TIAN, F. Numerical simulation of endwall fence on the secondary flow in compressor cascade.   ASME Turbo Expo 2008: Power for Land, Sea, and Air, 2008. American Society of Mechanical Engineers, 509-518.

ZLATINOV, M. B., TAN, C. S., MONTGOMERY, M., ISLAM, T. & HARRIS, M. 2012. Turbine hub and shroud sealing flow loss mechanisms. *Journal of Turbomachinery,* 134**,** 061027.

Publications

Peer Reviewed Journals:

1. **Miao, X.**, Q. Zhang, Y S Li, C. Atkin, and Z. Sun "IMPROVING PURGE AIR COOLING EFFECTIVENESS BY ENGINEERED END-WALL SURFACE STRUCTURES – PART I: DUCT FLOW"

2. **Miao, X.**, Q. Zhang, Y S Li, C. Atkin, and Z. Sun "IMPROVING PURGE AIR COOLING EFFECTIVENESS BY ENGINEERED END-WALL SURFACE STRUCTURES – PART II: TURBINE CASCADE"

Conference Proceedings:

1. **Miao, X.**, Q. Zhang, C. Atkin, and Z. Sun. "End-Wall Secondary Flow Control Using Engineered Residual Surface Structure." In ASME Turbo Expo 2016: Turbomachinery Technical Conference and Exposition, pp. V02BT38A040-V02BT38A040. American Society of Mechanical Engineers, 2016.